

# Structure and properties of intermetallic ternary rare earth compounds

Dissertation  
zur Erlangung des Grades  
"Doktor der Naturwissenschaften"  
am Fachbereich Chemie, Pharmazie und Geowissenschaften  
der Johannes Gutenberg-Universität Mainz

vorgelegt von  
Frederick Casper  
geboren in Wiesbaden

Mainz, 2008



# Contents

<b>1</b>	<b>Introduction</b>	<b>5</b>
1.1	<i>REME</i> compounds . . . . .	5
1.1.1	Structure . . . . .	6
1.1.2	Magnetism . . . . .	8
1.2	Spintronics . . . . .	11
1.2.1	Magnetoresistance . . . . .	12
1.2.2	Half – metallic ferromagnets . . . . .	16
1.3	This thesis . . . . .	18
<b>2</b>	<b>List of Publications</b>	<b>19</b>
<b>3</b>	<b>Calculation Details</b>	<b>21</b>
3.1	Antiferromagnetic ordering structure of half – Heusler compounds . . . . .	22
3.2	Antiferromagnetic ordering structure of LiGaGe compounds . . . . .	23
<b>4</b>	<b>Experimental Details</b>	<b>25</b>
<b>5</b>	<b>Searching for the Hexagonal Analogues of Half–Metallic Half Heusler <math>XYZ</math></b>	<b>27</b>
5.1	Crystal structures of the hexagonal compounds $RECuSn$ . . . . .	28
5.2	Electronic structures of the hexagonal compounds $RECuSn$ . . . . .	30
5.3	The influence of puckering on the band structure and the electron localization function . . . . .	32
5.4	Conclusion . . . . .	35
<b>6</b>	<b>GdAuE Compounds</b>	<b>37</b>
6.1	Introduction . . . . .	37
6.2	Crystal structures and details of the calculations . . . . .	37
6.3	Results and Discussion . . . . .	40
6.3.1	Density of states . . . . .	40
6.3.2	Chemical Bonding . . . . .	43
6.4	Conclusion . . . . .	45
<b>7</b>	<b>GdNiSb Compounds</b>	<b>47</b>
7.1	Introduction . . . . .	47
7.2	Band structure calculation . . . . .	48
7.3	Mössbauer measurements . . . . .	49

7.4	Summary . . . . .	51
<b>8</b>	<b>GdPdSb Compound</b>	<b>53</b>
8.1	Introduction . . . . .	53
8.2	Structural characterization . . . . .	54
8.3	Band structure calculations . . . . .	55
	8.3.1 Antiferromagnetic GdPdSb . . . . .	55
	8.3.2 Ferromagnetic GdPdSb . . . . .	57
8.4	Magnetic properties . . . . .	59
8.5	Conductivity measurements . . . . .	60
8.6	Mössbauer measurements . . . . .	62
8.7	Summary and conclusion . . . . .	63
<b>9</b>	<b>REAuSn Compounds</b>	<b>65</b>
9.1	Introduction . . . . .	65
9.2	Structural characterization . . . . .	65
9.3	Band structure and density of states . . . . .	68
9.4	Magnetic measurements . . . . .	70
	9.4.1 REAuSn ( $RE = \text{Gd, Er, Tm}$ ) . . . . .	70
	9.4.2 MnAuSn . . . . .	70
9.5	Mössbauer measurements and magnetism of GdAuSn . . . . .	71
9.6	Resistivity and magnetoresistance measurements . . . . .	74
9.7	Photoemission of ErAuSn . . . . .	77
9.8	Granular system . . . . .	78
9.9	Summary and conclusion . . . . .	80
<b>10</b>	<b>RENiBi Compounds</b>	<b>83</b>
10.1	Introduction . . . . .	83
10.2	Structural characterization . . . . .	83
10.3	Magnetic measurements . . . . .	85
10.4	Conductivity measurements . . . . .	89
10.5	Band structure calculations . . . . .	91
10.6	Magnetoresistance . . . . .	92
10.7	Inhomogeneous DyNiBi compound . . . . .	95
10.8	LuNiBi . . . . .	96
10.9	Summary . . . . .	97
<b>11</b>	<b>Summary and Outlook</b>	<b>99</b>
11.1	Summary . . . . .	99
11.2	Outlook . . . . .	101

# 1 Introduction

## 1.1 *REME* compounds

In the modern science world multidisciplinary research is an always growing field. The combination of chemical and physical methods, so called material science, is a new task for solid state chemists. To fulfill the needs for a variety of demands, new materials must be developed. Thus not only structural determination, but also magnetic and electronic properties of new materials should be investigated. This comes along with theoretical calculations and predictions for these compounds.

A class of compounds that has attracted a great deal of attention in recent years is known as *REME* compounds. These compounds are often referred to with *RE* designating rare earth, actinide or an element from group 1 – 4, *M* representing a late transition metal from groups 8 – 12, and *E* belonging to groups 13 - 15. There are more than 2000 compounds with 1:1:1 stoichiometry belonging to this class of compounds [1] and they offer a broad variety of different structure types [2, 3]. Here the focus was only on compounds containing elements as shown in Figure 1.1.

**REME  
Compounds**

H																			He
Li	Be											B	C	N	O	F	Ne		
Na	Mg											Al	Si	P	S	Cl	Ar		
K	Ca	Sc	Ti	V	Cr	Mn	Fe	Co	Ni	Cu	Zn	Ga	Ge	As	Se	Br	Kr		
Rb	Sr	Y	Zr	Nb	Mo	Tc	Ru	Rh	Pd	Ag	Cd	In	Sn	Sb	Te	I	Xe		
Cs	Ba		Hf	Ta	W	Re	Os	Ir	Pt	Au	Hg	Tl	Pb	Bi	Po	At	Rn		
Fr	Ra																		
		La	Ce	Pr	Nd	Pm	Sm	Eu	Gd	Tb	Dy	Ho	Er	Tm	Yb	Lu			
		Ac	Th	Pa	U	Np	Pu	Am	Cm	Bk	Cf	Es	Fm	Md	No	Lr			

Figure 1.1: Periodic table of elements, *REME* elements are marked blue, red and green, respectively

*REME* compounds can have interesting electronic and magnetic properties such as heavy fermion systems [4, 5], heavy electron behavior, half metallic behavior in some Ce compounds [6, 7], mixed valent behavior in Eu, Yb and Ce compounds [8, 9, 10, 11, 12, 13], giant magnetoresistance in heavy rare earth compounds [14] and superconductivity [13, 15]. These compounds usually order magnetically at low temperatures with a variety of magnetic moments that are confined to the rare earth sublattice. In particular, materials which display large changes in resistivity in response to an applied

magnetic field (magnetoresistance) are currently of great interest, due to their potential for applications in magnetic sensors, magnetic random access memories (MRAM), and spintronics – a new kind of electronics based on spin instead of charge [16].

An experimental and theoretical investigation of the magnetic and electronic properties of some *REME* compounds is presented in this thesis. Some of these compounds show a granular magnetoresistance effect, Giant Magnetoresistance effect (GMR) and/or an Extraordinary Magnetoresistance effect (EMR) depending on the charge carrier density, structure, order-disorder on the atomic scale, phase separation, spinorbit coupling, and magnetism.

### 1.1.1 Structure

As mentioned above, the *REME* phases offer a large variety of structure types. Table 1.1 gives an overview about the structural variety of the *REME* compounds according to the number of valence electrons. The *f*-electrons of the rare earth metal are localized and therefore not considered as valence electrons. The main focus in this thesis is on compounds with 18 valence electrons. Only among these *REME* compounds such with LiGaGe and MgAgAs (“half – Heusler” structure) structure can be found. A nearly complete overview of all *REME* compounds concerning structural variety and stacking is given Bojin *et al.* [17, 18]. For europium and sometimes for ytterbium, the oxidation state is only +2. For example EuNiSb has only 17 valence electrons and crystallizes in the orthorhombic Imm2 structure, while EuNiSb (18 valence electrons) has the hexagonal ZrBeSi structure.

Table 1.1: Overview of the *REME* compounds structure variety according to the number of valence electrons (VE).

VE	structure	space group	examples
8	Fe <sub>2</sub> P	P $\bar{6}2m$	HoLiGe, LaMgTl
	LiYSn	P6 <sub>3</sub> mc	YLiSn, TmLiSn
	<b>MgAgAs</b>	F $\bar{4}3m$	NdLiSn, CeLiSn
9	none		
10	none		
11	PbClF	P4/nmm	DyTiGe, DyTiSi
	AlB <sub>2</sub>	P6/mmm	DyZnSi, GdZnGe
	La <sub>2</sub> Sb	I4/mmm	GdTiGe
12	La <sub>2</sub> Sb	I4/mmm	DyZrSb
13	Cu <sub>2</sub> Mg	Fd $\bar{3}m$	TbMnAl
	Fe <sub>2</sub> P	P $\bar{6}2m$	HoMnGa, TbMnGa
	FeSiTi	Ima2	YMnGa
14	Cu <sub>2</sub> Mg	Fd $\bar{3}m$	YFeAl
	Fe <sub>2</sub> P	P $\bar{6}2m$	ScRuGe
	MgZn <sub>2</sub>	P6 <sub>3</sub> /mmc	GdFeAl
	PbClF	P4/nmm	CeMnGe, LaCoGe
	TiNiSi	Pnma	DyMnGe
15	Fe <sub>2</sub> P	P $\bar{6}2m$	LaRhIn
	MgZn <sub>2</sub>	P6 <sub>3</sub> /mmc	ScCoAl
	PbClF	P4/nmm	ScFeSi
	TiNiSi	Pnma	DyFeSi
16	Fe <sub>2</sub> P	P $\bar{6}2m$	NdAgMg, DyNiAl
	Hg <sub>2</sub> K	Imma	ErNiGa
	PbClF	P4/nmm	NdCoSi, TbCoSi
	TiNiSi	Pnma	HoCoSi, DyIrGe
17	Cu <sub>2</sub> Mg	Fd $\bar{3}m$	LuCuAl, TbCuAl
	MgZn <sub>2</sub>	P6 <sub>3</sub> /mmc	ScCuAl
	CaIn <sub>2</sub>	P6 <sub>3</sub> /mmc	GdCuTl
	YPdSi	Pmnm	PrPtSi
	LaPtSi	I41md	GdPtSi, LaNiSi
	Fe <sub>2</sub> P	P $\bar{6}2m$	DyPdTl, TbDyTl
	Hg <sub>2</sub> K	Imma	ErPdSi
	TiNiSi	Pnma	HoPdGa, HoNiGa
18	ZrBeSi	P6 <sub>3</sub> /mmc	LaPdP, LaCuSi
	<b>LiGaGe</b>	P6 <sub>3</sub> mc	GdAuSn
	CaIn <sub>2</sub>	P6 <sub>3</sub> /mmc	DyAgSn, DyAgPb
	AlB <sub>2</sub>	P6/mmm	NdAgSi, NdAgPb
	BiIn <sub>2</sub>	P6/mmm	GdCuSi
	Fe <sub>2</sub> P	P $\bar{6}2m$	DyAgGe, LuAgSn
	<b>MgAgAs</b>	F $\bar{4}3m$	GdAuPb, GdNiBi
19	BiIn <sub>2</sub>	P6/mmm	CeCuGe
	PtYAs	P6 <sub>3</sub> /mmc	YPtAs
$\geq 20$	none		

### Cubic MgAgAs structure

The MgAgAs structure can be thought as a  $RE^{n+}$  ion within a zincblende  $ME^{n-}$  sublattice [19]. Recently it was shown that these compounds are closed shell species, non magnetic and semiconducting or have a pseudo gap at the Fermi energy [20]. Here the trivalent electro positive  $RE^{3+}$  ion of the  $RE^{3+}ME^{3-}$  compounds occupy the Mg sites. This structure can be described as filled MgAs, NaCl structure type in which  $M$  atoms are inserted in half of the tetrahedral holes (Ag position) in the lattice. In this description, the compound can be viewed as either  $M$  atoms in the host  $RE^{3+}E^{3-}$  lattice or as filled ZnS zincblende type lattice  $ME^{3-}$  in which  $RE^{3+}$  atoms occupy octahedral holes. Not counting equivalent permutations this face-centered cubic structure has possible three different atomic distributions, depending on which atom is at the  $4c$  ( $\frac{1}{4}\frac{1}{4}\frac{1}{4}$ ) position. For every distribution, only the intensities in the x-ray diffraction pattern are different.

The structure can also be thought of as the Heusler structure ( $L2_1$  structure,  $Fm\bar{3}m$ ) where half of the tetrahedral sites are empty (Figure 5.1a). Thus  $REME$  atoms can occupy the vacant site and antiphase domains corresponding to the inversion of two different atoms may occur. Such defects can not be easily detected by X-ray or neutron diffraction, but have significant impact on the resistance of the polycrystalline samples.

A change of the valence electron concentration should strongly affect the properties of  $REME$  compounds with MgAgAs structure [21, 22, 20]. Half Heusler compounds with 22 electrons (e.g. with Mn at the  $RE$  position) should be localized moment ferromagnets. The 22 electrons divide themselves into 13 in the majority spin and 9 in the minority spin direction, resulting in a semiconducting gap (half metallic behavior) in the majority spin direction. Unfortunately, changing the valence electron number lead to either a structural change or a granular system due to phase separation (see Chapter 7).

### Hexagonal LiGaGe structure

The LiGaGe structure is shown in Figure 5.1b. This structure can be seen as ordered  $CaIn_2$  structure. It should be noted that many compounds, earlier identified as having a  $CaIn_2$  structure type, were later identified as having a LiGaGe structure type [23, 24, 25, 26, 27]. In the hexagonal LiGaGe structure, the  $M_3E_3$  hexagons have an ABAB layered structure, whereas the cubic MgAgAs structure can be described as an ABCABC sequence (Figure 9.2).

#### 1.1.2 Magnetism

On the first viewing the magnetic behavior of  $REME$  compounds looks rather unexciting. In particular most of the MgAgAs and LiGAGe compounds are antiferromagnetic and have low Neel temperatures [28]. The magnetic moments of the ternary  $REME$  compounds are almost exclusively due to localized  $4f$  electrons. The value of the effective magnetic moments  $\mu_{eff}$  is in good agreement with the values for the free  $RE^{n+}$  ions,

which can be obtained from (see Figure 1.2)

$$\mu_{eff}(theo) = g_j[J(J+1)]^{1/2}. \quad (1.1)$$

This agreement can be explained by the small disturbance of the 4  $f$ , which are lying deep within the  $RE^{n+}$  ion, when attached to the crystal lattice [29].

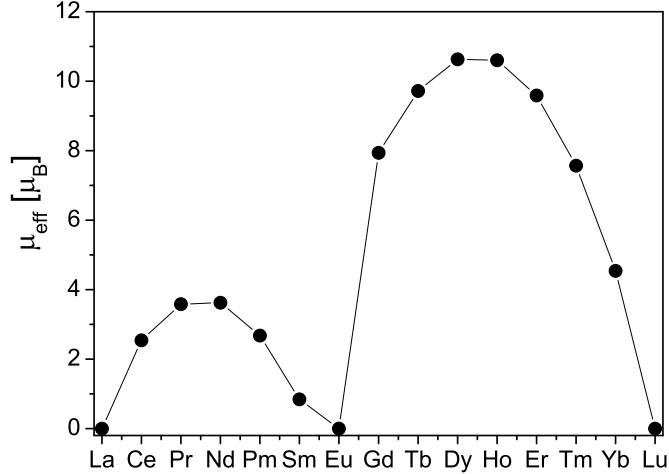


Figure 1.2: Theoretical effective magnetic moments  $\mu_{eff}$  of the free  $RE^{3+}$  ions obtained from equation 1.1

The Hamiltonian describing the magnetic properties of rare-earth ions is usually presented in the form:

$$H_{tot} = H_{Coul} + H_{ex} + H_{cf} + H_{ms} + H_{ext}, \quad (1.2)$$

where  $H_{Coul}$  is the Coulomb interaction,  $H_{ex}$  the exchange interaction,  $H_{cf}$  the crystal field term,  $H_{ms}$  the magnetorestriction effect and  $H_{ext}$  accounts for the interaction with an external magnetic field. The  $H_{ex}$  and the  $H_{cf}$  are the most dominant terms [28].

On the other hand, a closer look reveals a more complex magnetic behavior, which is also related to some remarkable transport properties (see chapter 10). Especially in the *REME* compounds with LiGaGe structure, the energy difference of the ferromagnetic and antiferromagnetic ground state is marginal [30]. Thus a competition between these ground states can not be excluded (see Chapter 8)

### Exchange Interactions

In **metallic** compounds of rare earths, exchange interactions between rare-earth moments are mediated by the spin polarization of conduction electrons. This kind of interaction is related to elements and compounds where the magnetic and electric properties

are defined by different kinds of electrons. The interaction was originally proposed by Ruderman and Kittel [31], later extended by Kasuya [32] and Yoshida [33] and is known as RKKY interaction. One of the most significant applications of the RKKY theory has been to the theory of giant magnetoresistance (see chapter 1.2.1). In the RKKY theory, the critical temperature of the magnetic ordering ( $T_C$  or  $T_N$ ) and the paramagnetic Curie temperature  $\theta_P$  are proportional to the de Gennes factor  $(g_J - 1)^2 J(J + 1)$  (Figure 1.3).

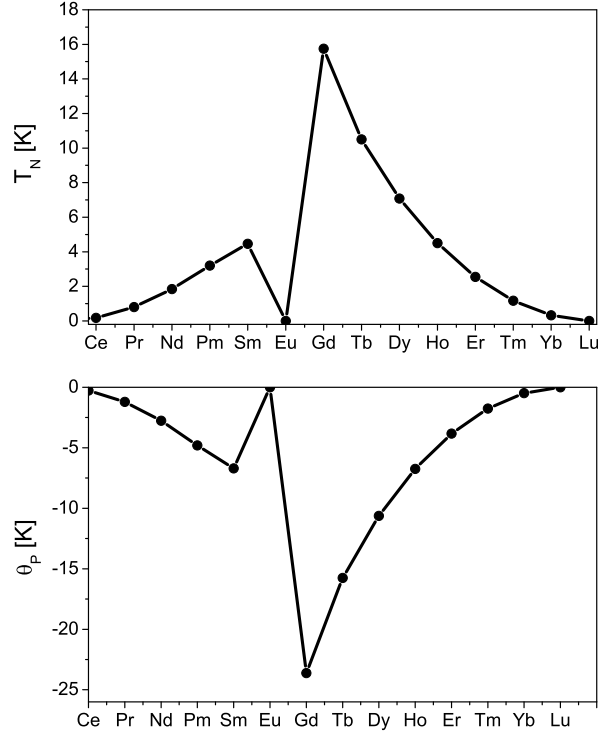


Figure 1.3: Prediction of the de Gennes scaling for the magnetic ordering temperatures  $T_N$  (top) and paramagnetic Curie  $\theta_P$  (bottom) of *REME* compounds as a function of the rare earth atom, whereby  $T_N$  should be maximum in the Gd – containing compounds

In **semiconducting and insulating** rare earth compounds, the magnetism arises from superexchange interaction. Here the atoms which strongly interact magnetically are quite definitely separated from each other by intervening non-magnetic atoms. The energy of the superexchange between two atoms  $i, j$  with the spins  $\mathbf{S}_i, \mathbf{S}_j$  is given in the Heisenberg Model by:

$$U = -2JS_i \cdot S_j, \quad (1.3)$$

The exchange integral  $J$  is negative for antiferromagnetic coupling. For a review, see [34]

Another interaction in rare earth compounds is the Kondo effect [35, 36]. the Kondo effect tends to compensate the local moment on moment-bearing ion and thus leads to the formation of a nonmagnetic ground state. Such behavior is discussed for some ternary rare earth compounds, e.g. CePdSb [37].

### Crystalline electric field

The magnetic properties of rare earth compounds can also be determined by the interaction of the  $4f$  electrons with the electric charges due to the surrounding ions. Each rare-earth ion in a crystal is submitted to an inhomogeneous electrostatic potential originating from the electric charges of the surrounding ions and the conducting electrons in the case of metallic compounds.

A closer look at some of those compounds reveals a more complex magnetic structure, which is connected with unusual transport properties. In europium compounds with approximately 18 valence electrons (such as EuNiP) the structure and properties are in an extremely well correlation [9]. With the change of the electronic structure the elastic properties are changing. Thus with increasing valence the layers are more puckered (see also chapter 5). For compounds with Ce, Eu, Sm and Yb, the  $RE$  valence should affect the bonding length and magnetism.

For some compounds, especially the among hexagonal ones, the energy difference between the antiferromagnetic and ferromagnetic ground states is marginal, a competition between the two ground states can not be excluded [30].

## 1.2 Spintronics

Despite the enormous progress in the field of electronics in the last decades, many applications in the field of data storage are based on the property of electron charge. Today the physical limit, namely the size of the structures, has been reached. A promising approach to overcome this problem is the so called spintronic device. It includes all magnetoelectronic effects that are based on the spin polarization of electrons, holes, and currents or both in semiconducting devices. The major ingredients for its realization are the transfer of spin information into semiconductor device (spin injection), the manipulation and storage of the spin and the detection of the spin information.

Since the discovery of the giant magnetoresistance (GMR) effect in 1988, many groups are working worldwide on further developments and application of magnetoresistance effects. The commercial implementation of a GMR read head by IBM in 1997 started a rapid shrinking of magnetic structures. As this shrinking of magnetic structures causes a reduction in the field strength to prevent interaction of adjacent bits, the demand of high sensitivity is still increasing. The so called half – metallic ferromagnets have an important role in the field of spintronics.

In the following a short introduction of magnetoresistance effects and half – metallic ferromagnets will be given.

### 1.2.1 Magnetoresistance

The change of the resistance in an applied field is called magnetoresistance. The magnetoresistance is defined as:

$$\Delta R = (R_{field} - R_0)/R_0, \quad (1.4)$$

where  $R_{field}$  and  $R_0$  are the resistances with and without applied field. A large change in the electrical resistivity in a weak applied magnetic field is of technological relevance.

#### Anisotropic magnetoresistance (AMR)

The first magnetoresistive effect, the anisotropic magnetoresistance effect (AMR), was discovered by W. Thomson, Lord Kelvin in 1856 [38]. The AMR is the property of a ferromagnetic metal in which a dependence of electrical resistance on the angle between the direction of electrical current and orientation of magnetic field is observed (figure 1.4).

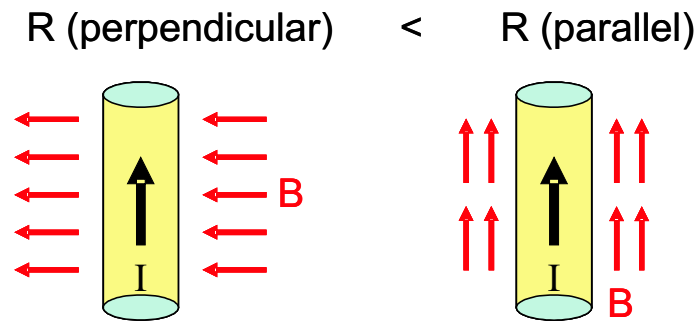


Figure 1.4: Angular dependence (for fields parallel and perpendicular the the sample) of the AMR effect.

Although the effect is very weak ( $\approx 4\%$ ) it is used in read out heads, magnetoresistive random access memory (MRAM) and magnetic sensors.

#### Giant magnetoresistance (GMR)

A breakthrough occurred with the discovery of giant magneto-resistance (GMR) in 1988 by Grünberg [39] and Fert [40]. The Giant magneto-resistive effect is observed in multilayer systems consisting of interleaved magnetic and non-magnetic layers. Figure 1.5 shows an example of such a multilayer Fe–Cr–Fe system. At certain thicknesses the RKKY coupling between adjacent ferromagnetic layers becomes antiferromagnetic, making it energetically preferable for the magnetizations of adjacent layers to align in an antiparallel configuration. The electrical resistance of the system is normally higher in the anti-parallel case. The resistivity drops as the configuration of the magnetisation

in neighboring Fe layers goes from antiparallel to parallel when an external magnetic field is applied. If the exchange coupling is antiferromagnetic, the electrons experience strong scattering at the interface, resulting in a high resistance.

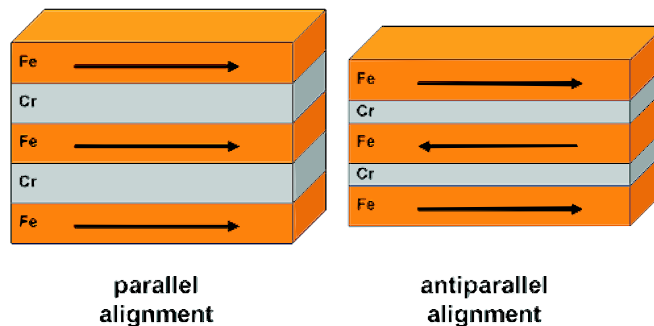


Figure 1.5: A multilayer system Fe–Cr–Fe with ferromagnetic (left) and with antiferromagnetic (right) exchange coupling between the iron layers.

Another possible arrangement, the so called spin valve, consists of two ferromagnetic layers sandwiching a thin non-magnetic metal layer. If the coercive fields of the two ferromagnetic electrodes are different it is possible to switch them independently. Therefore, parallel and anti-parallel alignment can be achieved, and normally the resistance is again higher in the anti-parallel case. Since 1997 the read out heads of magnetic discs are based on the GMR effect [41].

### Colossal magnetoresistance (CMR)

Another magnetoresistance effect was found in mixed valence manganese perovskites. In a certain range of doping ( $x \approx 0.2 - 0.4$ ) the ground state of the compound  $\text{La}_{1-x}\text{Ca}_x\text{MnO}_3$  changes from antiferromagnetic to ferromagnetic. The paramagnetic to ferromagnetic transition is accompanied by a sharp drop in resistivity. This phenomenon has been known to exist since 1950 [42, 43]. In 1993, von Helmolt et al.[44], and soon followed by Jin et al.[45], showed that the transition can be suppressed by magnetic fields and thus leads to a large magnetoresistance effect, the so-called colossal magnetoresistance (CMR). Today the CMR is known in some more compounds, e.g., in  $\text{EuO}$  [46],  $\text{GdI}_2$  [47], in the  $\text{Gd}_{3-x}\text{S}_4$  system [48], and in a few other rare earth compounds. Although the effect is large in some compounds, the MR ratio in small fields as well as the transition temperatures are too low for use in applications.

### Tunnel magnetoresistance (TMR)

The use of half-metallic electrodes in spin valves or in magnetic tunnel junctions (MTJs) results in a pronounced increase in the magneto-resistance. As shown in Figure 1.6, a tunnel junction is a device in which the pinned magnetic layer and the free magnetic layer are separated by a very thin insulating layer. Then the resistance of the tunneling current changes with the relative orientation of the two magnetic layers. The effect was

first discovered by Julliere [49] and called tunnel magnetoresistance (TMR). Following the Julliere model, the tunnelling magnetoresistance (TMR) ratio of a junction is related to the spin polarisation  $P$  (a high spin polarisation is required for high TMR ratios). Today very high TMR ratios of more than 400 %<sup>1</sup> at room temperature were achieved with crystalline MgO barriers [50, 51, 52], but the TMR effect is not as yet used in applications.

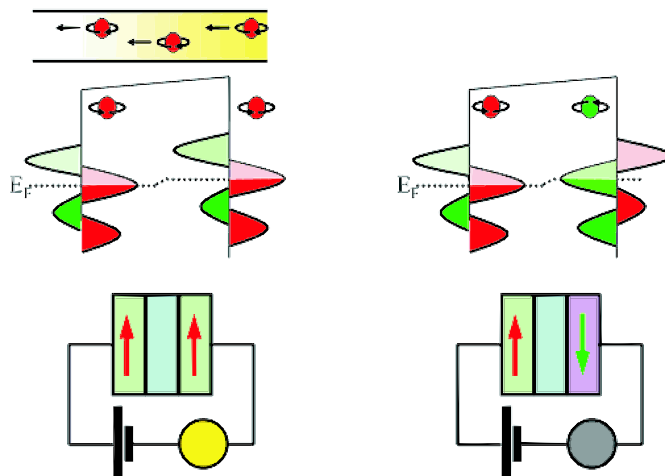


Figure 1.6: A typical tunnel magnetoresistance device (TMR)

### Granular magnetoresistance

Granular magnetoresistance is observed in granular magnetic materials and is related to GMR. The effect occurs in solid precipitates of a magnetic material in a non-magnetic matrix, eg. in matrices of copper containing cobalt granules [53]. The reason for this is that copper and cobalt are nearly immiscible, so it is possible to create the solid precipitate by rapidly cooling a molten mixture of copper and cobalt. Granule sizes vary depending on the cooling rate and amount of subsequent annealing. In these systems, the magneto-resistance curve looks like the MR curve of a multi-layer GMR system. On the other hand, a positive granular magnetoresistance was found for magnetic inclusions in a antiferromagnetic matrix [23]. Figure 1.7 shows a schema of a granular sample and the behavior of the magnetic inclusions in an external field.

<sup>1</sup>Note that the TMR ratio here is calculated by  $\frac{\Delta R}{R} = \frac{R_P - R_{AP}}{R_P}$ ;  $R_P$ /  $R_{AP}$  resistivity for parallel/antiparallel alignment

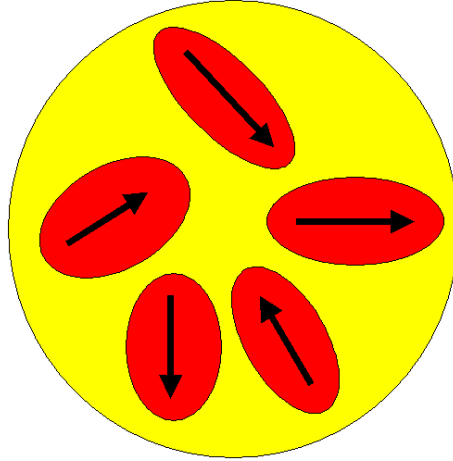


Figure 1.7: Granular magnetoresistance

### Extraordinary magnetoresistance

Recently, the so-called extraordinary magnetoresistance (EMR) was found in semiconductor-metal hybrid structures. The change of the resistance was as high as 100 - 750000 % in fields ranging from 0.05 to 4T for symmetric van der Pauw disk at room temperature [54]. The EMR effect is due to the magnetic field induced current redistribution between the semiconductor and the metal (figure 1.8). In principle, the EMR is defined as:

$$\Delta R_{EMR}(\Delta B) = \frac{R_{field}(\Delta B) - R_0}{R_0} = G(\Delta B)(\mu\Delta B)^2, \quad (1.5)$$

where  $\mu$  is the mobility of the dominant carrier,  $B$  the magnetic field and  $G(\Delta B)$  is a geometric factor that depends on the shape, location and physical properties of the conducting inhomogeneity and contacts. An EMR of 6% at 300 K at a relevant field of 50 mT was found for a microstructured metal-semiconductor hybrid structure [55], thus making the effect usable for applications.

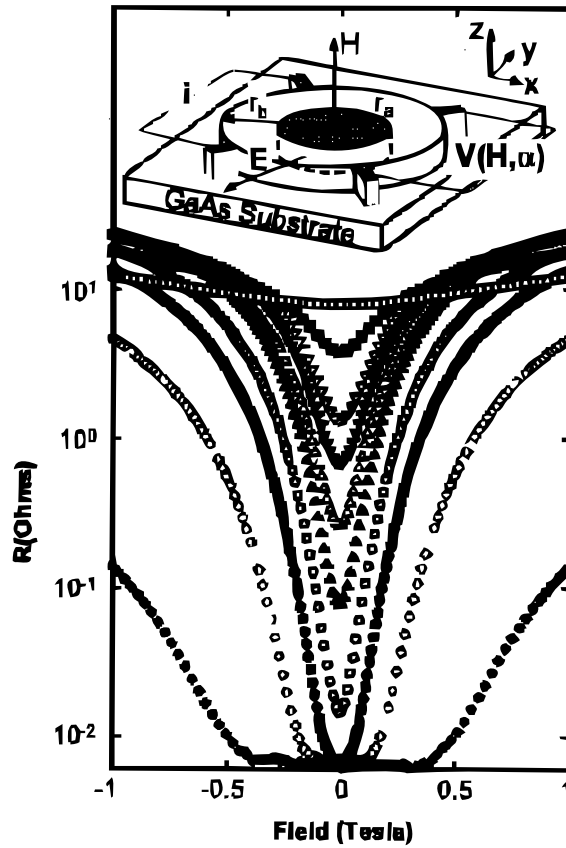


Figure 1.8: Room temperature magneto resistance of a composite van der Pauw disk (top picture) of InSb and Au for a number of values of  $\alpha = r_a/r_b$ . The symbols correspond to an  $\alpha$  between 0 and  $\frac{15}{16}$ , increasing from top to bottom [54].

Due to disorder in atomic to nano scale, also some bulk systems show such a formation of semiconductor - metal hybrid structures. For the first time this was observed in InSb/ NiSb. Here NiSb needles were formed in a semiconducting InSb matrix, and the compound showed a EMR of 20 % [56].

### 1.2.2 Half – metallic ferromagnets

In 1983, de Groot defined a half-metallic ferromagnet as a compound having a gap at the Fermi energy in one spin direction while the opposite density is metallic (Figure 1.9). One of the first materials predicted to be HMF by electronic band structure calculations was the MgAgAs type compound NiMnSb [21]. Recent interest in the idea that solid state devices can function through manipulation of the spin of electrons [57, 58] has given rise to a wealth of research in the area of half-metals, which play an important role in spin injection [59, 60]. Most of the magnetic and half-metallic MgAgAs compounds contain

Mn. Kübler *et al.* [61] attribute this to the manganese ion, which has an approximate  $\text{Mn}^{3+}$  configuration and a highly localized moment of 3 - 4  $\mu_B$ . Rare earth ions in these compounds have also a charge of +3 with the localized moments coming from the  $f$  electrons, and should show the same properties in the case that they are ferromagnetic [20].

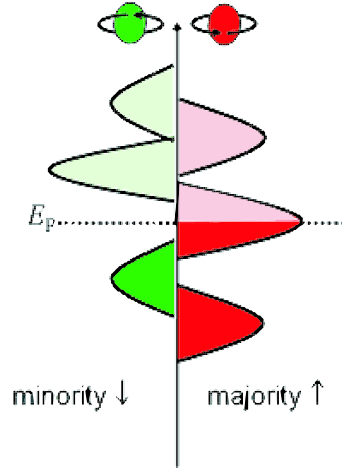


Figure 1.9: Schematic density of states (DOS) of a half-metallic ferromagnet.

Table 1.2 shows a broad classification scheme for half-metallic ferromagnets as proposed by Coey [62]. Type I and II half-metals in this scheme fit the original description made by de Groot. Additionally some more half-metals were defined. Type III and IV half metals are also known as “transport half metals”. They have localised majority states and delocalised minority states, or vice versa [63]. Diluted magnetic semiconductors build up the group of type V half metals.

Table 1.2: The classification of half-metals proposed by Coey *et al.* [62]

Type	Density of states	Conductivity	↑ Electrons at $E_F$	↓ Electrons at $E_F$
IA	half-metal	metallic	itinerant	none
IB	half-metal	metallic	none	itinerant
IIA	half-metal	nonmetallic	localised	none
IIB	half-metal	nonmetallic	none	localised
IIIA	metal	metallic	itinerant	localised
IIIB	metal	metallic	localised	itinerant
IVA	semi-metal	metallic	itinerant	localised
IVB	semi-metal	metallic	localised	itinerant
VA	semiconductor	semiconducting	few, itinerant	none
VB	semiconductor	semiconducting	none	few, itinerant

### 1.3 This thesis

Although many *REME* compounds are known to exist, mainly only structure and magnetism has been determined for these compounds. In particular, in the field of electronic and transport properties relatively few efforts have been made. The main focus in this study is on compounds crystallizing in MgAgAs and LiGaGe structure. Both structures can only be found among 18 valence electron compounds. The *f* electrons are localized and therefore not count as valence electrons. A special focus here was also on the magnetoresistance effects found among the *REME* compounds.

In Chapter 5 a theoretical examination of the band structure of the hexagonal compounds is shown to see if hexagonal analogues of the half-metallic half Heusler exists.

Chapter 6 deals with some *REME* compounds that have less than 18 valence electrons. The electronic structure of the isotypic GdAuX ( $X = \text{Mg}, \text{Cd}$  and  $\text{In}$ ) compounds are presented as well as a study of the composition of the valence band.

The next two chapters deal with the GdNiSb and GdPdSb compounds. GdNiSb crystallizes in two different structure types, which could not be separated. The magnetic properties were investigated on the biphasic compound by the means of Mössbauer spectroscopy. GdPdSb is a hexagonal LiGaGe compound with an interesting magnetic behavior at low temperature. This behavior was examined by SQUID measurements and Mössbauer spectroscopy to see if a ferromagnetic ordering at low temperature takes place. In the case of ferromagnetic ordering, GdPdSb would be a half-metallic ferromagnet according to band structure calculations.

Chapter 9 and 10 show the magnetic and electronic properties of *REAuSn* and *RENiBi* compounds. In both series, interesting magnetoresistance effects (GMR, granular magnetoresistance, possible EMR) were found.

## 2 List of Publications

1. F. Casper, G. Jakob, S. Wurmehl, H. J. Elmers, and C. Felser  
*Dünne epitaktische Filme der Heusler-Phase  $\text{Co}_2\text{Cr}_{0.6}\text{Fe}_{0.4}\text{Al}$*   
Z. Anorg. Allg. Chem. 630 (2004), 1715
2. G. Jakob, F. Casper, V. Beaumont, S. Falk, N. Auth, H.-J. Elmers, C. Felser, and H. Adrian  
*Thin epitaxial films of the Heusler compound  $\text{Co}_2\text{Cr}_{0.6}\text{Fe}_{0.4}\text{Al}$*   
J. Mag. Mag. Mat. 290-291 (2005), 1104
3. S. Wurmehl, G. H. Fecher, V. Ksenofontov, F. Casper, U. Stumm, C. Felser, H.-J. Lin, and Y. Hwu  
*Half-metallic ferromagnetism with high magnetic moment and high Curie temperature in  $\text{Co}_2\text{FeSi}$*   
a) Los Alamos National Laboratory, Preprint Archive, Condensed Matter (2005), 1-3, arXiv:cond-mat/0511463.  
b) J. App. Phys. 99(8) (2006), 08J103/1
4. F. Casper, V. Ksenofontov, H. C. Kandpal, S. Reiman, T. Shishido, M. Takahashi, M. Takeda, and C. Felser  
*Structure and properties of  $\text{GdAuSn}$  and the  $\text{GdAuSn}/\text{MnAuSn}$  system*  
Z. Anorg. Allg. Chem. 632 (2006), 1273
5. V. Ksenofontov, K. Kroth, S. Reiman, F. Casper, V. Jung, M. Takahashi, M. Takeda, and C. Felser  
*Mössbauer spectroscopic study of half-Heusler compounds*  
Hyperfine Interactions 168 (2007), 1201
6. F. Casper, H. C. Kandpal, G. H. Fecher, and C. Felser  
*Electronic and magnetic properties of  $\text{GdPdSb}$*   
J. Phys. D: Appl. Phys. 40 (2007), 3024

7. H. C. Kandpal, F. Casper, G. H. Fecher, C. Felser, J. Kübler, and R. Pöttgen  
*Variation of the bonding interactions and magnetism in GdAuX (X = Mg, Cd, and In)*  
Los Alamos National Laboratory, Preprint Archive, Physics (2007), 1-15, arXiv:0709.4445v1
  
8. F. Casper, C. Felser, R. Seshadri, C. P. Sebastian, and R. Pöttgen  
*Searching for hexagonal analogues of the half-metallic half-Heusler XYZ compounds*  
a) Los Alamos National Laboratory, Preprint Archive, Condensed Matter (2007), 1-11, arXiv:0710.5769v1  
b) J. Phys. D: Appl. Phys 41 (2008), 035002
  
9. F. Casper, and C. Felser  
*Giant magnetoresistance and extraordinary magnetoresistance in inhomogeneous semiconducting DyNiBi*  
Los Alamos National Laboratory, Preprint Archive, Condensed Matter (2007), 1-3, arXiv:0709.4182v1
  
10. F. Casper, and C. Felser  
*Magnetic and electronic properties of RENiBi (RE=Pr, Sm, Gd - Tm, Lu) compounds*  
Z. Anorg. Allg. Chem., submitted

### 3 Calculation Details

Self-consistent band structure calculations were carried out using the full potential linear augmented plane wave (FLAPW) method [64]. The calculations were performed using the Perdew-Burke-Ernzerhof implementation of the generalized gradient approximation (GGA) [65]. The muffin-tin radii (RMTs) of the rare earth, transition metals and  $sp$  – elements were set at 2 - 2.5 Bohr. The self-consistent calculations employed a grid of at least 5000 total k-points within the primitive wedge of the Brillouin zone. Finally, the LDA +  $U$  self interaction correction (SIC) scheme was used to account for the orbital dependence of the Coulomb and exchange interactions as described by Anisimov *et al.* [66]. In this work, an  $U = 6.7$  eV and  $J = 0.7$  eV for the  $f$  – orbitals of the rare earth atoms was applied, values that have been obtained by valence band – XPS measurements (see figure 8.4c). The  $U$  was neglected when calculating the electric field gradient (EFG), because only then WIEN2K gives the correct algebraic sign for the EFG value. Structural optimizations for all compounds showed that the calculated lattice parameter deviates from the experimental one only marginally. On the other hand in the case of the half-Heusler compounds, a position swap between two atoms with strong differing atom radii (e.g. swapping Er and Ni in the ErNiBi compound) leads to a change in the lattice constant. Thus for more than 60 compounds calculations for this thesis were done using the WIEN2K program.

Density functional theory-based electronic structure calculations were performed using the linear muffin tin orbital method [67] within the local spin density approximation. The crystal structure inputs for the calculations were obtained from experimental data, except when hypothetical structures are considered. For certain orbitals, the so-called downfolding procedure [68] was applied. In the LMTO-ASA procedure, the space of the unit cell is filled using both atomic spheres as well as empty spheres whose centers and radii are determined automatically. The empty spheres were described using a  $1s$  orbital basis with  $2p$  downfolding. Crystal orbital Hamiltonian populations (COHP) [69] and the electron localization function(ELF)[70, 71] were used to obtain insights into bonding in terms of the strengths of individual bonds as well as in real space. In order to avoid unphysical COHP interactions between empty spheres and atoms, all empty sphere orbitals were kept downfolded for COHP calculations.

As the cubic half-Heusler compounds and the hexagonal LiGaGe compounds are in the main focus, the possible “simple” antiferromagnetic ordering structure used for band structure calculations of these compounds will be described. For ferromagnetic compounds the original unit cell can be used for the band structure calculations.

### 3.1 Antiferromagnetic ordering structure of half – Heusler compounds

For the *REME* compounds with 18 valence electrons, the magnetic moment is exclusively due to localized *4f* electrons [28]. The rare earth atom not at the  $4c$  ( $\frac{1}{4}\frac{1}{4}\frac{1}{4}$ ) position in any of these compounds because of the size. Taking this into account there is only one possible simple antiferromagnetic ordering structure, displayed in figure 3.1. Such a magnetic structure was found for example in *RENiSb* [5] and *ErAuSn* [72].

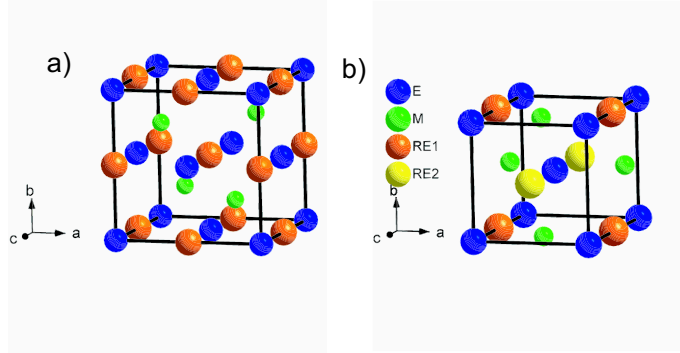


Figure 3.1: MgAgAs structure of *REME* compounds a) and the corresponding simple antiferromagnetic structure b) (Spin of *RE1* inverse to spin of *RE2*)

The antiferromagnetic unit cell has the tetragonal space group  $P -4 m 2$ . The axes are  $a = b = \frac{a_{org}}{\sqrt{2}}$ ,  $c = a_{org}$  and the atomic positions *RE1* on  $1b$  ( $\frac{1}{2}, \frac{1}{2}, 0$ ), *RE2* on  $1d$  ( $0, 0, \frac{1}{2}$ ), *M* on  $2g$  ( $0, \frac{1}{2}, \frac{1}{4}$ ), *E* on  $1a$  ( $0, 0, 0$ ) and  $1c$  ( $\frac{1}{2}, \frac{1}{2}, \frac{1}{2}$ ). The spin of *RE1* is the inverse of the spin of *RE2*.

### 3.2 Antiferromagnetic ordering structure of LiGaGe compounds

Figure 3.2 shows the three possible simple magnetic unit cells for antiferromagnetic ordering of the LiGaGe structure. The magnetic ordering could be either within the  $a - b$  layer (perpendicular to the  $c -$  axis, HEX1) or parallel to the  $c -$  axis. For the latter the spins could be either similar (HEX2) or alternating (HEX3) along the  $c -$  axis. These spin alignments for *REME* compounds with LiGaGe structure are discussed in detail in [73].

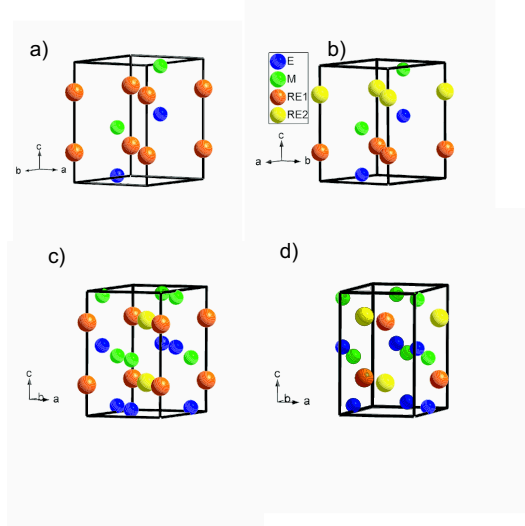


Figure 3.2: a) LiGaGe structure of *REME* compound and the corresponding simple antiferromagnetic structures for b) HEX1 c) HEX2, and d) HEX3 (see text for details)

Table 3.1: Unit cell parameters for the antiferromagnetic structure of *REME* compounds with LiGaGe structure.

Name	SG	axes			Atomic positions			
		a	b	c	RE1	RE2	M	E
HEX1	P3m1	$a_0$	$a_0$	$c_0$	$1a (0,0,\frac{1}{4})$	$1a (0,0,\frac{3}{4})$	$1c (\frac{2}{3},\frac{1}{3},z_1)$ $1d (\frac{1}{3},\frac{2}{3},z_1+\frac{1}{2})$	$1c (\frac{2}{3},\frac{1}{3},z_2)$ $1d (\frac{1}{3},\frac{2}{3},z_2+\frac{1}{2})$
HEX2	Pmc21	$a_0$	$\sqrt{3}a_0$	$c_0$	$2a (0,0,\frac{1}{4})$	$2b (\frac{1}{2},\frac{1}{2},\frac{3}{4})$	$2a (\frac{1}{2},\frac{1}{6},z_1)$ $2b (0,\frac{2}{3},z_1)$	$2a (\frac{1}{2},\frac{1}{6},z_2)$ $2b (0,\frac{2}{3},z_2)$
HEX3	Pmn21	$a_0$	$\sqrt{3}a_0$	$c_0$	$2a (0,\frac{3}{4},\frac{1}{4})$	$2a (0,\frac{3}{4},\frac{3}{4})$	$2a (\frac{1}{2},\frac{11}{12},z_1)$ $2a (\frac{1}{2},\frac{5}{12},z_1)$	$2a (\frac{1}{2},\frac{11}{12},z_2)$ $2a (\frac{1}{2},\frac{5}{12},z_2)$

For all structures the spin of *RE1* is inverse to spin of *RE2*,  $z_1$  and  $z_2$  are compound dependent structure parameters and determine the puckering of the layers (see chapter 5.4).



## 4 Experimental Details

Polycrystalline *REME* samples were prepared by arc melting the pure elements under a dry argon atmosphere at  $10^{-4}$  mbar. In case of bismuth and antimony containing compounds, a slight excess ( $\approx 5\%$ ) was used to compensate the loss during the arc melting. The ingots were wrapped in tantalum foil, sealed in evacuated silica quartz tubes and then annealed. Single crystals were grown with the flux method.

The structure was investigated by means of powder x-ray diffraction (XRD) using a Bruker Axis D5000 operating in transmission mode (Cu –  $K_\alpha$  radiation,  $\lambda = 154.0598$  pm) and a Bruker Axis D8 operating in reflection mode (Mo –  $K_\alpha$  radiation,  $\lambda = 70.9317$  pm). The experimental x – ray patterns were refined by using the FULLPROF program [74].

X – ray photoemission spectroscopy (XPS) was performed by using Mg  $K_\alpha$  radiation to check the composition of the samples. Valence band XPS was used to check the energy of the  $f$  – orbitals. For this and all other other spectroscopic investigations the samples were cut into small discs, polished and bombarded in situ with  $\text{Ar}^+$  ions to remove the native oxide.

Variable temperature magnetic susceptibility measurements were performed in the range from 1.8 K to 300 K and magnetic fields up to  $5.57 \times 10^6$   $\text{Am}^{-1}$  using a Quantum Design MPMS XL SQUID magnetometer. The experimental data were corrected for diamagnetism using Pascal’s constants [75].

The resistance measurements and magneto resistance measurements were performed using the four point probe method. The samples were measured using a Quantum Design PPMS Model 6000 operating in the 5 K to 300 K temperature range in magnetic fields up to  $7.17 \times 10^6$   $\text{Am}^{-1}$ . For the resistivity measurements the samples were cut with a diamond wire saw into small bars ( $\approx 10 \times 1 \times 1$  mm) and polished.

Ultraviolet photo electron spectroscopy (UPS) measurements have been performed at the CP-NIM beamline of BESSY (Berlin). The beam line provides ultraviolet radiation in the energy range from 4 eV to 35 eV. For further details see [76].

Mössbauer measurements of powder samples were performed in transmission geometry using a constant-acceleration spectrometer and a helium bath cryostat.  $^{119}\text{Sn}$  Mössbauer spectra were measured using a 10 mCi  $^{119m}\text{Sn}$  ( $\text{CaSnO}_3$ ) source on the samples, placed in a flow-gas cryostat. Recoil 1.03 Mössbauer analysis software was used to fit the experimental spectra [77]. The  $^{155}\text{Gd}$  Mössbauer spectra were recorded using a  $^{155}\text{Eu} / ^{154}\text{SmPd}_3$  source. The  $^{197}\text{Au}$  Mössbauer measurements were performed using a  $^{197}\text{Pt} / \text{Pt}$  source produced by neutron irradiation of Pt foil. During the measurements, both the source and samples were kept at 12 K in a cryostat equipped with a closed cycle refrigerator. The  $^{155}\text{Gd}$  and  $^{197}\text{Au}$  Mössbauer spectra were computer-fitted using MossWin software [78].



## 5 Searching for the Hexagonal Analogues of Half-Metallic Half Heusler $XYZ$

An important fundamental question is what makes some ferromagnets half-metals, whilst others are not. This question has been addressed across large classes of materials such as the system  $\text{Fe}_{1-x}\text{Co}_x\text{S}_2$  [79, 80], in proposed epitaxial transition metal compounds with the zincblende structure [81], in some chromium chalcogenide spinels [82, 83], and in the half-Heusler [21, 84, 19, 20, 85] and Heusler [86, 84, 87] compounds,  $\text{CrO}_2$  [88, 89] and some members of the colossal magnetoresistive manganites [90]. With the exception of the perovskite manganites, in all these different classes of half-metallic compounds an interesting common theme that emerges. This is the existence of a band semiconductor that is quite proximal in terms of composition and electron count.

As an example, in  $\text{Fe}_{1-x}\text{Co}_x\text{S}_2$  perhaps the first series of compounds that were reported with integer moments on the magnetic substituents [91], the starting point is semiconducting  $\text{FeS}_2$  whose empty  $e_g$  band is populated through Co substitution. Similarly, the basis for zincblende half-metals [81, 92] is the replacement of the cations in a semiconductor with magnetic ions: Half-metallic zincblende CrAs can be considered the magnetic analogue of GaAs, or perhaps even more appropriately, as the magnetic analogue of zincblende ScAs, with the semiconducting gap being retained in the magnetic compound, albeit only in one spin direction. Similar analogies can be drawn for systems such as rutile  $\text{CrO}_2$  [88, 89].

One of the best studied systems of half-metals are the half-Heusler compounds  $XYZ$  exemplified by  $\text{MnNiSb}$  [21]. Whangbo and coworkers pointed [19] out that the 18 electron half-Heusler compounds must be non-magnetic and semiconducting, with earlier hints along these lines from de Groot [93]. Recently, Galanakis [84] has placed these half-Heusler compounds on a firm theoretical footing, suggesting that in the half-metallic compositions, the magnetic moment obtained from the saturation magnetization  $M$ , per formula unit, should vary as  $M = Z_t - 18$  where  $Z_t$  is the total number of valence electrons. The role that covalency plays and that the half-Heusler compounds are both structurally and electronically best treated as an  $X$  ion within a zincblende  $YZ$  structure has recently been investigated [20]. When the  $X$  ion is non-magnetic and  $Z_t = 18$ , the compound is a band semiconductor. If  $X$  is magnetic and  $Z_t \neq 18$ , such as in  $\text{MnNiSb}$  with  $Z_t = 22$ , the compound is a half-metallic ferromagnet, with a magnetic moment of  $4 \mu_B$  per formula unit in the case of  $\text{MnNiSb}$ .

Hexagonal *REME* compounds with cerium, europium, ytterbium, and uranium as the *RE* atom have been investigated in the last twenty years in light of their unusual properties. Examples include valence-fluctuations in  $\text{EuPtP}$  [94], the Verwey type transition in  $\text{EuNiP}$  [9], intermediate-valent  $\text{YbCuAl}$  [95], the 10 K ferromagnet  $\text{CeAuGe}$  [96], the Kondo system  $\text{CePtSn}$  [97], and the heavy fermion material  $\text{CePtSi}$  [98].  $\text{CeRhAs}$  is a Kondo semiconductor in the stuffed wurtzite structure, which undergoes an electronic transition at high temperature and pressure into a metallic phase simultaneously with

a structural transition into the  $\text{TiNiSi}$  structure [99]. The rare-earthPdSb system is particularly interesting since  $\text{CePdSb}$  is a 17K Kondo ferromagnet with a resistance minimum, while many members of this series prepared with other magnetic rare-earths are antiferromagnetic [100]. The tunability of electronic structure and the charge carrier density in this structure type make the compounds of this structure type interesting for magnetoresistance effects [23, 101], and it is likely that they would be a fertile class of thermoelectric compounds as well.

## 5.1 Crystal structures of the hexagonal compounds $RE\text{CuSn}$

A huge variety of the equiatomic intermetallic compounds  $REME$  ( $RE$  = rare-earth,  $M$  = late transition metal element,  $E$  = main group element) crystallize in structure types related to the  $\text{AlB}_2$  family. The ordered superstructures crystallize in the  $\text{LiGaGe}$ ,  $\text{NdPtSb}$  and  $\text{ZrBeSi}$  type structures. The late transition metals and the main group elements form  $\text{Y}_3\text{Z}_3$  hexagons, which are connected in a two-dimensional honeycomb network. Disorder between the transition metals and the main group elements leads to the pseudobinary structure types like  $\text{AlB}_2$ ,  $\text{Ni}_2\text{In}$  or  $\text{CaIn}_2$ . The layers can be planar as in graphite (found in the  $\text{ZrBeSi}$  and  $\text{AlB}_2$  types), weakly puckered ( $\text{NdPtSb}$  type) or strongly puckered with short interatomic distances between the layers leading to a wurtzite-related structure with a three-dimensional network ( $\text{LiGaGe}$ -type). Compared with the compounds with the stuffed zincblende structure, namely the  $\text{C1}_b$  half-Heusler compounds, the  $\text{LiGaGe}$  structure type which is the focus of this contribution has a free lattice parameter, the  $c/a$  ratio. This parameter should be 1.633 for the ideal hexagonal wurtzite structure. Beside the variable  $c/a$  ratio, the free  $z$  parameter of the  $2b$  positions (see Table 5.1) allows different degrees of puckering of the hexagons leading to structures that can vary almost continuously from three dimensional to quasi-two dimensional, with anticipated changes in electronic properties. Due to this reduction in symmetry in comparison with the half-Heusler compounds, a large variety of different structure types are possible as described above. The different superstructures are related via group-subgroup relations as recently reviewed [2]. The bonding features in such materials have been discussed in several overviews [102, 103, 104, 17, 18, 105]. Of the compounds discussed here,  $\text{ScCuSn}$  and  $\text{YCuSn}$  are examples for the puckered  $\text{LiGaGe}$ -type structure, whereas  $\text{LaCuSn}$  is an example for a planar  $[\text{YZ}]^{3-}$  (here  $\text{CuSn}^{3-}$ ) network [106].  $\text{CeCuSn}$  is dimorphic with different degrees of puckering in the low- and high-temperature configurations [107].

Table 5.1: Crystal structures of the compounds whose electronic structures are described here.  $RE$  (Sc, Y, La) at  $(0,0,0)$ , Cu at  $(\frac{2}{3}, \frac{1}{3}, z(Cu))$  and Sn at  $(\frac{1}{3}, \frac{2}{3}, z(Sn))$ . The first three experimental crystal structures are taken from [106].

Compound	Space group	$a(\text{\AA})$	$c(\text{\AA})$	$c/a$	$z(\text{Cu})$	$z(\text{Sn})$
LaCuSn	$P6_3/mmc$	4.582	8.173	1.783	0.75	0.25
YCuSn	$P6_3mc$	4.513	7.274	1.612	0.8148	0.2318
ScCuSn	$P6_3mc$	4.388	6.830	1.557	0.82545	0.22914
Hypothetical structures						
LaCuSn [LiGaGe]	$P6_3mc$	4.583	8.173	1.783	0.78	0.22
LaCuSn [wurtzite]	$P6_3mc$	5.005	8.173	1.633	0.8125	0.1875

Figure 5.1 compares the crystal structure of a typical cubic half-Heusler compound, (a)  $F\bar{4}3m$  TiNiSn, with the crystal structures of two variants of the hexagonal  $REME$  compounds discussed here:  $P6_3mc$  ScCuSn, crystallizing in the LiGaGe-type structure and the planar  $P6_3/mmc$  LaCuSn [106]. TiNiSn is displayed with bonds connecting the zincblende network of Ni and Sn. The Ti atoms stuff the  $(6 + 4)$ -coordinate voids of the zincblende structure. The structure is displayed with the  $[1\ 1\ 1]$  direction pointing up in the plane of the page, in order to emphasize the ABC stacking each of the three  $fcc$  substructures of the half-Heusler structure. ScCuSn can be thought of as comprising a  $\text{Sc}^{3+}$  ion stuffing a wurtzite  $[\text{CuSn}]^{3-}$  substructure where the number of electrons is 18 ( $d^0 + d^{10} + s^2 + p^6$ ). LaCuSn is also an 18-valence electron compound which crystallizes in the ZrBeSi-type structure. In this structure type, compounds with 18 valence electrons are most commonly found.

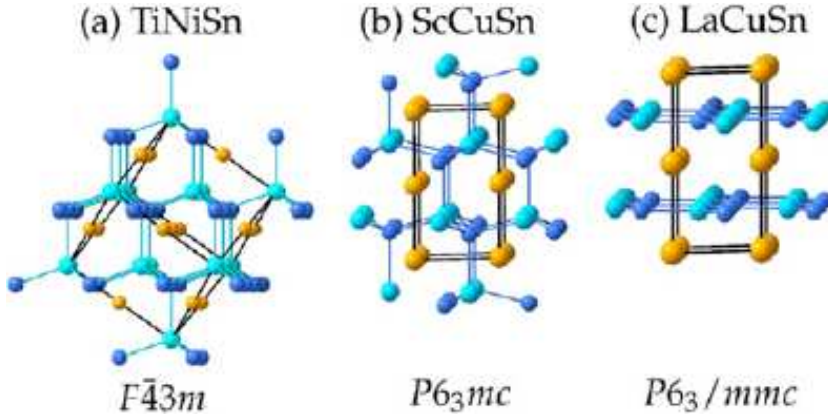


Figure 5.1: Crystal structures of (a) the half-Heusler compound TiNiSn, (b) the filled wurtzite ScCuSn with the LiGaGe structure and (c) LaCuSn, in the ZrBeSi structure type. The structures are depicted in the manner that highlights, respectively, the zincblende NiSn, the wurtzite CuSn and the 'decorated graphite' CuSn networks. The orange spheres are, respectively, Ti, Sc, and La. Light and dark blue spheres represent (Ni/Cu) and Sn.

From the electron count of these 18-electron compounds, we would expect closed shell species similar to the 18-electron half-Heusler compounds: non-magnetic, and semiconducting, at least for  $\text{ScCuSn}$ . In  $\text{LaCuSn}$  the  $[\text{CuSn}]^{3-}$  honeycomb network adopts a planar graphite type layer. This structural change from  $\text{ScCuSn}$  via  $\text{YCuSn}$  to  $\text{LaCuSn}$  is reflected in the  $c/a$  ratio and the  $z$  parameter, listed in Table 5.1. The  $c/a$  ratio decreases with an increase in the puckering.

## 5.2 Electronic structures of the hexagonal compounds $RE\text{CuSn}$

The  $RE\text{CuSn}$  compounds were examined using LMTO calculations. The experimental lattice constants and experimental  $z$  parameters were employed in the input crystal structures to investigate the influence of puckering of the honeycomb  $Y_3Z_3$  networks on the electronic structure. Additionally, calculations were performed for  $\text{LaCuSn}$  in two hypothetical structures described in Table 5.1: the  $\text{LiGaGe}$  structure with experimental lattice parameters and hypothetical  $z$  parameters which result in puckered  $\text{Cu}_3\text{Sn}_3$  honeycombs, and an ideal wurtzite structure with the experimental  $c$  parameter, and  $a$  and  $z$  chosen so that the ideal wurtzite structure is obtained ( $c/a = 1.633$ ). In this ideal structure, all  $\text{CuSn}_4$  and  $\text{SnCu}_4$  tetrahedra are regular.

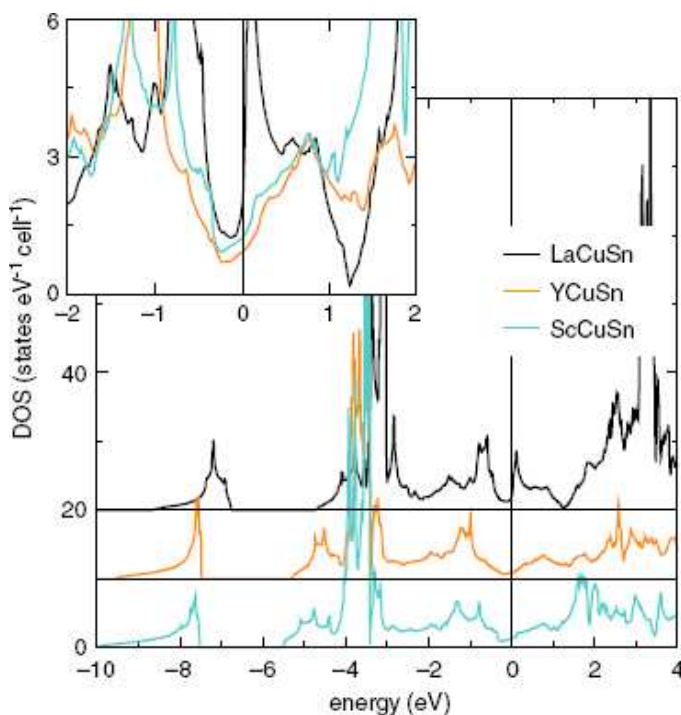


Figure 5.2: Total densities of state obtained from LMTO calculations on the experimental structure of  $\text{LaCuSn}$ ,  $\text{YCuSn}$  and  $\text{ScCuSn}$ . The DOS in the main panel are offset on the ordinate for clarity. The inset shows the DOS of the three compounds in a region close to  $E_F$ .

In the three panels of Figure 5.2, the densities of states (DOS) near the Fermi energy  $E_F$  for LaCuSn, YCuSn and ScCuSn calculated for the experimental structures are compared. The trends in the electronic structure as the CuSn networks in these structures are increasingly puckered. All compounds have a noticeable pseudo band gap at  $E_F$ , with a more pronounced gap in the more puckered Y and Sc compounds. Projections of the densities of state on the different orbitals (not displayed) reveal that the valence band has mainly Sn  $p$  character. The Sn  $s$  states are separated by a gap from the valence band at around -8eV. The bottom of the valence band is built from Sn  $p$  states. Cu  $d$  states lead to spikes in the electronic structure around -3.5 eV (ScCuSn) or -3 eV (LaCuSn). The Cu  $d$  bands are very flat with an overall dispersion of 0.5 eV. In the three-dimensional compound ScCuSn all Sn  $p$  states contribute to the states below and above the copper states. In the two-dimensional LaCuSn, the bottom of the valence states around -4 eV has a pronounced Sn  $p_z$  character, whereas the top of the valence band is built mainly from Sn  $p_x$  and  $p_y$  states. Sc or rare-earth  $d$  states form the conduction band with a width around 5 eV and have a small contribution to the Sn  $p$  states below  $E_F$ . From the density of states we can conclude that a description of the compound as  $X^{3+}$  ion within a wurtzite or ‘decorated graphite’  $[\text{CuSn}]^{3-}$  substructure is appropriate. The total DOS of these hexagonal compounds look very similar to those of the half-Heusler compounds [20], with some differences in the projected densities due to the different electronegativities of the constituent elements.

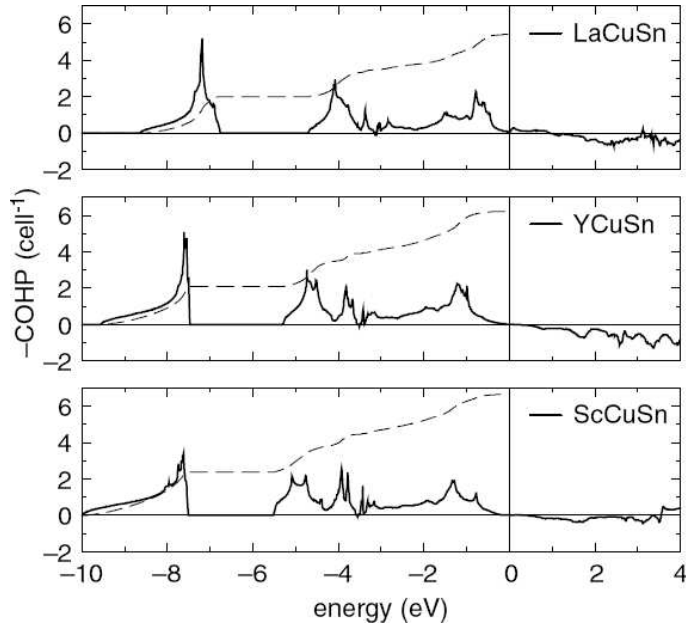


Figure 5.3: COHPs of the Cu-Sn interaction in the three compounds LaCuSn, YCuSn and ScCuSn.

The similarities and differences in the electronic structure of the three compounds are further emphasized through an analysis of the Cu-Sn COHPs of the three stannides

displayed in Figure 5.3. Cu-Sn is the main bonding interaction in these compounds and bonding and antibonding states are separated by the Fermi energy. The dashed line in this figure is an integration of the COHP up to the  $E_F$ , yielding a number that is indicative of the strength of the bonding. The extents of the bonding and the antibonding states of the Cu-Sn COHPs are slightly larger in the puckered compounds compared with the planar LaCuSn. Integrating the COHPs, the strongest bonding interaction seems to be in the planar LaCuSn. The planar Cu-Sn layers seem to lead to a stronger Cu-Sn interaction than the puckered Cu-Sn layers. However, the total bonding interaction seems to be stronger in the puckered compounds. Cu-Sn interactions are non-bonding around and above  $E_F$  and therefore do not contribute to the states around  $E_F$ . In YCuSn and ScCuSn, the other pairwise interactions are significantly smaller: the X – Cu interaction is only 10%, and the X – Sn interaction is around 20% of the Cu-Sn interaction. The X – Cu interaction is bonding below  $E_F$  and small and slightly bonding above  $E_F$ . The bonding interactions in the hexagonal compounds ScCuSn and YCuSn are similar to what are found in the half-Heusler compounds [20]. A much stronger La – Cu interaction is found in the planar compound LaCuSn (not shown). The La – Cu interaction has a strong bonding interaction leading to the high density of states peak slightly above  $E_F$ . The La – Sn states build the top of the valence band and are responsible for reducing the magnitude of the pseudogap in this compound. It is clear from this discussion that YCuSn and ScCuSn are electronically well described as filled wurtzite compounds, with pseudogaps at  $E_F$  between the bonding and antibonding states.

### 5.3 The influence of puckering on the band structure and the electron localization function

The fact that the puckering of the Cu – Sn layer seems to be responsible for the metallic or semimetallic behavior of hexagonal 18-electron compounds has motivated us to look more closely at the influence of puckering on the band structure and the gap of these compounds. Here the band structure of LaCuSn in the experimental structure and in the hypothetical LiGaGe-type and the wurtzite-type structures is discussed. Figure 5.4 displays the band structure of (a) LaCuSn with the experimental ZrBeSi-type structure, (b) hypothetical LaCuSn with the LiGaGe-type and (c) LaCuSn with the ideal wurtzite type structure. These structures are described in Table 5.1. LaCuSn in its experimental structure is clearly a metal in the  $\Gamma - K - M - \Gamma$  direction and shows a gap of nearly 0.3 eV along the direction at the surface of the Brillouin zone  $A - L - H - A$ . In the LiGaGe structure the compound would be a semimetal due to the dipping of the conduction band at the M point and the valence band at the  $\Gamma$  point. In the hypothetical wurtzite structured LaCuSn becomes semiconducting. A closer view of the bands and their eigenvectors around  $E_F$  shows that the metallicity is due to an overlap between the conduction band with mainly La  $d_{x^2-y^2}$  and  $d_{3z^2-1}$  characters and the Sn  $p_x$  and  $p_y$  valence bands. Symmetry induces a metal to semiconductor transition by going from the ZrBeSi-type structure to the LiGaGe-type structure. For the experimental structure the

La band dips below the Fermi energy at the M point with mainly  $d_{3z^2-1}$  character and the Sn  $p_x$  and  $p_x$  bands cross  $E_F$  around . It is surprising that the overall band dispersion in the planar layers is much higher compared with the puckered layers. However a detailed look at the eigenvectors leads to a simple explanation. In the case of the planar Cu – Sn layers the bands with Sn  $p_x$  and  $p_y$  contribution have a larger dispersion compared with the puckered layers. The strength of this interaction depends on the bonding distance and the effective overlap of the orbitals; both are stronger in the case of the planar layers. The strong sigma type bonding interaction between Sn and Cu pushes the valence band above the Fermi level at the  $\Gamma$  point. The conduction band which is derived from La  $d_{3z^2-1}$  displays a dispersion of nearly 2 eV and dips below  $E_F$  along the  $\Gamma$  to the M direction.

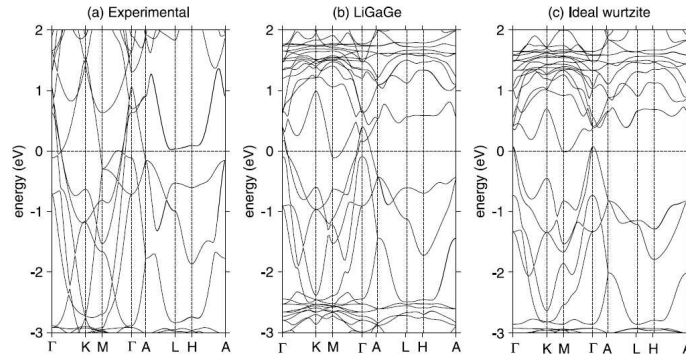


Figure 5.4: Band structures of experimental and hypothetical LaCuSn structures.

The same the La  $d_{3z^2-1}$  band of the puckered structures has a much smaller dispersion of 0.5 eV and touches the Fermi energy slightly at the M point. The most important point is that the degeneracy at the M point between the La  $d_{3z^2-1}$  and the Sn  $p_x$  band is lifted by reducing the symmetry from  $P6_3/mmc$  to  $P6_3mc$ , which renders the opening of the gap possible in the LiGaGe-type and wurtzite-type structure. In a manner similar to the half-Heusler compounds, the hexagonal compounds display an indirect gap, here between the  $\Gamma$  and the M point.

By puckering the structure in going from the graphite type structure via LiGaGe to the ideal wurtzite-type structure the overlap between the conduction and the valence band becomes smaller and the symmetry is reduced. The compounds with LiGaGe structure can show semiconducting or semimetallic behavior, which is experimentally and theoretically found for CePdSb [108] and CeRhAs [99]. Introducing  $f$  – elements like Gd leads to half metallic ferromagnets for example in GdPdSb [30].

Real space visualization of the electronic structure employed the electron localization function (ELF) for LaCuSn in Figure 5.5(a) for the experimental ZrBeSi-type and in Figure 5.5 (b) for the hypothetical wurtzite structure. The value of localization runs from 0 (no localization, deep blue) to 1 (high localization, white). The isosurface of 0.75 is displayed here.

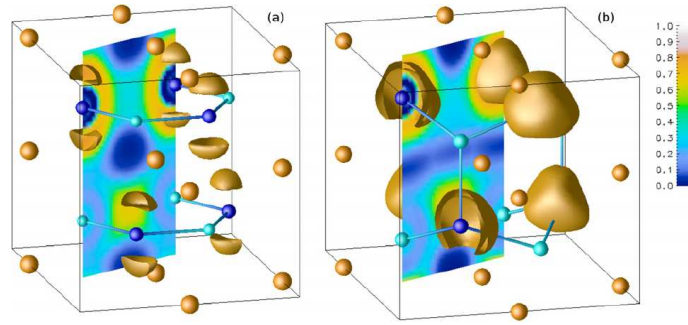


Figure 5.5: Electron localization functions (ELFs) of the valence electrons of LaCuSn in (a) the experimental crystal structure and in (b) the hypothetical wurtzite structure. The ELF isosurface is displayed for a value of 0.75.

The colored map in the background is the ELF shown on a  $(1\ 1\ \bar{2}\ 0)$  plane to visualize the bonding interaction along the Cu–Sn network. For the ZrBeSi type structure, Figure 5.5(a), the Sn  $p$  electrons perpendicular to planar Cu–Sn layer are strongly localized. These  $p$  states interact strongly with La  $d_{3z^2-1}$  states with the layer, and are responsible for closure of the gap and metallicity of the compound. In Figure 5.5(b), a clear evidence for highly covalent and three-dimensional bonding between Cu (cyan) and Sn (blue) in the wurtzite substructure of the wurtzite-type LaCuSn can be seen. As observed in the half-Heusler compounds, the localization is closer to the more electronegative Sn atom [20].

The valence charge densities displayed in Figure 5.6(a) and (b) are again very similar to the valence charge densities of the half-Heusler compounds. Because of the filled  $d$  shells on Cu it forms nearly large spherical blobs around that atom, visualized for a charge density of  $0.025\ e\text{\AA}^{-3}$ . These blobs of charge are pulled out into four strongly localized (as seen from the coloring) lobes arranged tetrahedrally and facing Sn in (b), whilst in the LiGaGe structure, the bonding interaction in the third dimension is removed, leading to three lobes arranged trigonally in the plane and facing the Sn in the plane.

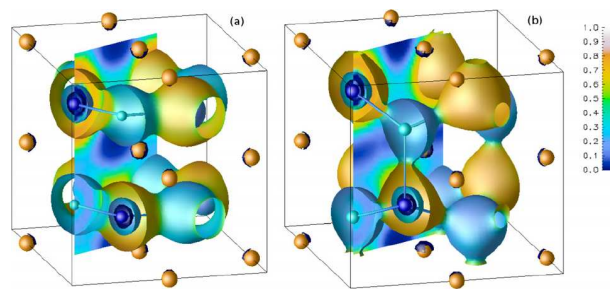


Figure 5.6: Electron density isosurfaces plotted for values of  $0.025\ e\text{\AA}^{-3}$  for LaCuSn in (a) the experimental crystal structure and in (b) the hypothetical wurtzite structure. The electron density is colored according to the degree of localization.

## 5.4 Conclusion

A systematic examination of *REME* compounds with hexagonal structures: LaCuSn, YCuSn and ScCuSn was carried out, and it was demonstrated that 18-electron compounds can become semiconductors depending on the degree of puckering of the  $[\text{CuSn}]^{3-}$  substructure. The most instructive way of considering these systems is to think of them as being built up of a wurtzite  $[\text{YZ}]$  framework that is filled with the electro positive  $X$ . An effective strategy for new half-metals, in analogy with half-Heusler half-metals, would be to fill these wurtzite-derived structures with magnetic ions.



# 6 GdAu*E* Compounds

## 6.1 Introduction

Intermetallic gadolinium compounds are promising candidates for magnetocaloric materials (magnetocaloric effect; MCE) [109, 110] and magnetoelectronics [111]. The recent developments in this field of magnetocalorics were reviewed earlier [112]. Although gadolinium and gadolinium-based solid solution alloys are the excellent candidates for MCE materials, some intermetallic gadolinium compounds show adiabatic temperatures that are up to 30% higher than those for elemental gadolinium. A highly interesting compound in that respect is the giant-MCE material  $\text{Gd}_5\text{Ge}_2\text{Si}_2$  [113]. Another class of materials concerned the  $\text{Fe}_2\text{P}$  related pnictide solid solution  $\text{MnFeP}_{0.5}\text{As}_{0.5-x}\text{Ge}_x$  [114].

Recently, a more systematic investigation of the structure-property relations of gadolinium compounds  $\text{GdAu}E$  ( $E = \text{Sn, In, Cd, Mg}$ ) has been started.  $\text{GdAuSn}$  crystallizes like the many other 18 electron compounds in the  $\text{LiGaGe}/\text{NdPtSb}$  Structure ( $\text{P6}_3\text{mc}$ ) [115, 23] and orders antiferromagnetic at  $T_N = 26$  K [116, 117]. The other three compounds follow the  $\text{Fe}_2\text{P}/\text{ZrNiAl}$  structure. The isotypic compounds  $\text{GdAuMg}$  [118],  $\text{GdAuCd}$  [119], and  $\text{GdAuIn}$  [120] are antiferromagnetic with distinctly different magnetic ordering temperatures of  $T_N = 81.1$  K,  $T_N = 66.5$  K, and  $T_N = 12.5$  K, respectively. The similarity in their crystal structure is in spite of the different bonding behavior of Mg, Cd and In. Mg is more electropositive as compared to Cd and In.  $\text{GdAuMg}$  and  $\text{GdAuCd}$  (16 valence and 7  $f$ -electrons) have the same number of valence electrons, whereas the indium compound exhibits 17 valence electrons. There is not much known about the structure – property relationship of these compounds. More recently Tjeng et al have systematically studied the band structure of  $\text{GdAuMg}$  within local density approximation LDA and LDA+ $U$  with a view to understanding the role of partial density of states near the Fermi energy [121]. They have found Gd in  $\text{GdAuMg}$  is in a half filled  $4f^7$  configuration and the states in the vicinity of Fermi energy are unaffected by the Gd  $4f$  states.

## 6.2 Crystal structures and details of the calculations

The intermetallic compounds  $\text{GdAuMg}$ ,  $\text{GdAuCd}$ , and  $\text{GdAuIn}$  crystallize in hexagonal  $\text{ZrNiAl}$  type structure. In Figure 6.1, a projection of the  $\text{GdAuMg}$  structure and the corresponding coordination polyhedra are presented as examples. Both crystallographically independent gold sites have a trigonal prismatic coordination by gadolinium and  $E$  atoms, respectively. The two different trigonal prismatic building groups are shifted with respect to each other via half the translation period  $c$ . The trigonal prisms are capped by three additional atoms on the rectangular faces leading to a coordination number of nine, which is often observed for related intermetallics.

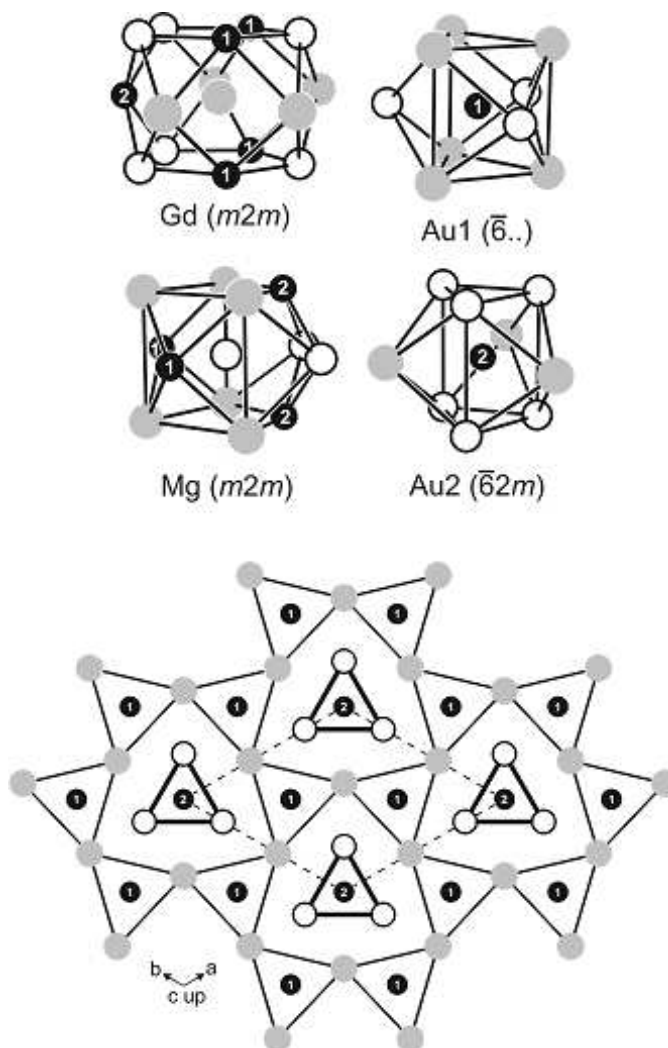


Figure 6.1: Projection of the GdAuMg structure onto the  $xy$  plane. All atoms lie on mirror planes at  $z = 0$  (thin lines) and  $z = 1/2$  (thick lines). Gadolinium, gold, and magnesium atoms are drawn as grey, black, and open circles, respectively. The trigonal prisms around the gold atoms are emphasized. The coordination polyhedra are drawn in the upper part and the site symmetries are indicated.

The largest differences between the GdAuMg, GdAuCd and GdAuIn structures are the Au –  $E$  distances (Table 6.1). There are two inequivalent Au atoms in the cell. One Au atom has three (in plane) and the other has six nearest  $E$  neighbors. Each has two different set of distances for two inequivalent Au atoms. In the three compounds the Au –  $E$  distances cover the range from 277 to 291 pm.

Table 6.1: Interatomic distances (pm) in the structures of GdAuE ( $E = \text{In, Mg and Cd}$ ) [118, 119, 120]. All distances within the first coordination sphere are listed

			GdAuMg	GdAuCd	GdAuIn
Gd:	4	Au1	307.6	306.4	306.8
	1	Au2	312.0	312.4	312.8
	2	$E$	330.6	326.1	325.5
	4	$E$	341.3	338.0	338.8
	4	Gd	395.1	396.0	404.6
	2	Gd	412.7	405.1	397.8
	Au1	3	$E$	290.8	290.2
6		Gd	307.6	306.4	306.8
Au2	6	$E$	277.8	280.4	281.6
	3	Gd	312.0	312.4	312.8
$E$	2	Au2	277.8	280.4	281.6
	2	Au1	290.8	290.2	289.5
	2	$E$	322.2	326.1	345.2
	2	Gd	330.6	338.0	325.5
	2	Gd	341.3	344.0	338.8

All calculations refer to the GdAuE ( $E = \text{Mg, Cd and In}$ ) compounds, ZrNiAl type, of space group  $P\bar{6}2m$ . The experimental structural parameters that were used as starting values for the calculations are displayed in Table 6.2.

Table 6.2: Experimental crystal structures of GdAuE ( $E = \text{Mg, Cd and In}$ ), space group  $P\bar{6}2m$  (No. 189); Gd in  $(x, 0, 0)$ ; Au1 in  $(\frac{1}{3}, \frac{2}{3}, \frac{1}{2})$ ; Au2 in  $(0, 0, 0)$ ; E in  $(x, 0, \frac{1}{2})$ .

Compounds	a(Å)	b(Å)	x (Gd)	x(E)	Reference
GdAuMg	7.563	4.127	0.4125	0.7540	[118]
GdAuCd	7.701	3.960	0.4057	0.7421	[119]
GdAuIn	7.698	3.978	0.4064	0.7411	[120]

To study the electronic structure of antiferromagnetic GdAuE ( $E = \text{Mg, Cd and In}$ ), a periodic supercell has been used. This can be constructed by doubling the lattice parameters in all three directions. Where Gd atoms lying in one plane are aligned parallel to each other and the next nearest neighbor Gd atoms sitting at other planes are aligned in opposite direction. Such arrangement of spin of Gd atoms avoids the possibility of a spin frustration state within the triangular network of Gd atoms.

### 6.3 Results and Discussion

The total energies of GdAuE ( $E = \text{Mg, Cd and In}$ ) in the ferromagnetic and antiferromagnetic states were calculated using LMTO and full potential linear augmented plane wave scheme within Wien2k. The differences between total energies for ferromagnetic and the antiferromagnetic GdAuE are presented in Table 6.3. The differences in the energies are small in both the calculations. In fact Wien2k does not give the correct ground state found experimentally and therefore a competition between the two ground states can not be excluded. Only LMTO gives the correct ground state for GdAuMg [122]. When compared to the other compounds, it should be noted that GdAuMg clearly exhibits the strongest antiferromagnetic behavior.

Table 6.3: Total energy difference  $\Delta E$  (in eV) between the ferromagnetic (FM) and antiferromagnetic (AFM) structures of GdAuE ( $E = \text{Mg, Cd and In}$ ) and corresponding Neel temperature in Kelvin.

Compounds	$\Delta E$ (LMTO)	$\Delta E$ (Wien2k)	$T_N$
GdAuMg	-0.0941	0.00821	81.1
GdAuCd	0.0087	0.0100	66.5
GdAuIn	0.0291	0.0023	12.5

#### 6.3.1 Density of states

The DOS for each GdAuE compound is displayed in the panels of Figure 6.2 for the different  $E$  atoms with orbital projected  $d$  and  $f$  states of Gd. In every one of the three compounds, the DOS exhibits a narrow band composed largely of Gd  $4f$  orbitals clustered at approximately -7.9 eV below the Fermi energy (taken as the top of the valence band and set to zero on the energy axis in all the plots). The density of states indicating that the Gd has localized nature of  $f$  electrons and half filled  $4f^7$  state as was found from experiment and previous calculations [30, 121]. Thus the  $4f$  electrons are not relevant for the states at the Fermi energy.

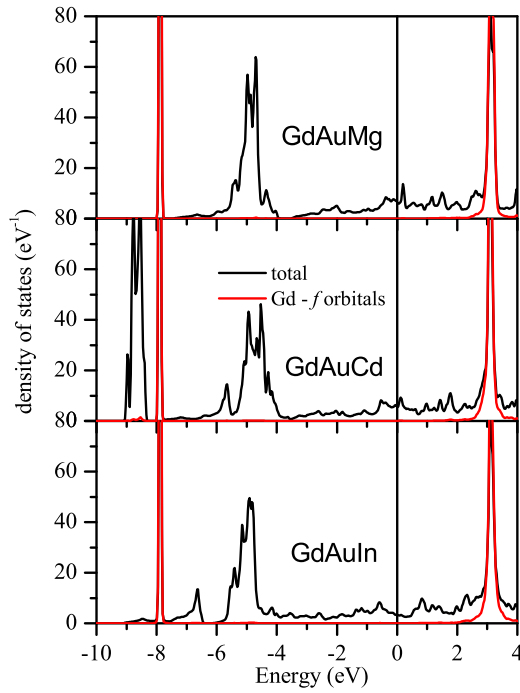


Figure 6.2: LDA +  $U$  total DOS and orbital projected Gd  $f$  DOS for GdAu $E$  ( $E = \text{Mg}, \text{Cd}$  and  $\text{In}$ ) compounds. In these and in other plots, the top of the valence band is taken as zero on the energy axis.

The orbital projected density of states of the valence electrons is shown in Figure 6.3. In GdAuMg, the density of states shows a band composed largely of Au  $5d$  and  $6s$  orbitals and a small contribution from Mg  $3s$   $3p$  orbitals ranging from  $-7$  eV to  $-4$  eV below the Fermi energy, while most of the Mg  $s$  and  $p$  states are found around the Fermi energy. The metallicity of the compound is mainly due to Mg  $s$  and  $p$  states, which appear at the Fermi energy.

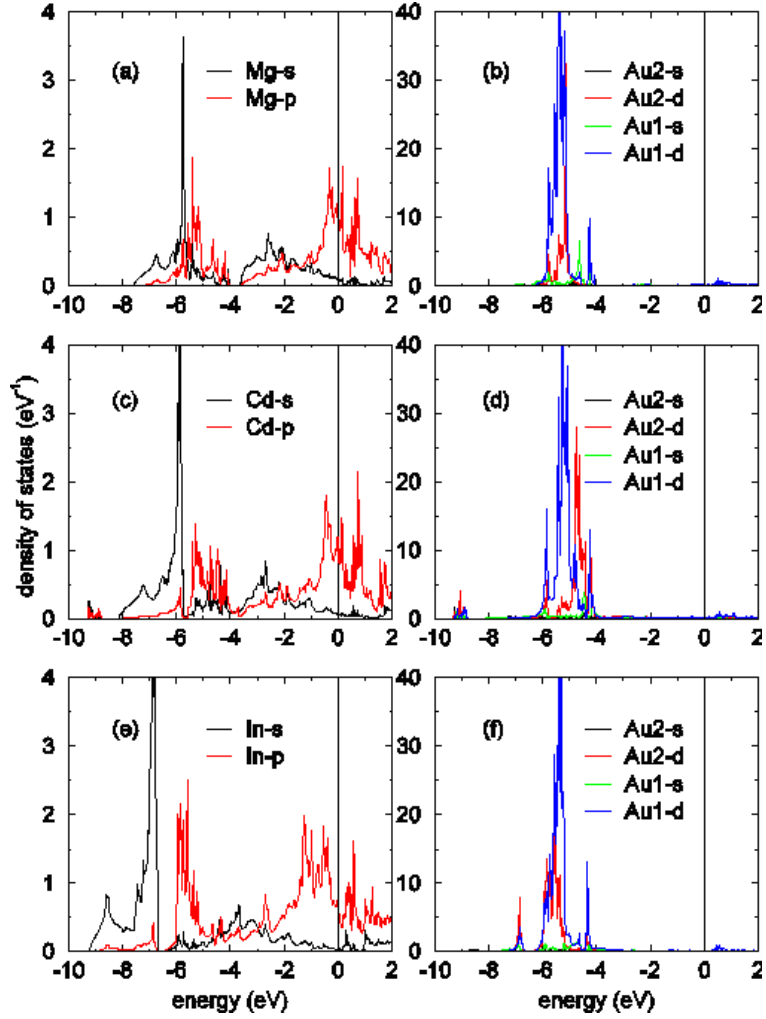


Figure 6.3: LDA orbital-projected density of states for GdAuMg (a) (b), GdAuCd (c) (d) and GdAuIn (e) (f). The orbitals that contribute to the DOS are labelled.

The fact that there are small  $d$  states found at  $-7$  eV close to the In  $s$  states (see in Figure 6.3(e) and (f)) is remarkable. Some of In  $p$  states are found with the Au  $d$  states over a range of  $-6.5$  to  $-4$  eV below Fermi energy. In  $s$  states are less disperse in GdAuIn compared with Mg  $s$  states in GdAuMg. Correspondingly fewer Au  $d$  states in this region of energy (see Figure 6.3),  $-7$  eV with respect to the Fermi energy reflect the smaller dispersion of the In  $s$  states. One observe more pure In  $s$  states in the In compound, whereas in the Mg case, some of the Mg  $s$  and Au  $d$  states are found at the same energies. There is a separation between In  $s$  and  $p$  states in GdAuIn compound. Despite this separation between the  $s$  and  $p$  states of In in GdAuIn compared to Mg  $s p$  in GdAuMg, it is In that has more localized (in energy)  $s$  states as seen from the narrower DOS of In  $5s$  compared with Mg  $3s$ .

In the Cd compound, the  $d$  states of two inequivalent Au atoms are not at the same

energy like Mg and In compounds, resulting in two narrower  $d$  states. The two inequivalent Au atoms in GdAuCd have Cd atoms in the surroundings; one has six Cd atoms in different planes and the second has three Cd in the same plane. The Cd atom has a completely filled shell structure. Therefore the Au atom which sits near the Cd surroundings (not in the same plane) feels more repulsion which causes the shift of the Au  $d$  states. Due to this two more  $d$  states in Cd compound can be found similar to those found in pure Au. Cd  $4d$  states are centered at -9 eV with some Au  $5d$  states. Cd  $5s$  and  $5p$  states are appear close to the Fermi energy.

The most obvious difference in the DOS of the two compounds (GdAuMg and GdAuIn) is the presence of filled  $5s$  orbitals in indium, indicated by a narrow peak at -7 eV below the Fermi energy. The  $5d$  states of gold in the magnesium and indium compounds are distinctly broader than those of the cadmium compound. In the magnesium and indium compounds, the  $5d$  states of the gold atoms trace the  $s p$  states of magnesium and  $p$  states of indium. One observes more pure Au  $5d$  states in the cadmium compound. Gd  $5d$  states and  $E s p$  states form the main contributions at the Fermi energy.

### 6.3.2 Chemical Bonding

The nature of interaction is better explored by plotting the COHPs of Au –  $E$  interactions. The COHP can be plotted as a function of the energy and can demarcate different bonding, non-bonding and antibonding contributions for specific pairwise interactions. All COHPs were then scaled by the number of interactions in the unit cell. The Au –  $E$  COHPs of GdAuE for the different  $E$  are displayed in Figure 6.4. A positive COHP represents bonding interactions while a negative COHP represents antibonding interactions.

There are bonding states at the Fermi energy for all the compounds confirming the metallic behavior. These compounds are electronically very stable as seen from a complete absence of any antibonding interaction below the top of the valence band. An interesting feature is the presence of an antibonding component in the In compound just above the Fermi energy, which is not seen in GdAuMg and GdAuCd compounds. This indicates the In  $p$  strongly hybridizes with Au states near the Fermi energy. It is clear from the interatomic distances (Table 6.1) that the GdAuIn has almost two equidistant In atoms around the Au atoms which are shorter than the Au –  $E$  distances in Mg and Cd compounds.

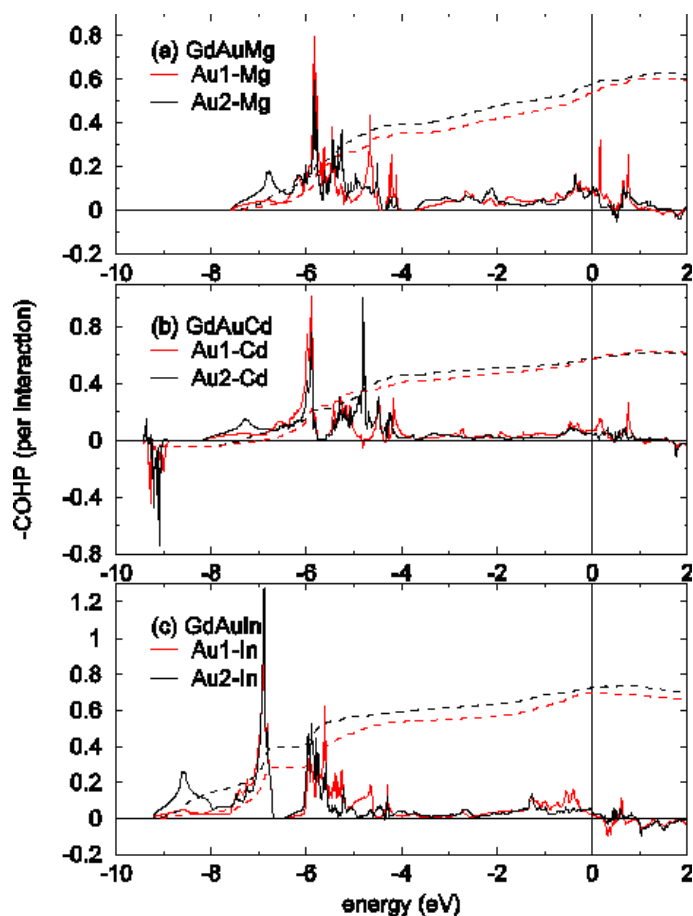


Figure 6.4: Crystal Orbital Hamiltonian Populations (COHPs) for the Au– $E$  interactions in GdAu $E$  ( $E = \text{Mg, Cd and In}$ ). Integrated COHP (ICOHPs) are depicted using broken lines. Note: There are two inequivalent Au atoms in the cell. ICOHPs are obtained by integration of the COHPs from over all valence electrons, i.e., up to the top of the valence band. The values of ICOHPs are (a) Au1–Mg 1.118; Au2–Mg 1.229 (b) Au1–Cd 1.2467; Au2–Cd 1.500 (c) Au1–In 1.08; Au2–In 1.3248 in unit eV per interactions.

In GdAuCd are antibonding states in the COHP below the Fermi energy, centered around -9 eV. When two closed-shell systems interact, one expects that the number of filled bonding states should be exactly compensated by the number of filled antibonding states below the Fermi energy [123, 124]. The presence of antibonding states below the Fermi energy can be inferred as arising from the filled  $d$  orbitals of Cd and filled  $d$  orbitals of Au. The extra electrons in the In  $p$  orbital enhance the extent of the favorable bonding hybridization in GdAuIn by pushing down the  $s$  electron pair from the Fermi energy and making them more localized. The Au – In COHP is more disperse in GdAuIn indicating Au – In hybridization over a broader energy range. In particular, the COHP strength in the region of the In  $s$  states is increased significantly.

The presence of the bonding Au – E states in the COHP of the GdAuMg, as arising due to the lone pair on Mg *s* being degenerate over a number of sites. In the GdAuIn, where the lone pair of In *s* is more localized this interaction is no longer possible up to the extent like Mg – Au in GdAuMg compound. This suggest that from a chemical viewpoint, the Au – E interactions is perhaps greater for Mg and In than for Cd. The dashed lines in the Figure 6.4 are an integration of the COHP up to the Fermi energy, yielding a number that is indicative of the strength of the bonding. The extent of the bonding of Mg and In are different from Au<sub>2</sub>, but so is the value of the integrated COHP: 1.229 eV per interaction for Mg and 1.33 eV per interaction for In compounds. The gold and *E* atoms together build up rigid three-dimensional [AuE] networks in which the gadolinium atoms fill distorted hexagonal channels. The Au–In (282-290 pm), Au–Mg (278-291 pm) and Au–Cd (280-290 pm) distances compare well with the sums of the covalent single bond radii of 283 pm (Au + In), 270 pm (Au + Mg), and 275 pm (Au + Cd) [125]. For GdAuIn, the shorter Au–In distances match perfectly with the sum of the radii, while they are slightly longer for GdAuMg and GdAuCd. From this comparison it can be assumed that there are slightly stronger Au–In interactions in GdAuIn than in GdAuMg and GdAuCd, which can be seen from the Au–E COHP calculations. In GdAuMg, the COHPs between gadolinium and magnesium are much weaker as a result of the longer Gd–Mg distances. The extent of such interactions are small but noticeable in the magnesium and indium compounds.

## 6.4 Conclusion

The electronic structure of the isotypic GdAuE (*E* = Mg, Cd and In) compounds has been investigated. In GdAuMg and GdAuIn, the Au *d* states are broader than those observed in the corresponding cadmium compound. However, the valence band states in the magnesium and indium compounds have a strong Au *d* admixture. In the case of the cadmium compound, states below the top of the valence band have a more pure Au *d* character. In particular, the effect of Au–E covalency in these compounds was examined. The Au *d* states occupy the same energy range as the In and Mg states, suggesting a significant Au–E covalency. The In *s* lone pair in GdAuIn has more localized behavior as compared with Mg *s* in GdAuMg. The electronic structure calculations predict metallic behavior with the appearance of Gd *d*, Mg *s p*, In *p* and Au *s* states at the Fermi energy.



# 7 GdNiSb Compounds

## 7.1 Introduction

Ternary lanthanoid nickel antimonides with the composition  $RENiSb$  have been known for some time. Within this series two different structure types can be found. For  $RE = Gd - Lu$  the cubic MgAgAs structure [126], and for  $RE = Ce - Nd, Sm$  and Gd the hexagonal  $ZrBeSi$  structure [127] (Figure 7.1).

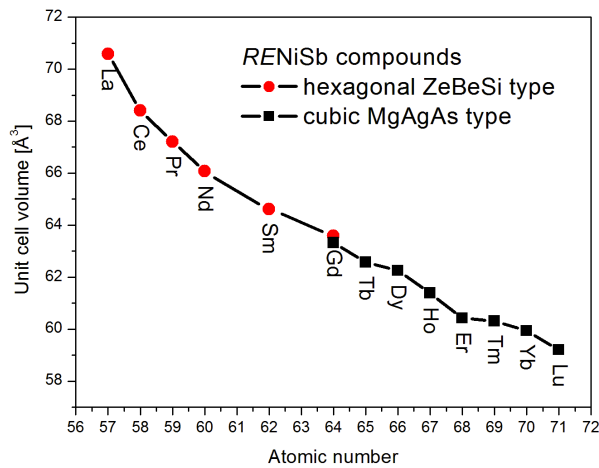


Figure 7.1: Dependence of structure and unit cell volume on the  $RE$  - atom for  $RENiSb$  compounds.

Later it was shown that the compounds with light  $RE$  elements do crystallize in an order variant of the  $AlB_2$  structure. Here the nickel and antimony atoms are ordered on the B position of the  $AlB_2$  structure, resulting in a doubled  $c$  axis ( $ZrBeSi$  structure, Figure 7.2).

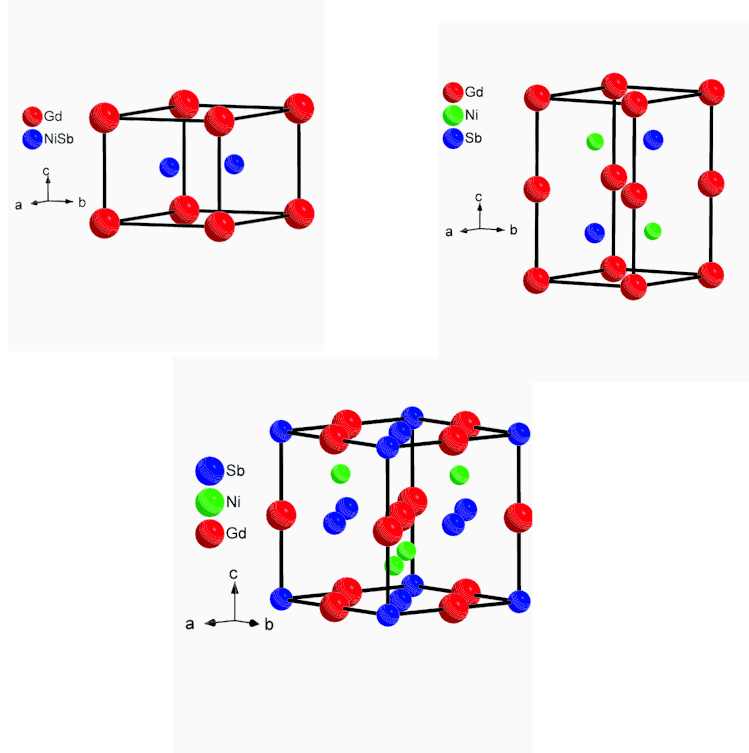


Figure 7.2: Reported structures of GdNiSb:  $\text{AlB}_2$  (top left),  $\text{ZrBeSi}$  (top right) and  $\text{MgAgAs}$  structure (bottom).

Although some measurements have been done on the  $\text{GdNiSb}$  compound [128, 129], the magnetic and electronic properties are still uncertain. The magnetic ordering temperatures of  $T_N = 3.7$  K and  $T_N = 3.3$  K for the compounds with cubic and hexagonal structure, respectively. For both a metallic behavior was found [128].

Here also both structure types have been found, but a separation could not be established under our preparation conditions. Nevertheless,  $^{155}\text{Gd}$  - Mössbauer measurements were performed with a mixed sample.

## 7.2 Band structure calculation

For the  $\text{MgAgAs}$  and  $\text{ZrBeSi}$  structure of  $\text{GdNiSb}$ , band structure calculations were performed (Figure 7.3). The metallic ground state of the hexagonal  $\text{GdNiSb}$  was confirmed. For the cubic  $\text{GdNiSb}$  compound a semiconducting behavior was found, which is in contrast to the above mentioned resistivity measurements.

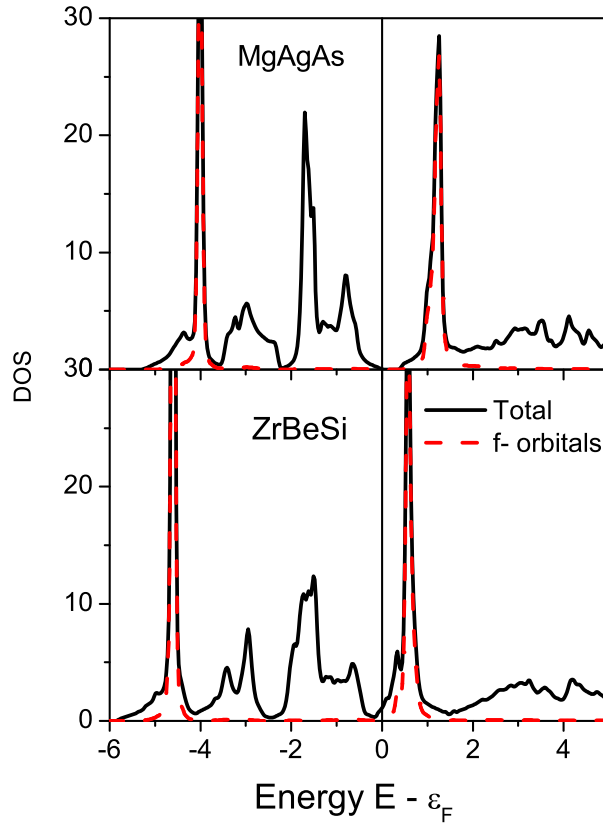


Figure 7.3: Density of states (DOS) of both GdNiSb compounds.

The states around the Fermi edge are mainly Ni  $3d$  states. For this calculations, only the LDA was used without applying a  $U_{eff}$ . Thus the Gd  $f$  orbitals are below and just above the Fermi edge as expected for a half filled  $4f$  orbital. As other calculations showed here, applying a  $U_{eff}$  would shift the  $f$  orbitals by  $\frac{U_{eff}}{2}$  away from the each other. On the other hand, it is known that applying a  $U_{eff}$  would lead to a wrong calculation of the electric field gradient.

### 7.3 Mössbauer measurements

Although a single phase sample could not be obtained,  $^{155}\text{Gd}$  - Mössbauer measurements were performed with the mixed sample. The  $^{155}\text{Gd}$  - Mössbauer spectra above 9 K (Figure 7.4), two lines can be found. The dominant single line ( $\approx 60\%$ ) can be assigned to the cubic phase, while the line with a broad quadrupole splitting corresponds to the hexagonal phase.

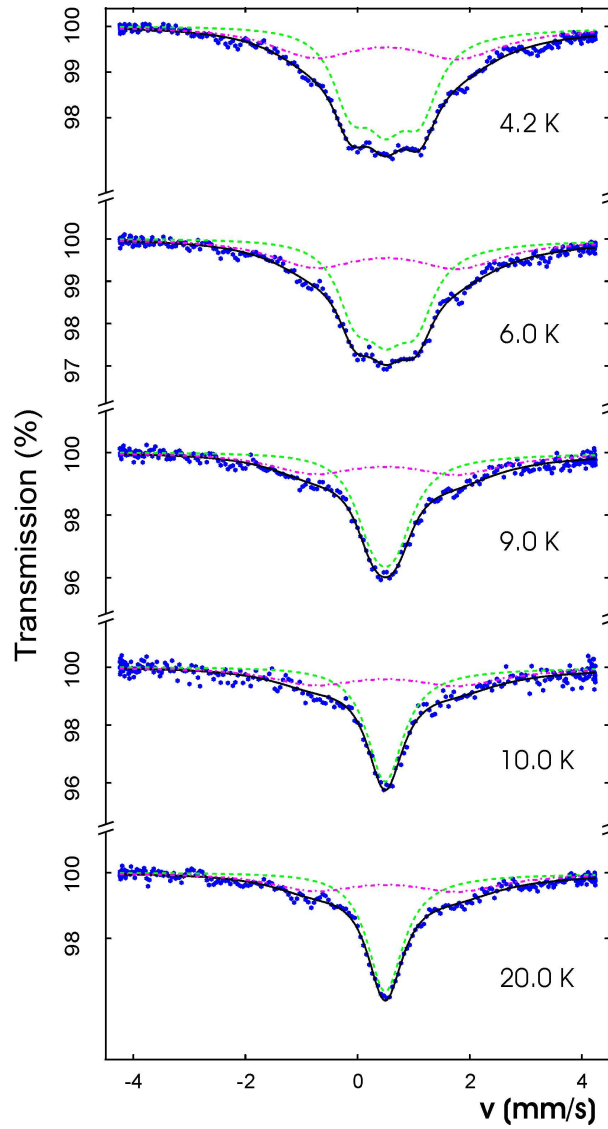


Figure 7.4:  $^{155}\text{Gd}$  - Mössbauer spectra of biphasic GdNiSb (cubic phase = dotted line, hexagonal phase = dot-dashed line).

For the cubic phase magnetic ordering below 9.5(5) K was observed. The value of the hyperfine fields for  $T \rightarrow 0$  suggest a antiferromagnetic ordering (Figure 7.5). The hexagonal phase shows magnetic ordering below 4.2 K.

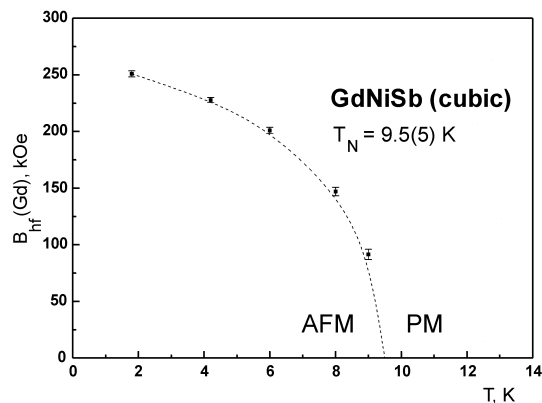


Figure 7.5: Trend of the magnetic hyperfine field  $B_{hf}$  in cubic GdNiSb.

## 7.4 Summary

Band structure calculations predict metallic behavior for hex. GdNiSb and semiconducting behavior for cubic GdNiSb. A monophasic compound could not be obtained with the preparation methods used here.  $^{155}\text{Gd}$  - Mössbauer measurements have been performed on the biphasic GdNiSb compound. In all spectra two subspectra have been identified and could be assigned to the respective structure. Measurements below 4.2 K to find the magnetic ordering temperature of the hexagonal phase as well as calculations to determine the electric field gradient are ongoing.



# 8 GdPdSb Compound

## 8.1 Introduction

The well-studied  $REPdSb$  series of compounds exhibits a variety of unusual properties, such as the Kondo effect, half metallic behavior, heavy fermion behavior with magnetic instability, etc. [4, 7, 37, 130]. A deeper understanding of the electronic structure of such complex compounds has become extremely important, both from a fundamental as well as materials science point of view. In the  $REPdSb$  series of compounds, both structure types can be found: the LiGaGe structure type for  $RE = La - Sm, Gd$  and  $Tb$ ; and the MgAgAs structure type for  $RE = Dy - Yb$  (figure 8.1).

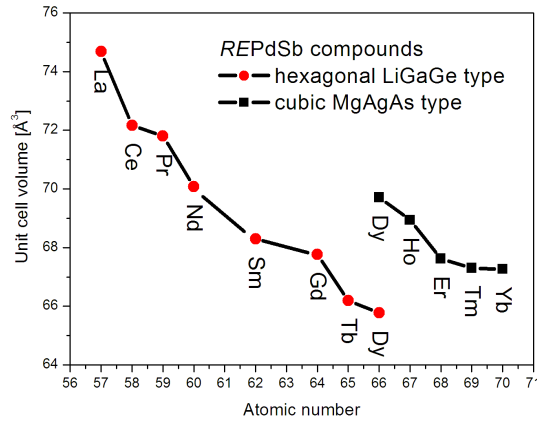


Figure 8.1: Dependence of structure and unit cell volume on the  $RE$  - atom for  $REPdSb$  compounds [37]

In this part, the focus is on the  $GdPdSb$  compound. A number of experimental studies have been carried out for this compound [37, 131, 100, 132], but it just was shown recently that  $GdPdSb$  does not crystallize in the  $CaIn_2$  structure type (random distribution of  $Pd$  and  $Sb$  atoms), but rather in an ordered “superstructure”, the LiGaGe structure type [133].

A number of experimental studies have been carried out on LiGaGe structure type compounds. For example, Baran et al. [134, 116, 135, 26] observed antiferromagnetic transitions at low temperatures for  $REYSn$  ( $RE = Gd - Er$ ,  $Y = Cu, Ag$  and  $Au$ ) ternary compounds.

## 8.2 Structural characterization

Our X-ray diffraction results (figure 8.2 show that our samples consisted of a single phase. A refinement of the powder pattern provided nearly the same R values for both the  $\text{CaIn}_2$  and the  $\text{LiGaGe}$  structures. For the  $\text{LiGaGe}$  structure ( $P6_3mc$ , figure 8.3), the following results were obtained: Gd occupies crystallographic  $2a$  sites  $(0, 0, 0)$ ; Pd atoms occupy the  $2b$  sites  $(\frac{1}{3}\frac{2}{3} 0.2923(6))$ ; and Sb atoms occupy the  $2b$  sites  $(\frac{1}{3}\frac{2}{3} 0.7022(3))$ . The lattice parameters are  $a = 4.553(5) \text{ \AA}$  and  $c = 7.434(8) \text{ \AA}$ . The structure and parameters are in good agreement with those published for single crystals of  $\text{GdPdSb}$  as  $\text{LiGaGe}$  structure type [133]. The experimental X-ray pattern was refined using the FULLPROF program [74].

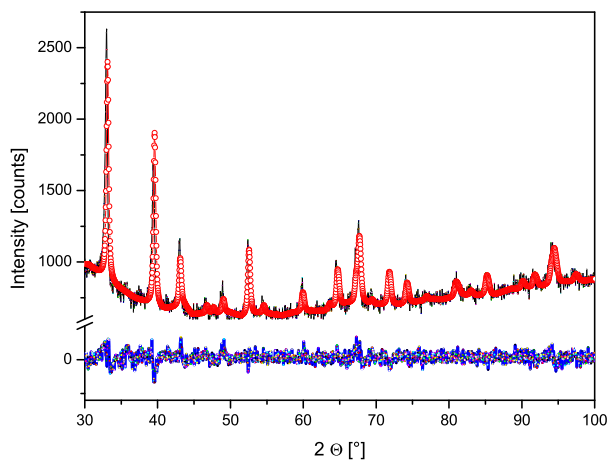


Figure 8.2: Powder x-ray diffraction pattern of  $\text{GdPdSb}$ . The difference plot is shown at the bottom of the figure.  $R_{\text{Bragg}}(\text{GdPdSb}) = 5.01$

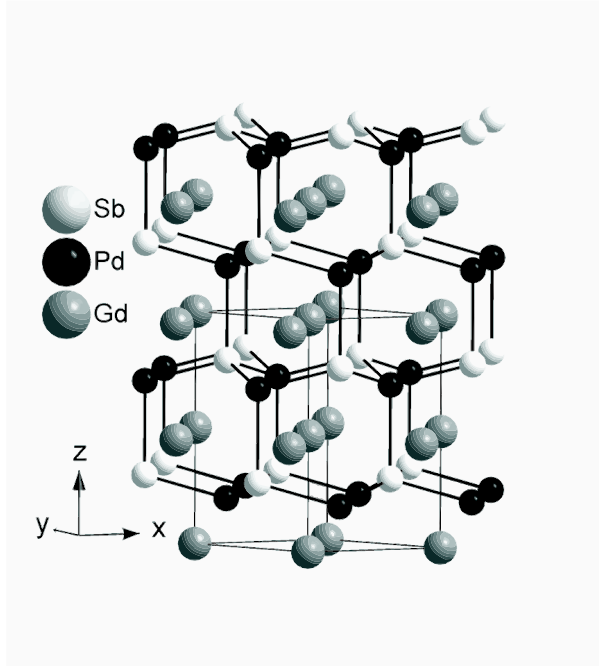


Figure 8.3: Crystal Structure of GdPdSb (LiGaGe - structure,  $P6_3mc$ )

### 8.3 Band structure calculations

Self-consistent band structure calculations were carried out using the full potential linear augmented plane wave (FLAPW) method [64]. The calculations were performed using the Perdew-Burke-Ernzerhof implementation of the generalized gradient approximation (GGA) [65]. We used 2.9, 2.55 and 2.55 Bohr for the muffin-tin radii (RMTs) of Gd, Pd and Sb atoms, respectively. The self-consistent calculations employed a grid of  $24 \times 24 \times 15$  k points (8640 total) within the primitive wedge of the Brillouin zone. Finally, the LDA+ $U$  self interaction correction (SIC) scheme was used to account for the orbital dependence of the Coulomb and exchange interactions. In this work, we used  $U = 6.7$  eV and  $J = 0.7$  eV for the Gd atom, values that have been confirmed by valence band – XPS measurements.

#### 8.3.1 Antiferromagnetic GdPdSb

The band structure of antiferromagnetic GdPdSb is displayed in figure 8.4. The antiferromagnetic structure was obtained by constructing a hypothetical supercell of GdPdSb by doubling the lattice parameters in all three directions. In this superstructure, the spins of Gd atoms lying in one plane are aligned parallel, and those from the nearest neighbor Gd atoms sitting in another plane are aligned antiparallel. Such an arrangement of spins of Gd atoms avoids a possible spin frustration state within the triangular network of Gd atoms. Such a layered structure was found for NdPdSb from neutron

diffraction measurements [24]. The descriptions of the DOS and the band structure for this compound were provided by using experimentally obtained crystal structures. Figures 8.4a & 8.4b show the band structures obtained from the GGA and the LDA+ $U$  calculations, respectively. In both cases, there are states appearing at the Fermi energy. Photoemission measurements indicate that the splitting of the  $f$  states within the LDA - GGA approximation is smaller than that obtained experimentally (the photoemission spectrum with the calculated DOS from the LDA +  $U$  is shown in figure 8.4c). Inclusion of the  $U$  in the calculations results in a larger splitting between the occupied and unoccupied Gd  $f$  states. The Gd  $f$  states are situated almost -8.4 eV below the Fermi energy. A broad band feature becomes visible in the photoemission spectrum between 6 and 11 eV below the Fermi energy. The origin of this feature is completely from Gd  $f$  states. In addition, another broad feature that is related to the Pd  $d$  and Sb  $p$  orbitals, and that has a width of approximately 4 eV, appears close to the Fermi energy. There are Sb  $p$  states mixed with Pd  $d$  states just below the Fermi energy that lead to strong bonding interactions between the Sb and Pd atoms. However, the states around the Fermi energy are not influenced by the Gd  $f$  states. Pd  $d$  states and Sb  $p$  states are unaffected by the electronic correlation.

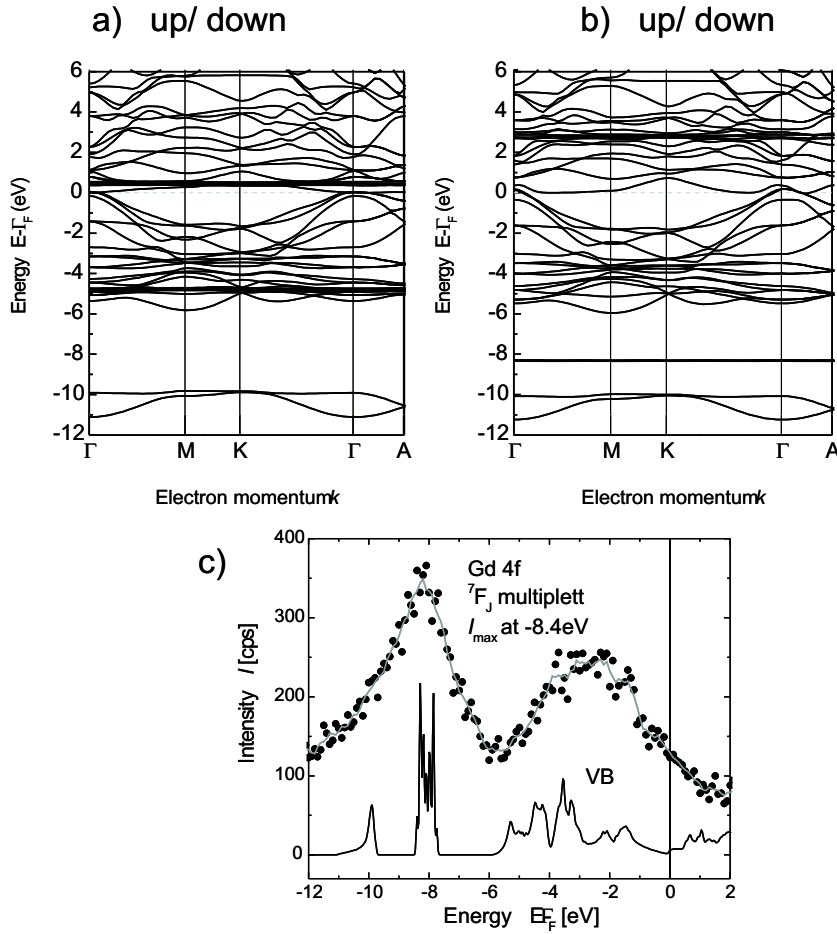


Figure 8.4: LAPW band structure of antiferromagnetic GdPdSb from the (a) GGA and the (b) LDA +  $U$  calculations. For comparison, the DOS calculated using the LDA +  $U$  with a photoemission spectrum from GdPdSb excited by Mg  $K_{\alpha}$  radiation is given in (c).

The calculated total energy for the antiferromagnetic structure of GdPdSb is with  $\Delta E = 5.9$  meV lower than the energy for the ferromagnetic structure. Thus the antiferromagnetic ground state is more stable than the ferromagnetic. Since the difference between energies is marginal, a competition between the two ground states can not be excluded. A similar type of such an energy based behavior was also observed by Felser *et al.* for the layered compound  $\text{LaSr}_2\text{Mn}_2\text{O}_7$  [136]. Therefore band structure calculations were performed for both ground states.

### 8.3.2 Ferromagnetic GdPdSb

Figure 8.5 shows the total density of states (DOS) of ferromagnetic GdPdSb obtained from spin polarization calculations using the GGA (figure 8.5a) and the LDA+ $U$  scheme (figure 8.5b). For all the plots, the upper section of each plot displays the majority (up)

spin states and the lower section displays the minority (down) spin states.

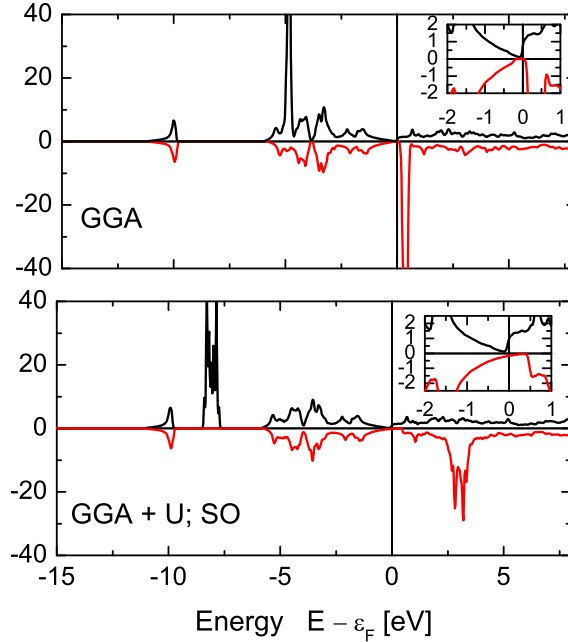


Figure 8.5: Projected density of states for ferromagnetic GdPdSb within the GGA a) and the LDA +  $U$  b). The insets enlarge the DOS around the Fermi energy. Spin up states are shown in the upper portion and spin down states in the lower portion of each plot. The top of the valence band is taken as zero on the energy axis.

For the GGA calculations, the half-filled Gd  $f$  orbitals form very narrow (well localized), strongly polarized bands. The Gd  $f$  states split with a separation of 5.1 eV between the up and down spin states. The empty Gd  $f$  spin down states are just above the Fermi energy with a separation 0.1 eV, while the completely filled Gd  $f$  spin up states are at approximately -5 eV below the Fermi energy. The inset enlarges the DOS around the Fermi energy. A minority band gap can be seen at the Fermi energy, while there are states for the majority band. Including the Coulomb parameter  $U$  in the calculations results in the Gd filled  $f$  states shifting approximately -8 eV below the Fermi energy and confirms our photoemission results. Differences in the two methods arise not only because of the larger splitting between the occupied and unoccupied Gd  $f$  states that is due to introduction of the Coulomb parameter. Now in both spin directions there are states at the Fermi energy. The majority spin states at the Fermi energy are weakly localized, while in the minority spin direction the states are itinerant. The spin-polarized calculations for GdPdSb yield a magnetic moment of 7.03  $\mu_B$ . The calculated local magnetic

moment of Pd and Sb is nearly zero.

## 8.4 Magnetic properties

Magnetic susceptibility measurements of GdPdSb (figure 8.6) show an antiferromagnetic transition at  $T_N = (13.1 \pm 0.3)$  K that is slightly lower than the reported 16.5 K [37].

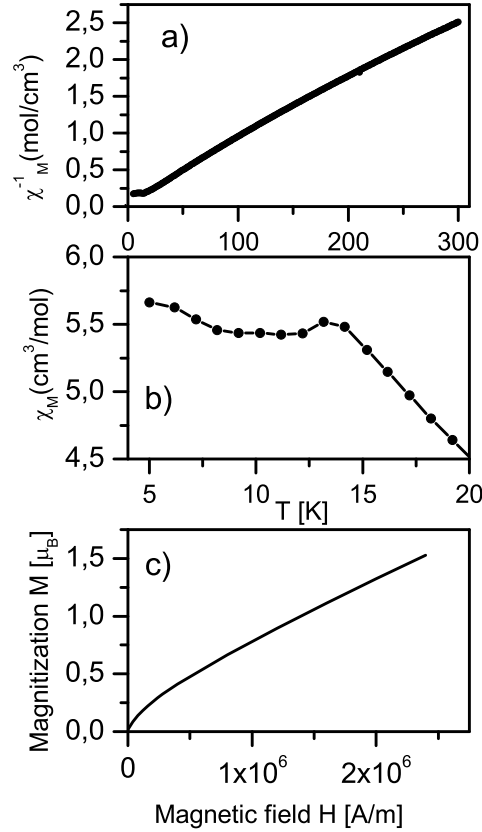


Figure 8.6: a) Magnetization curve in high magnetic fields at 4 K; b) inverse magnetic susceptibility of GdPdSb ( $T_N = 13.1$  K); c) susceptibility below 17 K as a function of temperature in an applied field of  $80 \times 10^3$  A/m

Between 30 and 300 K, the susceptibility follows the Curie-Weiss law. The values of the paramagnetic Curie temperature  $\theta_p$  and effective paramagnetic moment  $\mu_{eff}$  were obtained from a Curie-Weiss fit to the experimental data. The paramagnetic Curie temperature  $\theta_p = -(16 \pm 1)$  K is negative, indicating an antiferromagnetic coupling between the rare earth atoms. The effective paramagnetic moment of  $\mu_{eff} = (7.81 \pm 0.05) \mu_B$  for Gd is near the free  $\text{Gd}^{3+}$  ion value of  $\mu_{eff}(\text{theo}) = gJ[J(J+1)]^{\frac{1}{2}} = 7.94 \mu_B$ . As shown in figure 8.6b, the susceptibility in an applied field of  $80 \times 10^3$  A/m

increases below  $T_N$  (at  $\approx 8$  K). The value of the magnetic moment on the Gd ion at 4 K and  $2.3 \times 10^6$  A/m is  $(1.52 \pm 0.02) \mu_B$  (extrapolated to  $(1.75 \pm 0.02) \mu_B$  at 0 K), i.e. much smaller than the theoretical expected value of  $7 \mu_B$  for ferromagnetic GdPdSb (see above) and does not attain saturation (figure 8.6a). Magnetization curves at different temperatures slightly above and below  $T_N$  show small, narrow hysteresis loops below  $T_C = (8.0 \pm 0.3)$ K that could possibly be caused by ferromagnetic ordering (figure 8.7). This type of ferromagnetic behavior in a compound with a small magnetic moment was also seen by Augsburg et al. in the double perovskite  $\text{Ca}_2\text{CoTeO}_6$  at low temperatures. In fact,  $\text{Ca}_2\text{CoTeO}_6$  displayed characteristic antiferromagnetic ordering behavior below 10 K [137]. For the NdPdSb compound, a ferromagnetic ordering after an antiferromagnetic transition was found as well, but with a positive paramagnetic Curie temperature [24]. The second transition of GdPdSb at  $T_C = (8.0 \pm 0.3)$  K is too low to be due to possible impurities, e.g. Gd metal.

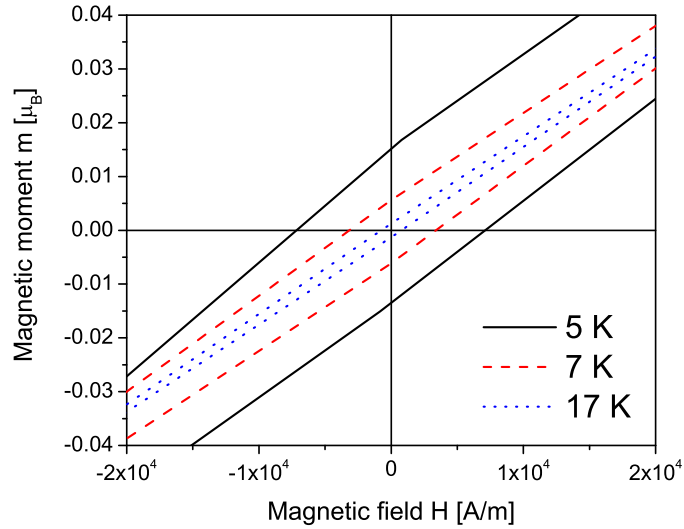


Figure 8.7: Sections of hysteresis loops of GdPdSb for different temperatures.

The  $\text{Gd}^{3+} - \text{Gd}^{3+}$  distances are large, indicating that the magnetic interactions have an indirect character that could be described by the RKKY model interaction [31]. In that model, the paramagnetic Curie or ordering temperatures are proportional to the de Gennes factor  $G = (g_j - 1)^2 J(J + 1)$  [138]. Zygmundt and Sztula showed that the dependence of  $\theta_p$  and  $T_N$  on the *RE* element within the *RE*PdSb series does not satisfy this de Gennes scaling. Thus the simple RKKY model is not suitable for describing the magnetic properties of GdPdSb [132].

## 8.5 Conductivity measurements

The resistivity is  $(2.3 \pm 0.2)$  m $\Omega$ cm at 280 K and  $(1.7 \pm 0.2)$  m $\Omega$ cm at 4 K, agreeing well with the results in [15]. GdPdSb shows metallic behavior below 280 K. According

to the LDA +  $U$  band structure calculations, GdPdSb should be metallic at 0 K. The low temperature dependence of GdPdSb (figure 8.8) shows two features at  $(13 \pm 0.5)$  K and  $(8 \pm 0.5)$  K that correspond to magnetic transitions, thus confirming the existence of a second magnetic transition below the antiferromagnetic ordering temperature. The value of the resistivity is very high; in fact, in the entire series of  $REPdSb$  compounds ( $RE = Pr - Tm$ ), a high value, whose origin is not yet understood at present, is observed for each compound [15].

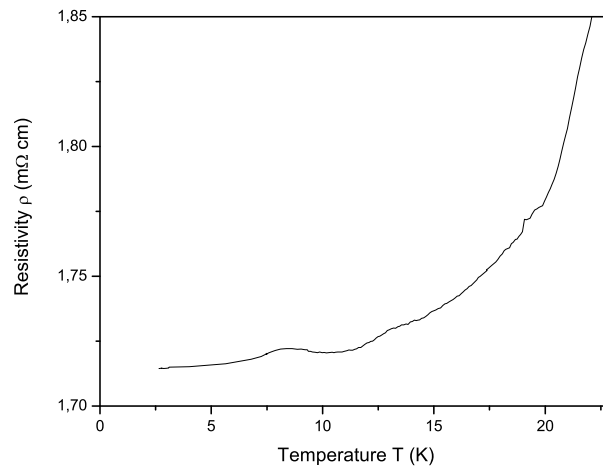


Figure 8.8: Conductivity measurements of GdPdSb at low temperatures.

## 8.6 Mössbauer measurements

Due to the strong neutron absorption of Gd, neutron diffraction to investigate the magnetic structure is not possible. Thus  $^{155}\text{Gd}$  Mössbauer spectroscopy was used to examine the magnetic structure of this compound. The spectra are shown in figure 8.9.

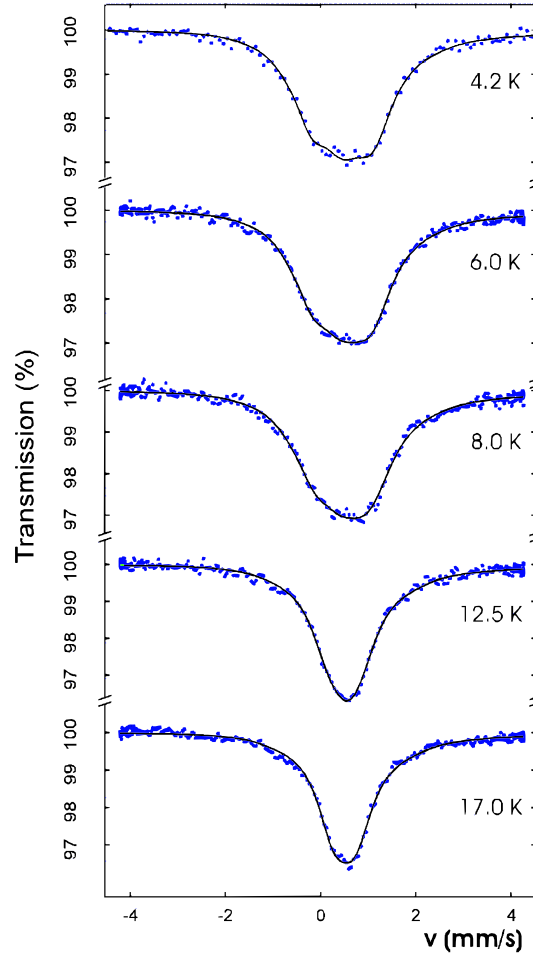


Figure 8.9:  $^{155}\text{Gd}$  Mössbauer spectra of GdPdSb at different temperatures

The magnetic splitting below the antiferromagnetic ordering temperature  $T_N = (13.1 \pm 0.3)$  K can be observed in these spectra. Below 10 K an angle  $\beta = 32(4)^\circ$  arises between the main axis of the electric field gradient ( $V_{ZZ}$  parallel to the  $c$ -axis) and the magnetic hyperfine field (figure 8.10). This could be due to a canting of the Gd-moments about this angle relative to the  $c$ -axis. The corresponding temperature fits well with the SQUID data.

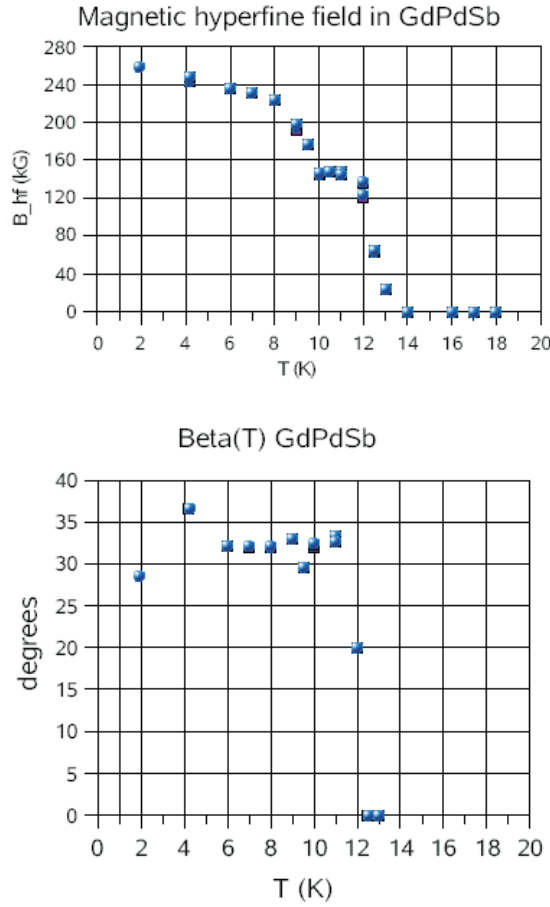


Figure 8.10: Temperature dependence of the magnetic hyperfinefield (top) and angle between hyperfinefield and field gradient (bottom)

## 8.7 Summary and conclusion

The ternary rare earth compound GdPdSb has been synthesized as a single phase compound. It crystallizes in the ordered LiGaGe structure and undergoes magnetic transitions at  $T_N = (13.1 \pm 0.3)$  K and  $T_C = (8.0 \pm 0.3)$  K. The first transition was identified as a transition to an antiferromagnetic ground state. This is in accordance with band structure calculations. Also, the paramagnetic Curie temperature  $\theta_p = -16$  K indicates an antiferromagnetic coupling between the rare earth atoms. However, electronic structure calculations show only a marginal energy difference between ferromagnetic and antiferromagnetic ground states. For this reason, the existence of a metastable ferromagnetic ordering can be expected. Indeed, magnetic measurements show a second magnetic transition. The rise of the susceptibility below  $T_C = (8.0 \pm 0.3)$  K and the observation of a hysteresis indicate a ferromagnetic state. Conductivity measurements confirm both the

metallic behavior of the compound and a second transition at  $T_C = (8.0 \pm 0.5)$  K that also corresponds to the magnetic measurements. Below the second magnetic ordering temperature, the magnetization does not attain saturation in fields up to  $2.3 \times 10^6$  A/m. For ferromagnetic GdPdSb, a magnetic moment of  $7.03 \mu_B$  is expected from band structure calculations. An estimation of the magnetic field needed to experimentally attain this value leads to a field of  $8.6 \times 10^6$  A/m. A similar type of ferromagnetic ordering is found within the series of *RE*PdSb compounds for NdPdSb [24]. For NdPdSb, a square-modulated structure is observed below the second magnetic ordering temperature. Thus either a square-modulated structure or a canted ferromagnetic ordering for GdPdSb can be proposed. Due to the results of the  $^{155}\text{Gd}$  Mössbauer measurements, the canted ferromagnetic ordering is likely the existing order. Band structure calculations predict a pseudogap at the Fermi energy in the antiferromagnetic ground state, even if Coulomb and exchange interactions are taken into account to compensate for the too low splitting of the *f* states. For the ferromagnetic case, band structure calculations predict itinerant states in the minority band and weak localized states in the majority band. According to the classification scheme for half metals as proposed by Coey et al. [62], GdPdSb belongs to the class of Type III half metal. This is the first half metallic ferromagnet with a LiGaGe structure. However, the transition temperature of GdPdSb is too low for it to be used in spintronic applications.

# 9 *REAuSn* Compounds

## 9.1 Introduction

In this chapter the focus is on the properties of *REAuSn*. In accordance with the previously mentioned notation, *REAuSn* can be described as  $[RE]^{3+}$  within a  $[AuSn]^{3-}$  sublattice. Several studies on these compounds are known [26, 73, 116]. However the interpretation in the cited publications was only supported by powder x-ray diffraction, which could not provide the precise structural parameters necessary for band structure analysis. A change of the valence electron concentration should strongly affect the properties of *REME* compounds with LiGaGe structure. This was shown within the class of half-Heusler compounds [21, 22, 20]. Half Heusler phases *XYZ* can be described as  $[X]^{n+}$  ions within a zincblende  $[YZ]^{n-}$  sublattice. Half heusler compounds with 22 electrons (e.g. with  $Mn^{3+}$  at the *X* position) should be localized moment ferromagnets. The 22 electrons divide themselves into 13 in the majority spin and 9 in the minority spin direction, resulting in a semiconducting gap (half metallic behavior) in the majority spin direction.

Based on the fact that MnAuSn is a 22 electron half-Heusler compound, one can expect that doping with Mn at the Gd – position should modify the electronic properties of GdAuSn. However, the GdAuSn/ MnAuSn system does not form a homogenous solution, but instead a granular system [139]. It is known that properties of hybrid materials can be essentially different from those of the pure single phases [140, 141]. Several groups have recently shown that certain granular ferromagnets exhibit giant magnetoresistances [53]. Such granular ferromagnets are produced by cosputtering or comelting two materials that are immiscible, one of which is ferromagnetic. With this in mind we explored the properties of granular materials based on mixtures of GdAuSn and MnAuSn. In the *REAuSn* series of compounds, both structure types can be found: the LiGaGe structure type for  $RE = La - Sm, Gd - Er$ ) and the  $C1_b$  structure type for  $RE = Er, Tm, Lu$ . According to band structure calculations, *REAuSn* compounds having the half-Heusler structure should be semiconducting whereas compounds with the LiGaGe structure should be metallic. Similar to other semiconducting ternary rare earth compounds, some of the *REAuSn* compounds show a giant magnetoresistance effect

## 9.2 Structural characterization

The crystal structures of *REAuSn* and MnAuSn were determined using powder x - ray diffraction in the reflection mode. The corresponding x -ray patterns (Figure 9.1) reveal that the sample MnAuSn adopts the half-Heusler structure (MgAgAs - structure,  $F\bar{4}3m$ ) with  $a = 6.333(7)$  Å, Mn at  $4b (\frac{1}{2}\frac{1}{2}\frac{1}{2})$ , Au at  $4c (\frac{1}{4}\frac{1}{4}\frac{1}{4})$  and Sn at  $4a (0\ 0\ 0)$ . The lattice parameters are in good agreement with those published in [142]. Small amounts of an unidentified impurity phase were found (estimated to be  $\approx 3\%$ ).

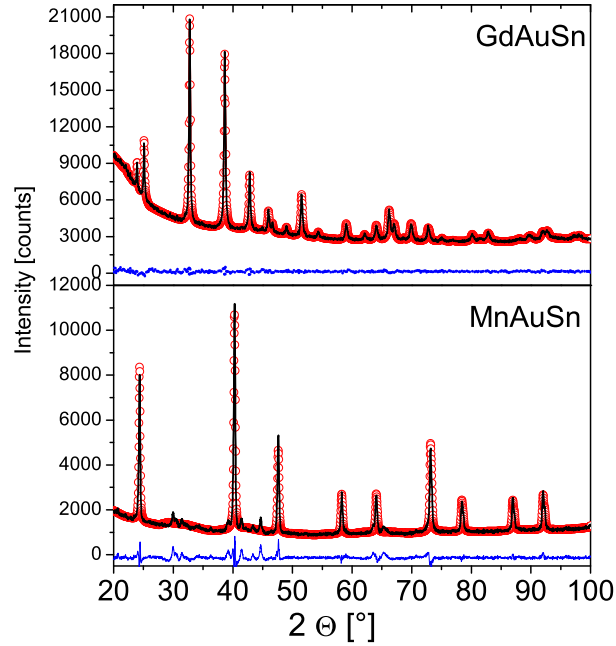


Figure 9.1: Powder x-ray diffraction patterns of GdAuSn (top) and MnAuSn (bottom) together with Rietveld refinement curves (red circles). The difference plot is shown at the bottom of the figures.  $R_{Bragg}$  (GdAuSn) = 2.02,  $R_{Bragg}$  (MnAuSn) = 4.67.

The *RE*AuSn (*RE* = Tm, Er) compounds also crystallize in the MgAgAs structure type. The lattice parameters are summarized in Table 9.1. Due to the lanthanoid contraction, the lattice parameter of TmAuSn is smaller than of ErAuSn. ErAuSn not only crystallize in the MgAgAs structure type but also in the LiGaGe structure type [143]. For the latter one metallic behavior (see Figure 9.9) and no magnetoresistance effect is found.

Table 9.1: Lattice parameter of *RE*AuSn and MnAuSn compounds

Compound	$a$ (Å)	$c$ (Å)	$V$ (nm <sup>2</sup> )	Reference
GdAuSn	4.660(8)	7.430(1)	0.1141	[144]
TmAuSn	6.599(8)		0.2875	[144]
ErAuSn	6.605(7)		0.2882	[144]
MnAuSn	6.333(7)		0.2541	[142]

For GdAuSn the fit of the powder x-ray diffraction pattern provides nearly the same  $R$  values for both the CaIn<sub>2</sub> and the LiGaGe structures. The refinement for LiGaGe (P6<sub>3</sub>mc) leads to  $a = 4.660(8)$  Å and  $c = 7.430(1)$  Å, with atom positions as described

below. Single crystal x-ray diffraction confirms the LiGaGe structure of GdAuSn.

Table 9.2: Crystal data and structure refinement for GdAuSn.

Empirical formula	GdAuSn
Formula weight	472,93 g/mol
Unit cell dimension	a = 0.4662 nm
	c = 0.7434 nm
	V = 0.1399(2) nm <sup>3</sup>
Pearson symbol	hP6
Structure type	LiGaGe
Space group	$P\bar{6}_3mc$
Formula units per cell	Z = 2
Calculated density	11.224 g/cm <sup>3</sup>
Crystal size	0.3 × 0.3 × 0.3 mm <sup>3</sup>
Transmission ratio	0.015596
Absorption coefficient	84.202 mm <sup>-1</sup>
F (000)	386
Device	Bruker Smart CCD
$\theta$ Range for data collection	5.05° to 27.96°
Range in $hkl$	±6, ±6, ±9
Total no. of reflections	2169
Independent reflections	158 ( $R_{int} = 0.0592$ )
Reflections with $I > 2\sigma(I)$	149
Data/ parameters	158/ 10
Goodness-of-fit on $F^2$	1.333
Final R indices [ $I > 2\sigma(I)$ ]	$R1 = 0.0723$ , $wR2 = 0.1816$
R Indices (all data)	$R1 = 0.0743$ , $wR2 = 0.1844$
Largest diff. peak and hole	4.524 and -7.894 e/Å <sup>-3</sup>

The structure was refined using SHELXL-97 [145]. Results of the refinement can be found in Table 9.2. The lattice parameters are in good agreement with those published [144]. In GdAuSn the Au<sub>3</sub>Sn<sub>3</sub> hexagons are puckered. The Au - Sn distance within the layer is 277.9(3) pm, whereas the interlayer distance is 302.4(7) pm. The rather small difference between the inter- and intralayer distances of Au - Sn shows that this compound has a three dimensional character. In MnAuSn the Au - Sn distances within the Au<sub>3</sub>Sn<sub>3</sub> hexagons are 274.2 pm. In hexagonal GdAuSn, the Au<sub>3</sub>Sn<sub>3</sub> hexagons have an ABAB layered structure, whereas the structure of MnAuSn can be described as an ABCABC sequence (Figure 9.2).

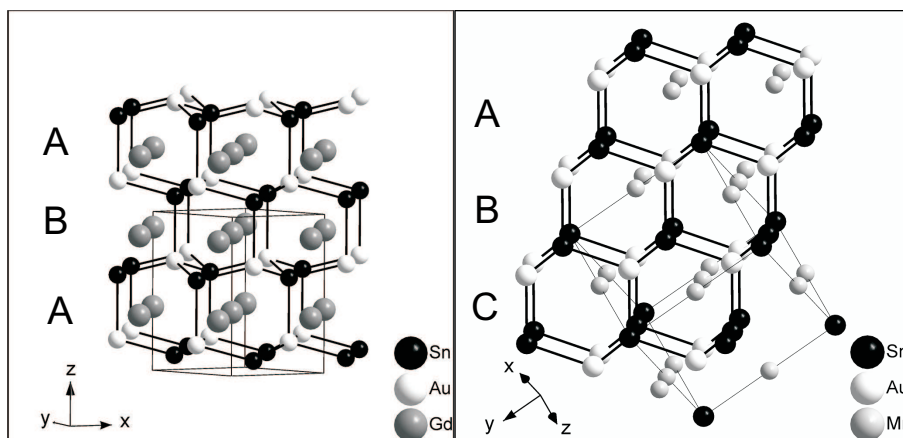


Figure 9.2: Structure of hexagonal GdAuSn and cubic MnAuSn. The layered ABC and ABAB structure is emphasized

### 9.3 Band structure and density of states

Spin-polarized band structure calculations of MnAuSn reveal a gap in one spin direction (majority states) and the metallic behavior in the minority state (Figure 9.3). It has a small gap because the electronegativity difference between the Au and Sn is small and according to Zintl rule it can be written as  $[\text{Mn}]^{3+}[\text{AuSn}]^{3-}$  [20].

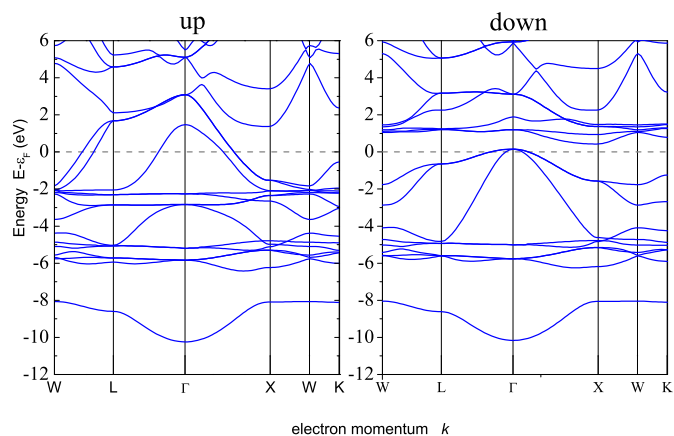


Figure 9.3: LDA band structure of MnAuSn; the top of the valence band is taken as zero on the energy axis.

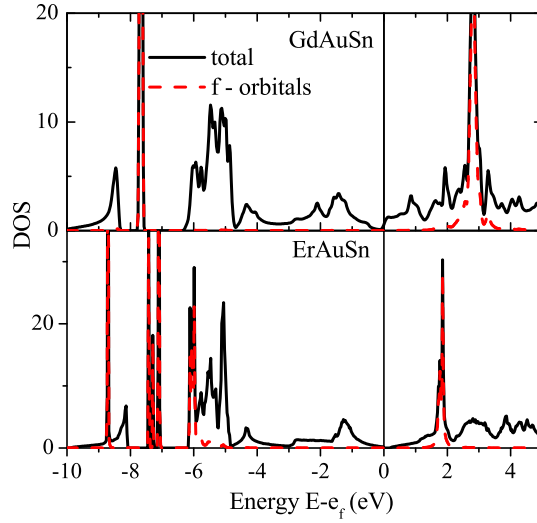


Figure 9.4: Density of states (DOS) for GdAuSn (top) and ErAuSn (bottom).

It follows from the band structure calculations that the magnetic moments in MnAuSn are associated with the Mn atoms. The local magnetic moments in *RE*AuSn are localized on the *RE* atoms only. On the other hand, the calculations predict the hyperfine magnetic field on all elements comprising the compounds. In accordance with the structure, the electrical field gradient should be zero on all elements of cubic compounds MnAuSn, ErAuSn and TmAuSn, and nonzero in hexagonal GdAuSn. The density of states (DOS) of the hexagonal GdAuSn and the cubic ErAuSn is displayed in Figure 9.4. GdAuSn can also be written as  $[\text{Gd}]^{3+}[\text{AuSn}]^{3-}$ . It has a pseudo gap arising at the Fermi energy, whilst ErAuSn has a gap at the Fermi edge. Thus one can expect metallic behavior for GdAuSn and semiconducting behavior for ErAuSn. TmAuSn (not shown here) also has a gap at the Fermi edge.

For GdAuSn all three possible “simple” antiferromagnetic ordering structures were calculated (see chapter 3). The results are summarized in Table 9.3.

Table 9.3: Calculated energy and magnetic parameters for the three simple antiferromagnetic ordering structures of GdAuSn

Structure	156			026			031		
	Gd	Au	Sn	Gd	Au	Sn	Gd	Au	Sn
$\mu_{eff}(\mu_B)$	7.07	0	0	7.097	0	0	7.079	0	0
$H_{hf}$ (kOe)	392.29	34.73	16.88	404.03	15.90	25.12	391.90	49.91	45.03
$V_{zz}$ ( $10^{21}$ V/m <sup>2</sup> )	-0.72	7.45	8.6	-1.98	7.4	9.11	-1.88	7.10	8.90
Tot. Energy (Ry)	-292061.2437			-292061.2152			-292061.2128		

Comparing the total energies of the three, an antiferromagnetic ordering of the gadolinium moments perpendicular to the *c* axis should be more stable.

## 9.4 Magnetic measurements

### 9.4.1 REAuSn ( $RE = \text{Gd, Er, Tm}$ )

The magnetic susceptibility measurements of the GdAuSn and ErAuSn (Figure 9.5) show an antiferromagnetic transition at  $T_N = 26$  K and  $T_N = 4$  K, which is in good agreement with earlier published data [116, 117, 146]. TmAuSn shows no magnetic transition in the measured temperature range [147]. Above 40 K the magnetic susceptibilities obey the Curie-Weiss law with a paramagnetic Curie temperatures of  $\theta_P \approx -70$  K,  $\theta_P \approx -1.5$  K,  $\theta_P \approx -7$  K for GdAuSn, ErAuSn and TmAuSn, respectively. The effective magnetic moments  $\mu_{eff} = 8.04 \mu_B$ ,  $\mu_{eff} = 9.5 \mu_B$ ,  $\mu_{eff} = 7.7 \mu_B$  are close to the free  $RE^{3+}$  ion value of  $7.94 \mu_B$  ( $\text{Gd}^{3+}$ ),  $9.59 \mu_B$  ( $\text{Er}^{3+}$ ) and  $7.57 \mu_B$  ( $\text{Tm}^{3+}$ ).

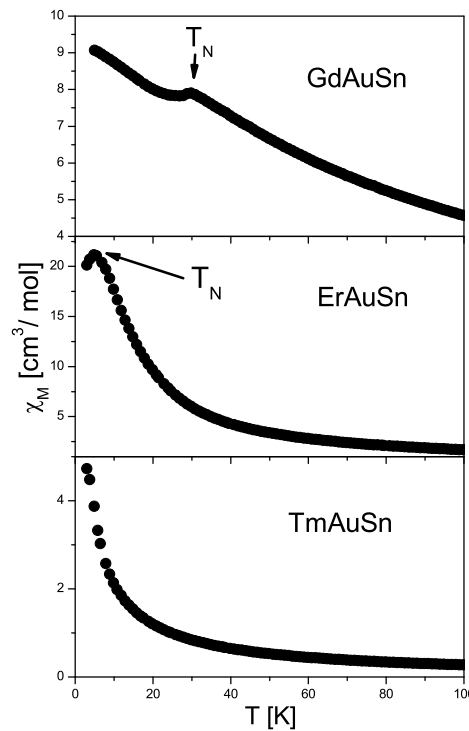


Figure 9.5:  $\chi_M$  vs.  $T$  of GdAuSn ( $T_N = 26$  K), ErAuSn ( $T_N = 4$  K) and TmAuSn.

### 9.4.2 MnAuSn

The half-Heusler compound MnAuSn reveals a ferromagnetic ordering at  $T_C = 570$  K (figure 9.6), which is below the upper stability temperature of 740 K [142]. The magnetisation curve with a narrow hysteresis loop proves that MnAuSn belongs to the class of soft ferromagnetic materials. The saturation magnetic moment of the compound is  $3.8 \mu_B/\text{f.u.}$ , which is in fair agreement with the theoretical value of  $3.99 \mu_B/\text{f.u.}$

that is derived from band structure calculations. Magnetisation measurements down to 5 K show the smooth increase of magnetisation to 10% greater than the value at room temperature.

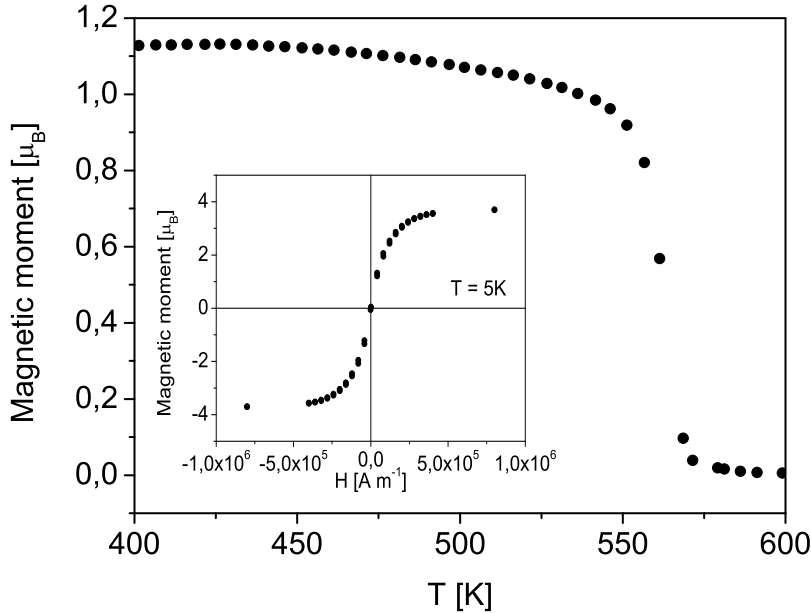


Figure 9.6: Temperature dependence of the magnetisation of MnAuSn in an applied field of 8000 A/m;  $T_C = 570\text{K}$ . Insert shows the hysteresis loop at 5K.

Table 9.4: The set of hyperfine parameters and effective moments obtained from band structure calculations of MnAuSn.

Parameters	MnAuSn		
	Mn	Au	Sn
$\mu_{eff}$ ( $\mu_B$ )	4.05	0.02	-0.08
$H_{hf}$ (kOe)	-61.67	-405.0	313.4
$V_{ZZ}$ ( $\text{V}/\text{m}^2$ )	0	0	0

## 9.5 Mössbauer measurements and magnetism of GdAuSn

$^{155}\text{Gd}$  and  $^{197}\text{Au}$  Mössbauer spectra of GdAuSn measured at  $T = 12\text{ K}$  are shown in Figure 9.7. The 77.34 keV  $^{197}\text{Au}$  broad resonance line has the isomer shift at  $\delta = 2.92(1)\text{ mms}^{-1}$ . The broadening could be due either to the effect of hyperfine magnetic or quadrupole interactions, or to their combination. The calculations show that, in the absence of a hyperfine field on the Au nuclei, the electrical field gradient  $V_{zz} = 9.2(9) \times$

$10^{21}$  V/m<sup>2</sup>. If both interactions are present, the corresponding hyperfine parameters are  $H_{hf}$  (Au) = 117(2) kOe and  $V_{zz}$  (Au) =  $6(3) \times 10^{21}$  V/m<sup>2</sup>. Comparison with theoretical values (table 9.3) shows that the presence of a hyperfine field agrees well with a former set of hyperfine parameters, i.e. there is a hyperfine magnetic field on Au atoms.

The <sup>155</sup>Gd spectrum with parameters  $\delta = 2.92(1)$  mms<sup>-1</sup> and  $H_{hf} = 198(5)$  kOe reveals the unique Gd site in the crystal structure. This finding confirms the magnetic and structural homogeneity of the sample under study and is in contrast to the results in publication [73], where the magnetic non homogeneity of GdAuSn was observed. The extremely small magnitude of the excited state quadrupole moment does not allow the value of the electrical field gradient on Gd atoms to be measured.

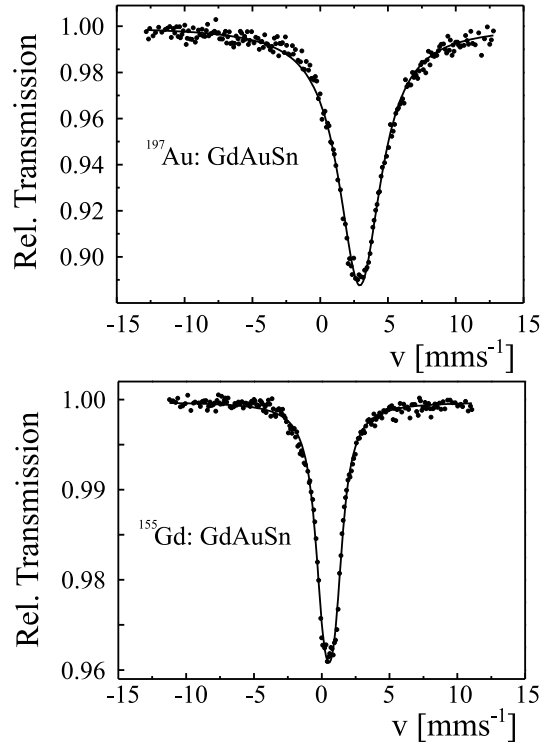


Figure 9.7: <sup>197</sup>Au and <sup>155</sup>Gd Mössbauer spectra of GdAuSn at T = 12 K

The <sup>119m</sup>Sn Mössbauer spectra measured across the antiferromagnetic ordering region are shown in Figure 9.8. The spectrum at T = 35 K corresponds to the only paramagnetic state and, within 2% accuracy, shows no traces of impurities in GdAuSn samples. The value of the isomer shift is  $\delta = 1.96(1)$  mms<sup>-1</sup> and the quadrupole splitting value is  $\Delta E_Q = 0.62(2)$  mms<sup>-1</sup>. The magnetically split Mössbauer spectrum in the antiferromagnetic state at T = 9 K has the following parameters:  $\delta = 1.90(1)$  mms<sup>-1</sup>,  $\Delta E_Q = -0.66(2)$  mms<sup>-1</sup> and  $H_{hf} = 26.8(1)$  kOe. Calculations of the quadrupole splitting using the theoretical value of  $V_{zz}$  (table 9.4) for Sn atoms lead to values between  $-0.747$  mms<sup>-1</sup> and  $-0.598$  mms<sup>-1</sup>, depending on the values of the quadrupole constant  $Q = -0.08$  barn

[148] or  $Q = -0.064$  barn [149]. The experimentally found value is in good agreement with this result. On the other hand, a discrepancy between the theoretical and experimental values of hyperfine magnetic fields on Sn and Gd atoms should be noticed. The effective hyperfine magnetic field,  $H_{eff}$  at Mössbauer nuclei of a paramagnetic nonconducting sample in zero external magnetic field consists of several contributions:

$$H_{eff} = H_C + H_L + H_D, \quad (9.1)$$

The Fermi contact term  $H_C$  arises from the imbalance of spin density of core electrons polarized by unpaired  $d$  - electrons,  $H_L$  is the orbital term, and the term  $H_D$  arises from the dipolar interaction of the nucleus with the spin moment of the atom. In the case of magnetic metals, additional factors such as the Lorentz and demagnetising field, direct conduction-electron polarization as well as indirect core-polarisation effects may be important [148]. Normally, the Fermi contact term dominates in the expression describing the hyperfine field on the Mössbauer nucleus. Watson and Freeman have noticed that even a small difference in the effects of fields of opposite sign created by action of magnetically polarized  $s$ -electron pairs of internal shells accounts for fields of hundreds of kilo-Oersteds [150]. Concluding, it appears that  $H_{eff}$  is very sensitive to the parameters of the calculation model, especially to the chosen radius of the  $3d$  shell. It follows from the above that the calculation of the magnetic field at nuclei is a very difficult task, and a discrepancy between the theoretical and experimental values of hyperfine fields on Gd and Sn should be classified as a common problem, which has no general solution so far.

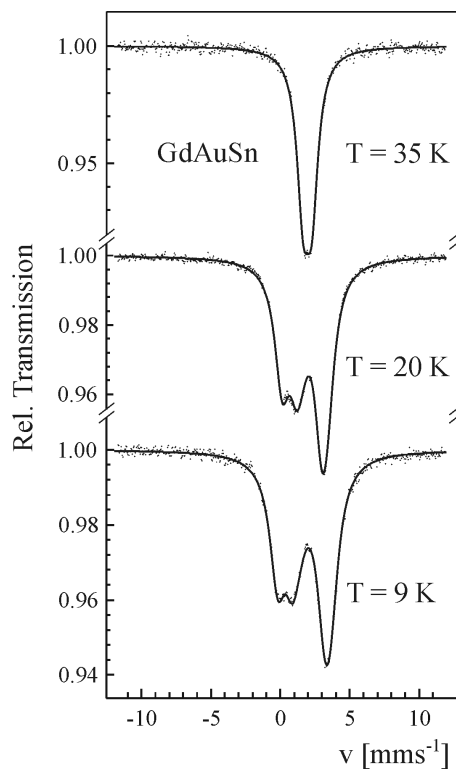


Figure 9.8:  $^{119}\text{Sn}$  Mössbauer spectra of GdAuSn across the antiferromagnetic transition.

The results of  $^{119m}\text{Sn}$  Mössbauer spectroscopy and the calculations allow the features of antiferromagnetic ordering in GdAuSn to be understood. The magnetic hyperfine fields induced by gadolinium atoms from planes above and below the Sn position do not cancel each other due to the non centric position of the atom. Comparing the experimental results with the theoretical results from Table 9.3, the best agreement is with the antiferromagnetic ordering of the gadolinium moments perpendicular to the  $c$  axis. This is also the ordering structure with the lowest total energy.

## 9.6 Resistivity and magnetoresistance measurements

The resistivity measurement results for GdAuSn, TmAuSn, ErAuSn and MnAuSn are presented in Figure 9.9. Hexagonal ErAuSn, GdAuSn and MnAuSn reveal a metallic behavior up to 285 K, while TmAuSn and cubic ErAuSn show semiconducting behavior with a metal - insulator transition at  $\approx 25$  K. This finding confirms the results of band structure calculations.

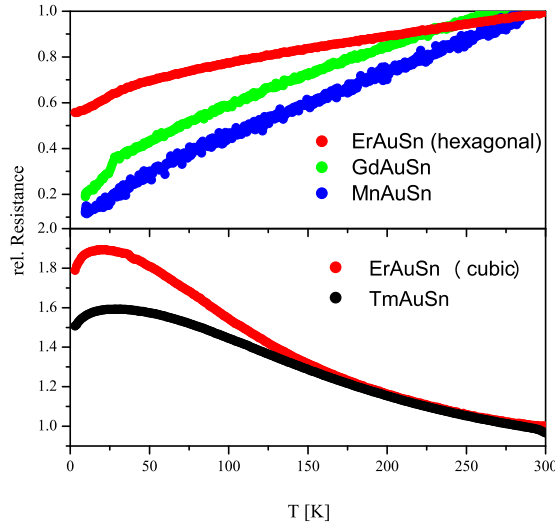


Figure 9.9: Zero magnetic field conductivity measurements of MnAuSn, TmAuSn and GdAuSn.

For the semiconducting compounds, the resistivity  $\rho_a$  follows the activation law in the temperature range 200 - 300K:

$$\rho_a = \rho_0 \exp(E_a/k_B T), \quad (9.2)$$

where  $E_a \approx 7$  meV and  $E_a \approx 8$  meV for TmAuSn and ErAuSn, respectively. For temperatures lower than 100 K a metallic-like behavior is observed. Such a behavior is typical for conduction through an impurity band that overlaps the conduction band. The resistivity  $\rho_m$  can be approximated by:

$$\rho_m = \rho_0 + CT^\alpha, \quad (9.3)$$

with  $\alpha \approx 0.3$  for TmAuSn and  $\approx 0.35$  for ErAuSn. Thus the complete temperature dependence can be described by the conduction of parallel channels, one corresponding to the metallic conduction and the other to the thermal activation. The temperature dependence of the MR is weak above 150 K, but increases at lower temperatures. The resistance slope shows a metal - insulator (MI) transition. GdAuSn shows an decrease in resistivity below  $T_N$ .

### Magnetoresistance of TmAuSn and ErAuSn

The resistivity for the metallic compounds MnAuSn and GdAuSn does not essentially change in magnetic fields up to  $1.6 \times 10^6$  A/m. Non-magnetic rare earth compounds have a low positive magnetoresistance. This weak MR may arise from the additional scattering of the charge carriers due to the Lorentz force (see e.g. [151]). Figure 9.10 shows the electrical resistance and magnetoresistance of ErAuSn and TmAuSn compounds. Above the metal - insulator transition these compounds show nearly no magnetoresistance

(MR). At the transition a small negative MR is observed, while below this transition in every compound the magnitude of the MR is considerable higher.

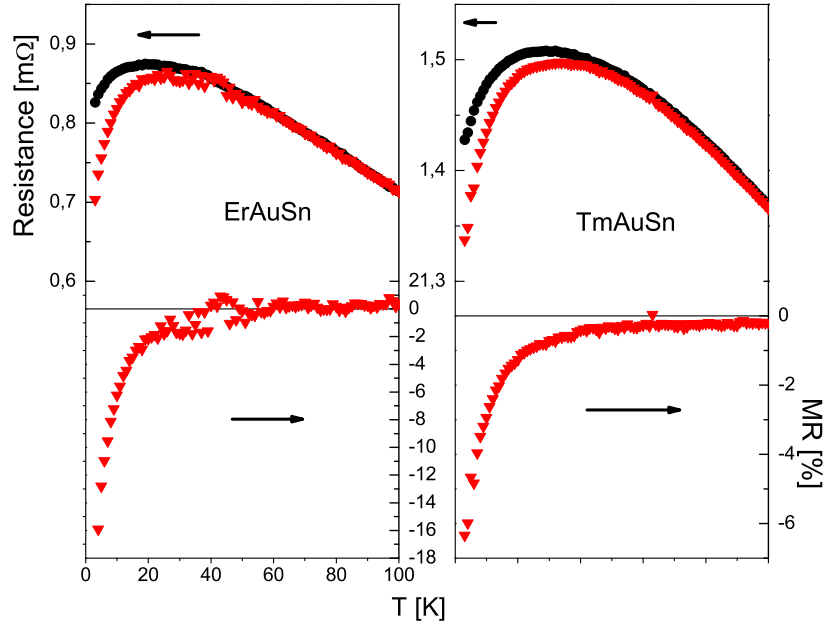


Figure 9.10: Electrical resistance of *REAuSn* compounds without and with an externally applied field of  $1.6 \times 10^6$  A/m . Below each plot the respective magnetoresistance (MR).

For similar rare earth containing semiconductors with a magnetic transition, a negative MR is found that, for low MR values in the paramagnetic state [101], is proportional to the square of the magnetization of the  $4f$  shell. Thus the value MR is given by:

$$MR = -AM^2(H, T) \quad (9.4)$$

At higher fields/ MR values, a deviation from the  $M^2$  behavior can be found. At higher temperatures, this deviation is rather small. Indeed, for the *REAuSn* compounds the  $M^2$  variation of the MR at low temperature is only valid for small fields (Figure 9.11). On the other hand, the negative MR is also found below the Néel temperatures for all of these compounds.

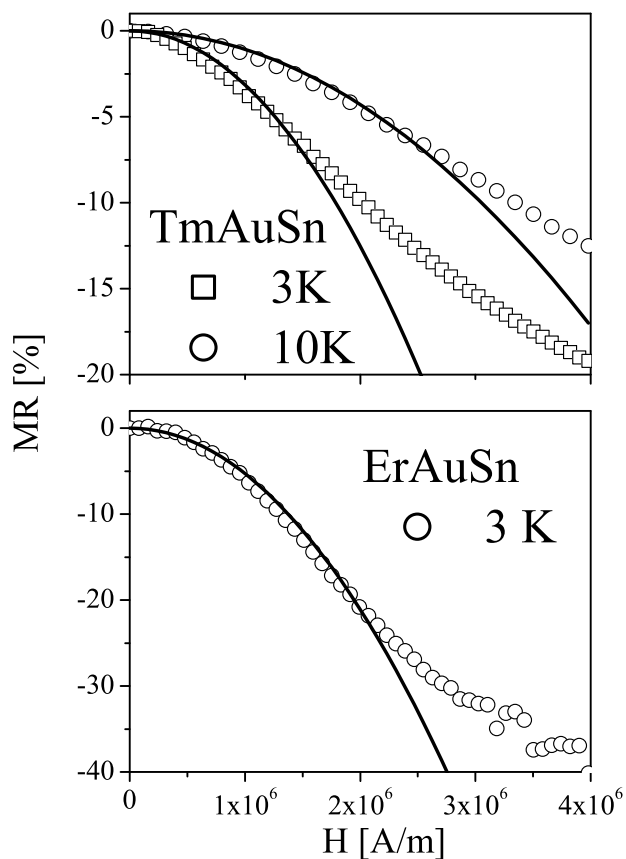


Figure 9.11: Magnetoconductance of TmAuSn at and below the metal – insulator transition temperature and of ErAuSn. Straight lines are fits using the expression 9.4.

## 9.7 Photoemission of ErAuSn

ErAuSn can be obtained in both the MgAgAs and the LiGaGe structure. Resistivity measurements show metallic behavior for hexagonal ErAuSn and semiconducting behavior for cubic ErAuSn (Figure 9.9). This result is in agreement with the calculated DOS of this compounds for both structure types (Figure 9.12).

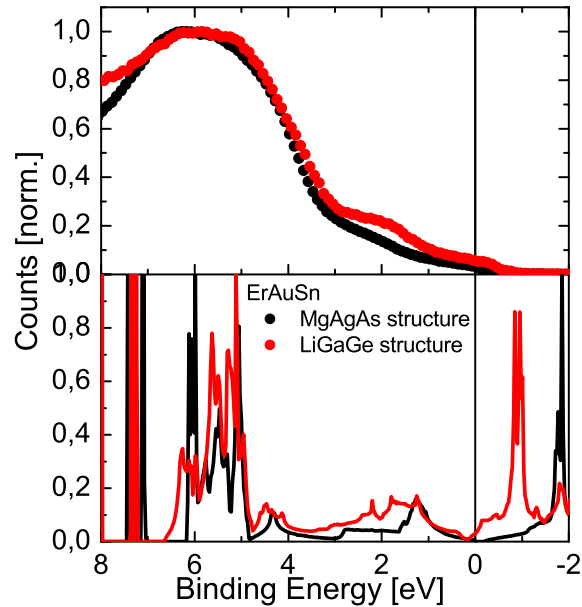


Figure 9.12: Photoemission spectra (top, excitation energy = 21.2 eV) and calculated DOS (bottom) for hexagonal and cubic ErAuSn

Figure 9.12 also shows the photoemission spectra (PE) for ErAuSn. At an excitation energy of 21.1 eV only the  $s$ ,  $p$  and  $d$  orbitals can be seen in the spectra, but not the  $f$  orbitals at  $\approx 7$  eV. The spectra are in good agreement with the calculated DOS for both structures. The Au  $d$  orbitals are lying between 5 – 6.5 eV. At  $\approx 2$  eV, the DOS for hexagonal ErAuSn shows more states than the DOS for cubic ErAuSn. This feature can also be seen in the PE spectra. At the Fermi edge, the PE spectra for both structures types also differ according to the semiconducting cubic ErAuSn and the metallic hexagonal ErAuSn.

## 9.8 Granular system

The x-ray powder diffraction analysis of granular systems based on MnAuSn and GdAuSn with a low concentration of one component (up to 5 %) is not precise enough to determine their phase composition. To verify the phase separation of both components in melted granular samples, we applied magnetic characterisation and Mössbauer spectroscopy. Antiferromagnetic ordering at  $T_N = 26$  K in GdAuSn and ferromagnetic transition at  $T_C = 570$  K in MnAuSn are clearly seen in the magnetisation curves of granular Gd - rich samples.

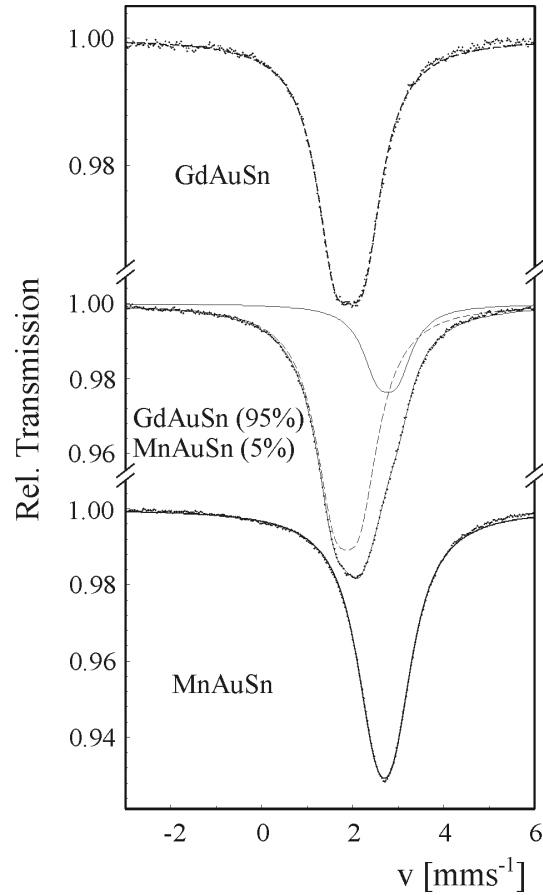


Figure 9.13:  $^{119m}\text{Sn}$  Mössbauer spectra of GdAuSn, MnAuSn and their 0.95/0.05 mixture at  $T = 80$  K.

The  $^{119m}\text{Sn}$  Mössbauer spectrum of a granular compound is well represented by two subspectra with parameters corresponding to GdAuSn and MnAuSn. Figure 9.13 shows  $^{119m}\text{Sn}$  Mössbauer spectra measured at 80 K for GdAuSn and MnAuSn. In the course of energy dispersion x-ray measurements (EDX), the size of the particles comprising the granular samples was estimated. Simultaneously the phase analysis was performed, which confirmed the two-phase composition of the samples. The maximum grain size in the granular phase  $(\text{GdAuSn})_{0.9}(\text{MnAuSn})_{0.1}$  of MnAuSn particles in a GdAuSn matrix is about  $20 \mu\text{m}$  (average  $\approx 5 \mu\text{m}$ ). Conductivity measurements show a metallic behavior for all granular samples. The important feature is a positive magnetoresistance of  $(\text{GdAuSn})_{0.1}(\text{MnAuSn})_{0.9}$  (sample I) below the antiferromagnetic transition in GdAuSn. Figure 9.14 shows the influence of the magnetic field on the conductivity of sample I at  $T = 3$  K and at  $T = 30$  K. The effect of increasing the resistance clearly drops above the antiferromagnetic ordering temperature of GdAuSn. Above the antiferromagnetic ordering temperature the small positive magnetoresistance can be a consequence of the additional scattering of the charge carriers due to the Lorenz force (see e.g. [151]). The resistance of sample I in a magnetic field of 2 T at 3 K is increased by 37%, in contrast

to a moderate 2.5% increase for  $(\text{GdAuSn})_{0.9}(\text{MnAuSn})_{0.1}$  (sample II). A positive magnetoresistance below  $T_N$  can also be found in other antiferromagnetic Gd - compounds, although a distinct explanation has yet not been found (see e.g. [152]).

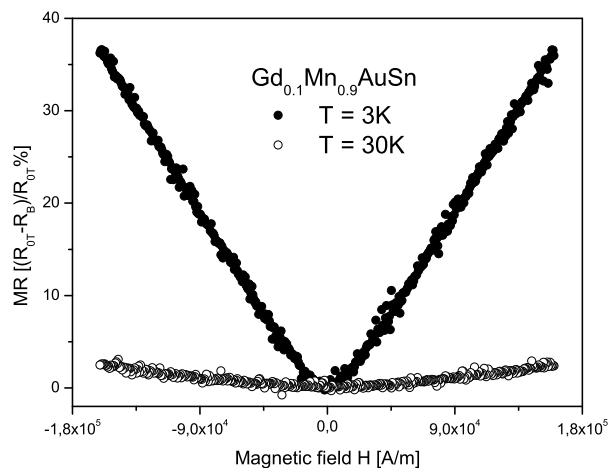


Figure 9.14: Magnetoresistance of the granular systems  $(\text{GdAuSn})_{0.1}(\text{MnAuSn})_{0.9}$  at  $T = 3$  K (open circles) and  $T = 30$  K (filled circles).

Significant intergrain magnetoresistance (IMR) has recently been observed in a number of polycrystalline half-metallic granular systems below the Curie temperature [153, 154, 155, 156, 157]. However in contrast to our observation, this phenomenon is characterized by a rapid drop of the resistance with applied field, followed by a slow decrease at higher fields [158]. In the publications cited, it has been shown that the IMR occurs at the grain boundaries, and that the large degree of the spin polarization specific for half-metallic ferromagnets is available for observing large scale effects. The main peculiarity of our observation is that the positive IMR effect is registered for a granular system based on a half-metallic ferromagnetic matrix with antiferromagnetic inclusions. Considering the importance for technological applications of magnetotransport in granular systems, more efforts should be invested in studying the behavior of spin polarized conduction electrons in the grain boundaries.

## 9.9 Summary and conclusion

Structural analysis of GdAuSn single crystal reveals the LiGaGe structure. Band structure calculations of GdAuSn based on the refined structural data demonstrated that this compound has a pseudo gap arising at the Fermi energy. The results of the calculations are in fair agreement with magnetic and Mössbauer measurements. The granular system GdAuSn/ MnAuSn shows an unusual high positive magneto resistance effect, while the ErAuSn and TmAuSn compounds show a giant magnetoresistance below a

---

metal-insulator transition in the paramagnetic regime. The magnitude of the GMR scales roughly with square of the  $4f$  magnetization, even below the magnetic ordering temperatures, and is due to the reduction of the spin – disorder scattering.



# 10 *RENiBi* Compounds

## 10.1 Introduction

To enhance thermoelectric, magnetic, piezoelectric, and other material characteristics has been a task for solid state chemists and physicists since many years. For a better understanding of the electronic properties, a comparison of experimental and theoretical results is important. Here both theoretic and experimental results on the ternary rare earth compounds *RENiBi* are presented. Although *RENiX* (with  $X = \text{Sb, Bi}$ ) have been known for some time [159, 126, 160], only for the *RENiSb* compounds further magnetic and electronic investigations were made [5, 129, 128, 161]. A remarkable feature of some *RENiSb* compounds is that despite the fact that they are composed of only metallic elements, they are semiconductors. The origin of the gap formation in these compounds was studied recently [162].

Since *RENiBi* are isoelectric to the *RENiSb* compounds, it can be assumed that similar properties within these compounds e.g. a large magnetoresistance at low temperature [161] will be found. The magnetoresistance of these compounds has been studied extensively [14, 101]. Magnetoresistance often appears in narrow gap semiconductors having an internal magnetic shell, thus one can expect large magnetoresistance in the *RENiBi* series, which have a smaller gap than the *RENiSb* compounds [162]. Also at low temperature possible EMR effect in the inhomogeneous semiconducting bulk compound *DyNiBi* and a high positive MR for *LuNiBi* at room temperature was found. To understand the structure-properties relationship, spin-polarized electronic band structure calculations were performed. Therefor the full potential linear augmented plane wave (FLAPW) method within the generalized gradient approximation (GGA) and the LDA+ $U$  scheme was used [64]. The results were compared with resistance and magnetic measurements.

## 10.2 Structural characterization

*RENiBi* crystallize in the cubic MgAgAs ( $C1_b$  structure,  $F\bar{4}3m$ ) structure type (Figure 10.1). The trivalent electro positive  $RE^{3+}$  ion of the  $RE^{3+}NiBi^{3-}$  compounds occupy the Mg sites. This structure can be described as filled MgAs, NaCl structure type in which Ni atoms inserted in half of the tetrahedral holes (Ag position) in the lattice. In this description, the compound can be viewed as either Ni atoms in the host  $RE^{3+}Bi^{3-}$  lattice or as filled ZnS zincblende type lattice  $NiBi^{3-}$  in which  $RE^{3+}$  atoms occupy octahedral holes. Not counting equivalent permutations this face-centered cubic structure has three possible different atomic distributions. The intensity data of the XRD measurement agrees only with the following atomic positions:  $RE$  at  $4b$  ( $\frac{1}{2}\frac{1}{2}\frac{1}{2}$ ), Ni at  $4c$  ( $\frac{1}{4}\frac{1}{4}\frac{1}{4}$ ) and Bi at  $4a$  (0 0 0). For this distribution, the 200 is calculated to be much stronger than the 111 reflection. For the two other distributions it should be the other way round, which is in disagreement with the experimental data.

The structure can also be thought of as the Heusler structure ( $L2_1$  structure,  $Fm\bar{3}m$ ) where half of the octahedral sites are empty (figure 10.1). Thus Ni atoms can occupy the vacant site, and anti phase domains corresponding to the inversion of  $RE$  and Bi may occur. Such kind of defects are not easily detected by X-ray or neutron diffraction, but can have significant impact on the resistance of the polycrystalline samples. The vacant site leads to less overlap between the transition metal wave functions, thus to narrower bands, and may lead to gaps in the density-of-states (DOS) spectrum. On the other hand, a Ni occupancy of the vacant site will lead to a closed gap, thus to metallic behavior. For this reason - using the example  $ErNiBi$  and the hypothetical compound ' $ErNi_2Bi$ '- the powder patterns were calculated for both structure types. The results are shown in Table 10.1. Although both calculated pattern do not perfectly fit to the experimental data, the MgAgAs structure for  $ErNiBi$  is in better agreement with the experiment.

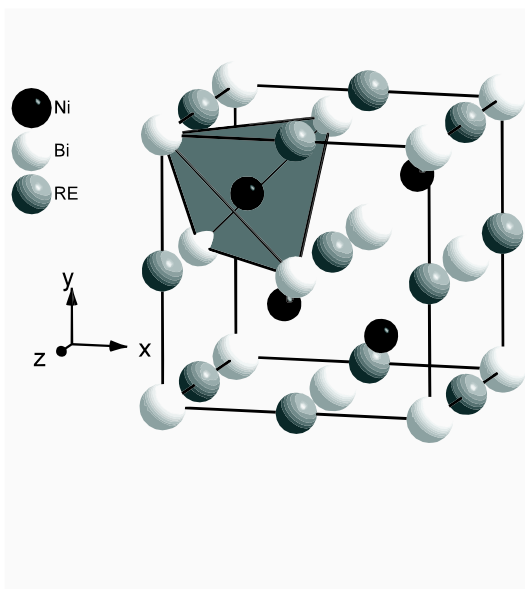


Figure 10.1: Structure of  $RENiBi$  (Half-Heusler structure,  $F\bar{4}3m$ ). A filled tetrahedral site is emphasized with lines.

Table 10.1: Calculated ( $I_C$ ) and observed ( $I_0$ ) x – ray diffraction intensities of *ErNiBi* with *MgAgAs* (Half-Heusler-) structure and hypothetical *ErNi<sub>2</sub>Bi* with *MnCu<sub>2</sub>Al*- (full-Heusler-) structure. The pattern was recorded with *CuK $\alpha$*  radiation.

Angle $2\theta$	$hkl$	$I_C$ <i>ErNiBi</i>	$I_0$	$I_C$ ' <i>ErNi<sub>2</sub>Bi</i> '
24.118	111	7.43	12.2	1.41
27.919	200	62.21	85.2	25.12
39.895	220	100	100	100
47.162	311	3.60	6.9	0.75
49.395	222	18.39	17.2	8.99
57.694	400	17.12	16.2	16.95
63.439	331	1.47	1.7	0.36
65.288	420	24.63	19.6	12.22
72.442	422	34.89	20.9	34.25
77.821	511/333	0.82	0.8	0.22
86.050	440	11.39	4.5	11.09

Table 10.2 shows the lattice parameters of the *RENiBi* compounds and the *RE-RE* distances. All are in good agreement with previous results [126, 160]. The cell volume decreases from the praseodymium to the lutetium compound as expected from the lanthanoid contraction.

Table 10.2: Lattice parameter, cell volume and *RE - RE* distance of *RENiBi* with cubic *MgAgAs*-Type structure

Compound	a [ $\text{\AA}$ ]	V [ $\text{nm}^3$ ]	<i>RE-RE</i> distance [nm]
PrNiBi	6.508(1)	0.2757	4.601(9)
SmNiBi	6.433(6)	0.2663	4.549(2)
GdNiBi	6.433(1)	0.2662	4.548(9)
TbNiBi	6.413(5)	0.2660	4.535(1)
DyNiBi	6.410(8)	0.2634	4.533(1)
HoNiBi	6.391(1)	0.2611	4.519(1)
ErNiBi	6.386(3)	0.2605	4.515(8)
TmNiBi	6.371(0)	0.2586	4.505(0)
LuNiBi	6.335(1)	0.2542	4.479(5)

### 10.3 Magnetic measurements

The temperature dependence of the magnetization of the *RENiBi* ( $RE = \text{Pr, Sm, Gd-Tm}$ ) in a magnetic field of  $4 \times 10^6 \text{ Am}^{-1}$  show anomalies for all compounds except for *LuNiBi* (not shown here) in the temperature regime of 1.8 - 300 K (Figure 10.2). The observed maxima and the negative paramagnetic Curie - temperatures indicate antifer-

romagnetic coupling between the moments of the rare earth compounds. Above 50 K the magnetic susceptibilities obey the Curie-Weiss law. The values of the paramagnetic Curie temperature  $\theta_P$  and the effective magnetic moment  $\mu_{eff}$  were obtained from a Curie-Weiss fit of the experimental data. The effective magnetic moments are close to the  $RE^{3+}$  free-ion values of  $\mu_{eff}(theo) = g_j[J(J+1)]^{1/2}$  (Table 10.3), indicating that Ni and Bi carry no magnetic moment.

As shown in Figure 10.2, the susceptibilities for GdNiBi, TbNiBi and DyNiBi are increase below  $T_N$  (at around 10, 5 and 2 K, respectively). This could be due to a more complex magnetic ordering (like canted magnetic moments) or ferromagnetic ordering. Such a type of weak ferromagnetic behavior in a ternary rare earth compound with a small magnetic moment is found e.g. in GdPdSb [30]. LuNiBi is paramagnetic, the susceptibility shows Curie – behavior down to 1.8 K.

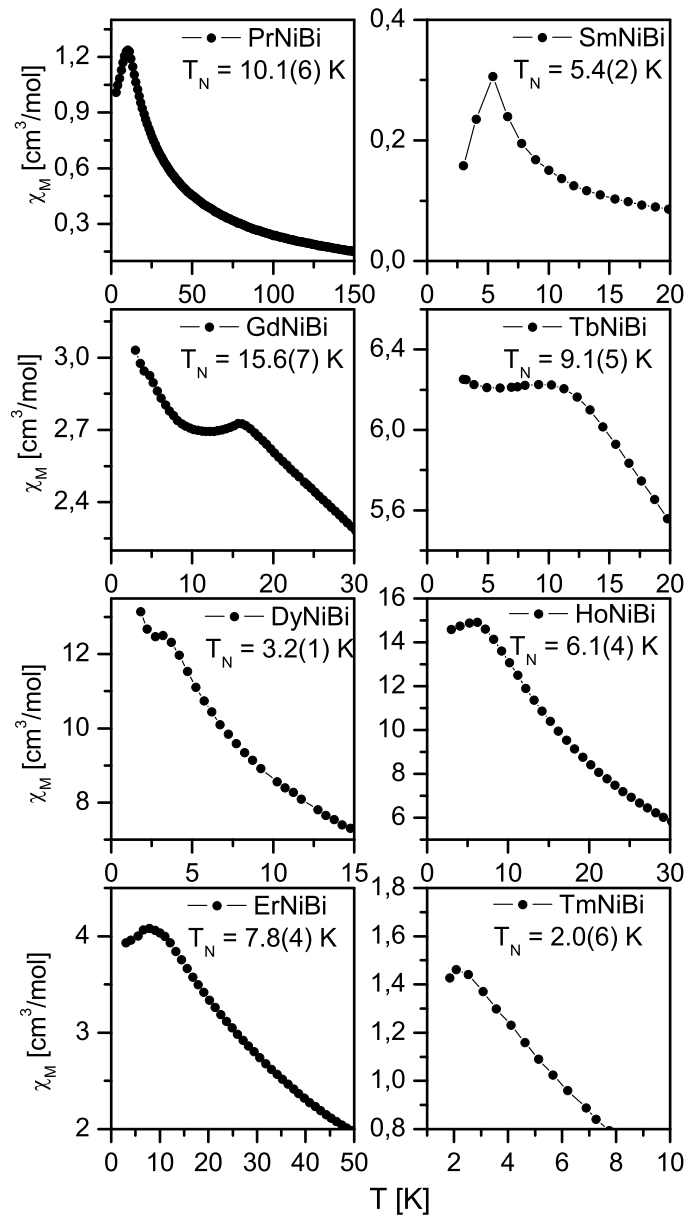


Figure 10.2: Temperature dependence of the magnetization of *RENiBi* compounds in a magnetic field of  $4 \times 10^6$  Am<sup>-1</sup>

Table 10.3: Magnetic properties of *RENiBi* ( $RE = \text{Pr, Sm, Gd-Tm, Lu}$ ) compounds. The theoretic moments are obtained from  $\mu_{eff}(theo) = g_j[J(J+1)]^{1/2}$ .

Compound	$T_N$ [K]	$\theta_P$	$\mu_{eff}$ [ $\mu_B$ ]		Type of Magnetism
			Exp.	Theo.	
PrNiBi	10.1(6)	-9.2(9)	3.9(1)	3.58	Curie-Weiss
SmNiBi	5.4(2)	-4.9(2)	0.9(2)	0.84	Curie-Weiss
GdNiBi	15.6(7)	-25.5(1)	7.8(6)	7.94	Curie-Weiss
TbNiBi	9.1(5)	-14.8(6)	9.4(7)	9.72	Curie-Weiss
DyNiBi	3.2(1)	-15.8(2)	10.3(5)	10.63	Curie-Weiss
HoNiBi	6.1(4)	-2.8(4)	10.6(9)	10.6	Curie-Weiss
ErNiBi	7.8(4)	-18.6(1)	9.8(1)	9.59	Curie-Weiss
TmNiBi	2.0(6)	-12.1(9)	7.7(1)	7.57	Curie-Weiss
LuNiBi	-	-	0	0	paramagnetic

The  $RE^{3+} - RE^{3+}$  distances are large (see Table 10.2), indicating that the magnetic interactions have an indirect character that could be described by the RKKY model interaction. In this model both the paramagnetic Curie and the ordering temperatures are proportional to the de Gennes factor  $G = (g_j - 1)^2 J(J+1)$  [138]. The dependence of the ordering temperatures on the rare earth atom is shown in Figure 10.3. For the *RENiBi* compounds the dependence of  $\theta_P$  and  $T_N$  on the *RE* element does not satisfy the de Gennes scaling. PrNiBi shows a strong derivation from the de Gennes scaling, while the derivation for compounds with heavier *RE* atoms is smaller. This indicates that the simple RKKY model is not suitable for the description of the magnetic properties of the *RENiBi* compounds.

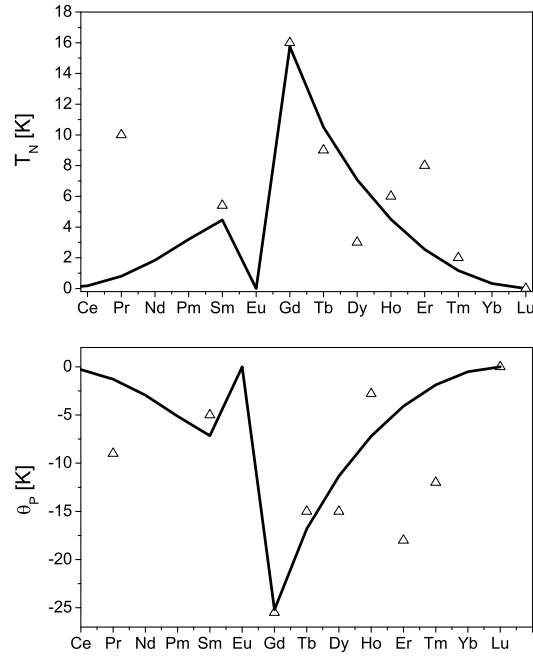


Figure 10.3: Magnetic ordering temperatures  $T_N$  (top) and paramagnetic Curie  $\theta_P$  (bottom) of *RENiBi* compounds as a function of the rare earth atom: solid curve, prediction of the de Gennes scaling whereby  $T_N$  should be maximum of the Gd-containing compounds;  $\Delta$  experimental data

## 10.4 Conductivity measurements

The resistance of the *RENiBi* compounds is shown in Figure 10.4 (normalized to 300K for comparison). In the upper panels all compounds with metallic behavior are displayed. The resistance of these compounds steadily decreases from 2 to 300 K with one exceptions. At temperatures below 11 K the curve of PrNiBi is increasing. This could be attributed to the antiferromagnetic ordering at  $T_N = 10$ K. For the metallic compound TmNiBi the change of the slope at the corresponding magnetic ordering temperatures is too low. For SmNiBi the resistance curve does not show any sharp anomaly, and instead reveals only a change in curvature, which can be attributed to excited crystal field levels.

The lower panels of Figure 10.4 show the semiconducting *RENiBi* compounds with a metal-insulator transition. For the temperature range 250 - 300K, the resistivity  $\rho_a$  follows the activation law as described in equation 9.2.  $E_{gap}$  is summarized in Table 10.4. For temperatures lower than 50 K a metallic-like behavior is observed. Such a behavior is typical for conduction through an impurity band that overlaps the conduction band. The resistivity  $\rho_m$  can be approximated by Equation 9.3 with  $\alpha \approx 0.6$  for ErNiBi and

DyNiBi and  $\alpha \approx 0.5$  for LuNiBi and GdNiBi. Thus the complete temperature dependence can be described by the conduction of parallel channels, one corresponding to the metallic conduction and the other to the thermal activation. The metal - insulator transition strongly depends on the preparation conditions, e.g., longer annealing of the samples shifts the transition to lower temperatures.

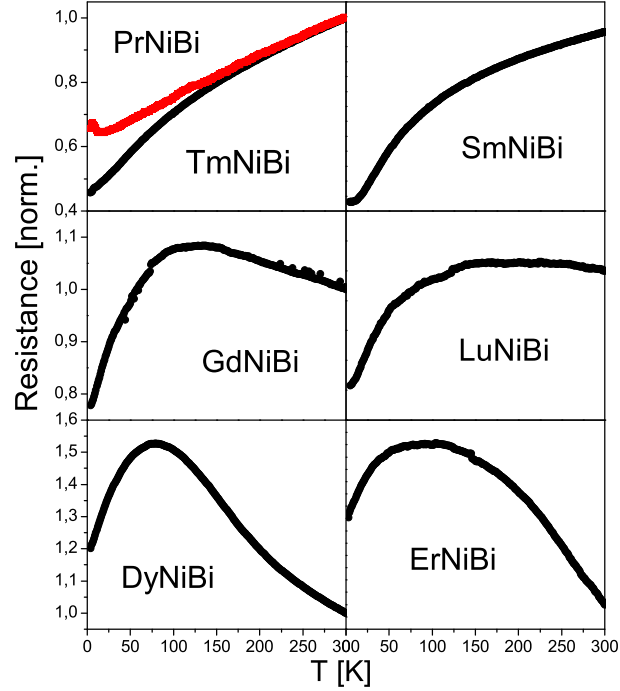


Figure 10.4: Normalized Resistance in the temperature range from 3K to 300K of metallic (top) and semiconducting (bottom) *RENiBi* compounds.

Table 10.4: Electrical behavior of *RENiBi* ( $RE = \text{Pr, Sm, Gd, Dy, Er, Tm, Lu}$ ) compounds. (SC = semi conductor; SC-metal = semi conductor to metal transition).

Compound	measured	band gap	theoretic	band gap
PrNiBi	metal	-	metal	-
SmNiBi	metal	-	metal	-
GdNiBi	SC - metal	2.5 meV	SC	314 meV
DyNiBi	SC - metal	10 meV	SC	256 meV
ErNiBi	SC - metal	16 meV	SC	195 meV
TmNiBi	metal	-	metal	-
LuNiBi	SC - metal	2meV	SC	121 meV

## 10.5 Band structure calculations

The description of the density of states (DOS) and the band structure for this compound were provided by using experimentally obtained lattice parameters (see Table 10.2). Additionally, calculations were performed for the hypothetical  $\text{ErNi}_2\text{Bi}$  compound. In the six panels of figure 10.5 the densities of states (DOS) near the Fermi energy  $E_F$  for  $\text{RENiBi}$  ( $RE = \text{Pr, Gd, Er, Tm, Lu}$ ) and  $\text{ErNi}_2\text{Bi}$  are compared. The DOS of the semiconducting compounds ( $RE = \text{Gd, Dy}$  (DOS not shown here),  $\text{Er, Lu}$ ) show nearly the same electronic structure between -6 and 0 eV below the Fermi energy. This structure mainly comes from the Ni 3*d* levels. Only a small contribution comes from occupied Bi 5*s* 5*p* orbitals. The well localized electrons at  $\approx 11$  eV are Bi 5*s* electrons in all compounds. Above the semiconducting gap are empty Ni 3*s* 3*p* and unoccupied Bi 5 *p* orbitals. The occupied *f* orbitals are at 6.4 eV – 9,1 eV, -7.6 eV and -7.6 eV for the Er, Gd and Lu compound, respectively, while the unoccupied *f* orbitals of  $\text{GdNiBi}$  and  $\text{ErNiBi}$  lie well above the Fermi Energy.

For the metallic compounds Sm (not shown here), Tm and Pr the situation at the Fermi edge changed drastically. For the  $\text{TmNiBi}$  the electron configuration of a  $\text{Tm}^{3+}$  ion with twelve occupied 4*f* orbitals shifted downward by  $U_{eff}/2 = (U - J)/2$  and two unoccupied orbitals shifted upwards this amount was taken. On the other hand it was emphasized that the 4 *f* states are not completely localized, but may hybridize, and together with all other states their energy position relax to self consistency. In principle this scenario was chosen for all the  $\text{RENiBi}$  compounds with their appropriate number of occupied and unoccupied 4*f* orbitals. Although a  $U_{eff}$  was applied, the twelve occupied orbitals of  $\text{Tm}^{3+}$  ions lie only between -0.8 eV and 2,3 eV below the Fermi energy, while one unoccupied 4 *f* orbital is located 4.8 eV above the Fermi energy. A hole 13th *f* level is pinned at the Fermi energy, despite the fact that the starting configuration in the calculation was completely empty 13th and 14th *f* level. The pinning of the 13th *f* level happens irrespective of the  $U$  and  $J$  values. Such pinning was found e.g. for  $\text{TmS}$  [163]. For  $\text{SmNiBi}$  nearly the same situation is found. Here five 4 *f* orbitals are shifted downward and nine upwards while the 6th *f* level is pinned at the Fermi energy.

For the  $\text{PrNiBi}$  compound the case is different. For this compound primarily 3*d* states from Ni are at the Fermi energy. The DOS for the hypothetical compound  $\text{ErNi}_2\text{Bi}$  metallic behavior. Thus Ni atoms filling up the empty octahedral sites in the structure would destroy the gap in the semiconducting compound. This would explain the smaller gaps seen experimentally as compared with the calculated ones. On the other hand, the calculated metallic and semiconducting ground states are in perfect agreement with the experiments.

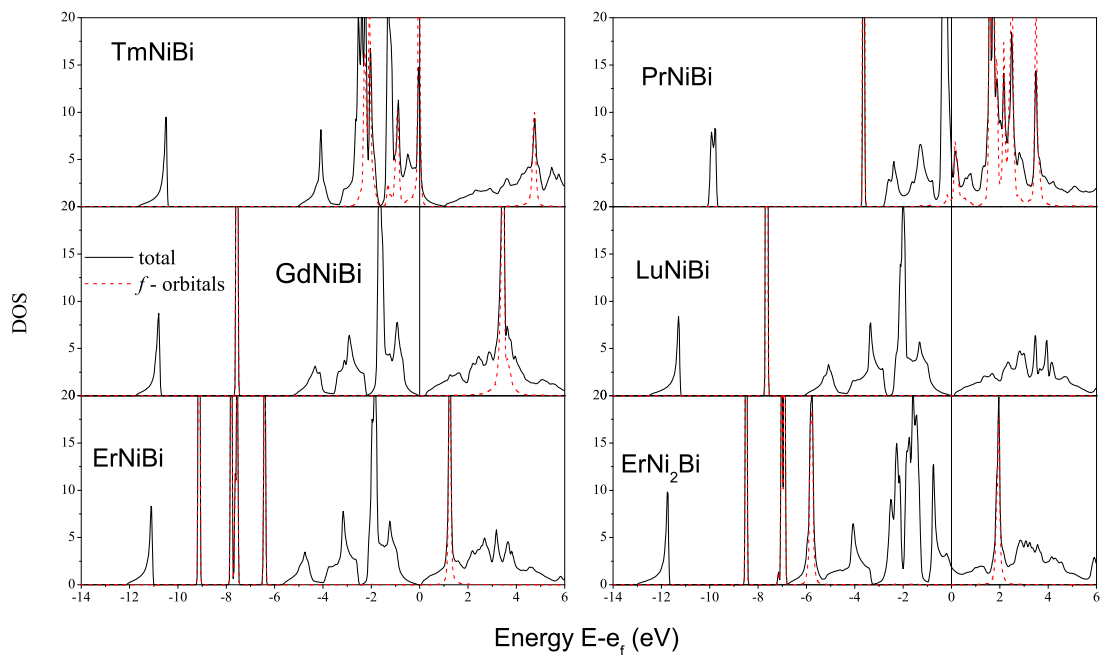


Figure 10.5: Density of states (DOS) of some *RENiBi* and hypothetical  $\text{ErNi}_2\text{Bi}$  compounds.

## 10.6 Magnetoresistance

Non-magnetic rare earth compounds have a low positive magnetoresistance. This weak MR may arise from the additional scattering of the charge carriers due to the Lorentz force (e.g. [151]). Figure 10.6 shows the electrical resistance and magnetoresistance of *RENiBi* compounds. Above the metal – insulator transition these compounds show nearly no magnetoresistance (MR). At the transition a small negative MR is observed, whilst below this transition in every compound the magnitude of the MR considerable higher.

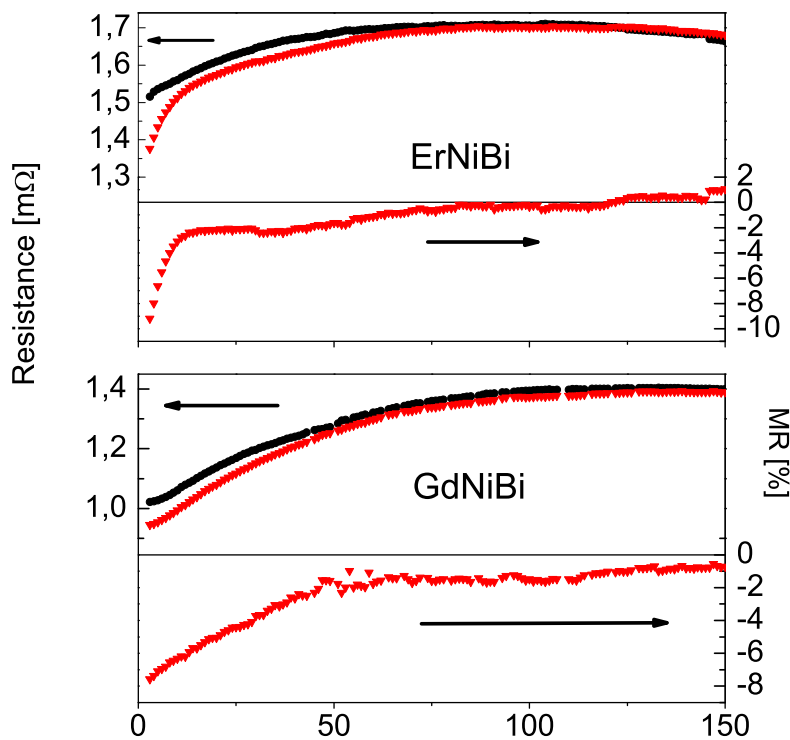


Figure 10.6: Electrical resistance of *RENiBi* compounds without and with an externally applied field of  $1.6 \times 10^6$  A/m. Below each plot the respective magnetoresistance (MR).

The DyNiBi compound shows the highest negative MR value. Even at the metal – insulator transition a MR of up to 10 % is found in fields up to  $7.1 \times 10^6$  A/m (Figure 10.7). The negative magnetoresistance in semiconductors is discussed due to two different origins: The reduction of the gap arising from the splitting of the up- and down- spins subbands, and the spin disorder scattering is reduced due to the alignment of moments under a field. For LuNiBi, where no magnetic  $4f$  shell is present, a positive magnetoresistance is found, thus for the *RENiBi* the contribution to the narrowing of the gap is negligible.

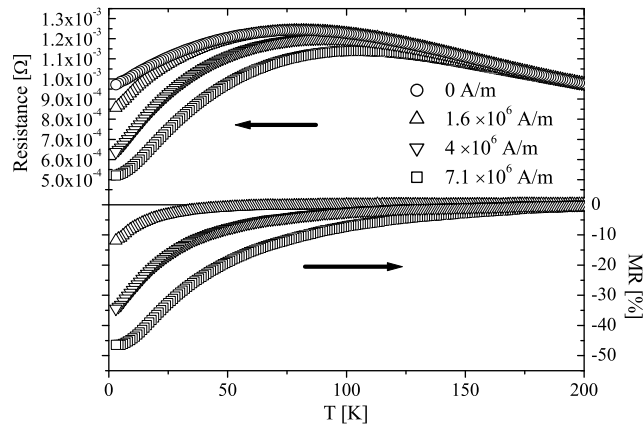


Figure 10.7: Electrical resistance in the presence of externally applied magnetic fields ( $H$ ) and magnetoresistance (MR) as a function of temperature ( $T$ ) for DyNiBi.

For similar rare earth containing semiconductors with a magnetic transition, a negative MR is found that is proportional to the square of the magnetization of the  $4f$  shell for low MR values in the paramagnetic state [101]. Thus the value MR is given by Equation 9.4. At higher fields/ MR values, a deviation from the  $M^2$  behavior can be found. At higher temperatures, this deviation is rather small. Only for the DyNiBi at the metal – insulator transition can this deviation be found (Figure 10.8).

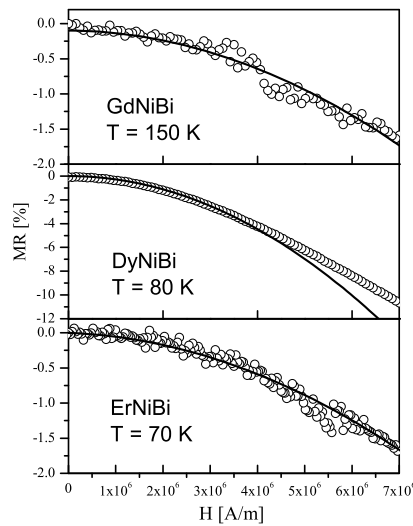


Figure 10.8: Magnetoresistance of *RENiBi* samples at the respective metal – insulator transition temperatures. Straight lines are fits using Expression 9.4.

## 10.7 Inhomogeneous DyNiBi compound

Scanning electron microscope (SEM) measurements reveal the inhomogeneity of the sample (Figure 10.9). Small semimetallic Bi dots (A) are clearly visible in the semiconducting DyNiBi matrix. The Bi dots on the surface (B) are due to the soft polishing process. The size of the Bi dots is 400 - 800 nm.

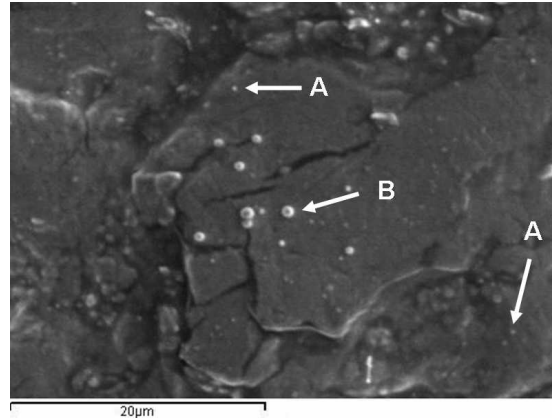


Figure 10.9: Scanning microscope image of a polished DyNiBi surface. Arrows mark Bi dots in the DyNiBi matrix (A) and on the surface (B) due to soft polishing.

Figure 10.10 shows the field dependence of the resistance at 80 K (open circles). The MR does not follow the  $M^2$  behavior. As seen in Figure 10.10, the sign of the MR changes in low fields at 10 K. The magnitude of the positive MR is slightly different for the measured different samples. The compound with the higher impurity content shows a slightly higher positive MR.

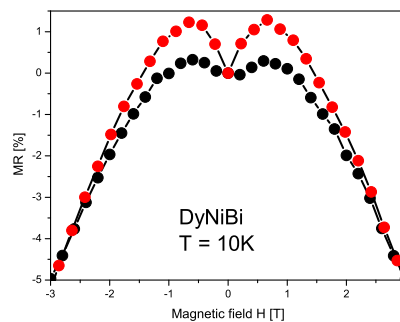


Figure 10.10: Field dependence of the resistance at 10 K. Two samples with slightly different bismuth impurities were measured (red dots = higher impurity content).

The positive MR in low fields and at low temperatures can be explained in two different ways. First, it could be due to changes to the density of states and mobility for up- and down-spin carries as found in EuSe [164]. Second, the positive MR could be caused by the metallic bismuth impurities. The embedded bismuth acts as a short circuit with most of the applied current passing through it. When a magnetic field is applied, the semimetallic inhomogeneities act as open circuits and the total resistivity rises [165]. This geometric contribution to the GMR, the so-called extraordinary magnetoresistance (EMR) constitutes a significant change of the MR at fields below 6 kOe. The magnitude of the positive MR changes at different impurity content of the samples. The sample with a slightly higher Bi content (red dots in Figure 10.10) shows a higher positive MR. Thus the positive MR is more likely attributed to the EMR. In higher fields, the EMR is overwhelmed by the negative GMR. Similar to other semiconducting rare earth compounds, this effect is due to the polarization of the current carriers by the 4 *f* shell [101].

## 10.8 LuNiBi

Due to the the 18 valence electrons and a complete filled *f* orbitals LuNiBi is a non-magnetic compound. This is also in agreement with band structure calculations. Nevertheless a magnetoresistance effect was found. Figure 10.11 shows the resistance in the presence of an applied field of  $1.6 \times 10^6$  A/m. The MR value is positive throughout the whole temperature range and reaches up to 120% at 3 K. Most non-magnetic rare earth compounds have a small positive MR up to 2%. This weak MR may arise from the additional scattering of the charge carriers due to the Lorentz force (e.g. [151]), but here the value is too high.

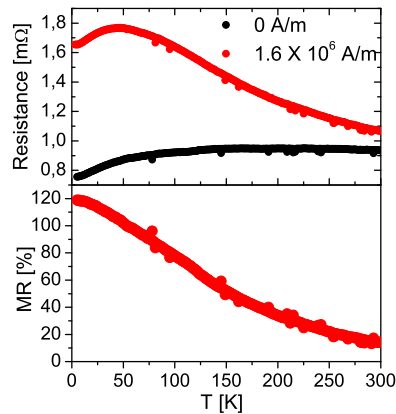


Figure 10.11: Electrical resistance in the presence of an externally applied magnetic field ( $H$ ) and magnetoresistance (MR) as a function of temperature ( $T$ ) for LuNiBi.

Figure 10.12 shows the field dependence of the resistance at 300K and 5K. Here the value reaches 130% at high fields and low temperature. The MR value of 28% at room temperature, which makes this compound interesting for applications. Although this compounds shows small Bi impurities ( $\leq 1\%$ ), the large MR value can not explained by the EMR effect.

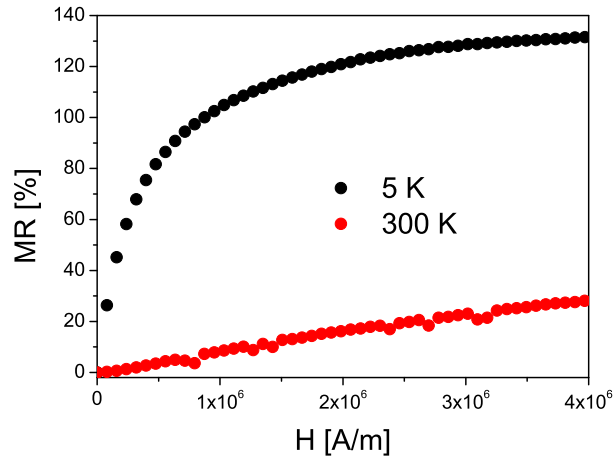


Figure 10.12: Field dependence of the resistance at 300 K.

## 10.9 Summary

In summary, magnetic and transport properties of the *RENiBi* ( $RE = \text{Pr, Sm, Gd-Tm, Lu}$ ) compounds were presented. LDA +  $U$  calculations confirm the antiferromagnetic ground state of these compounds. Only for LuNiBi a paramagnetic ground state was found in experiment and theory. Also the transport properties for these compounds are in good agreement with the band structure calculations.

A GMR effect has been observed in *RENiBi* compounds, like those occurring in several other rare earth semiconductors. Although these compounds order antiferromagnetically, a metal – insulator transition was found. The magnitude of the GMR scales roughly with square of the  $4f$  magnetization, even below the magnetic ordering temperatures, and is due to the reduction of the spin – disorder scattering. The highest magnitude of the GMR was found for DyNiBi, which also has the biggest spin-orbit coupling. It is a theoretically challenging task to understand how the spin–disorder contribution becomes apparently large and also temperature dependent in the paramagnetic state of some antiferromagnetic intermetallic compounds. However, in the case of ferromagnets, there is a recent theoretical attempt to understand such GMR anomalies in terms of critical point effects [166]. A higher charge carrier density should shift the GMR to higher temperatures [167].

Due to small Bi inhomogeneities in DyNiBi, the compound also shows a positive MR

at low temperatures and fields whose origin can be explained by the extraordinary magnetoresistance effect (EMR). For these cases, the EMR is suppressed in higher fields by the negative MR of the DyNiBi phase. By tuning the bismuth impurities, the EMR effect is affected. Semiconductor-metal hybrid structures are considered to be of enormous technological interest for the development of ultrafast read heads. Using this approach could lead to the development of a simple bulk sensor for magnetic fields.

LuNiBi shows a large positive MR even at room temperature, which makes this compound interesting for applications.

# 11 Summary and Outlook

## 11.1 Summary

This work shows some interesting details in the field of *REME* compounds. The main focus here was on *REME* compounds with MgAgAs and LiGaGe structure, which only exist with 18 valence electrons. Examples for half-metallic ferromagnets with LiGaGe structure, giant magnetoresistance, intergrain magnetoresistance and extraordinary magnetoresistance were shown. The magnetic and electronic properties were compared with band structure calculations. A particular highlight is the large positive magnetoresistance of the LuNiBi compound.

### Structure

It was demonstrated that *REME* compounds with cubic MgAgAs structure are semi-conducting, while those with hexagonal LiGaGe structure can become semiconducting depending on the degree of puckering.

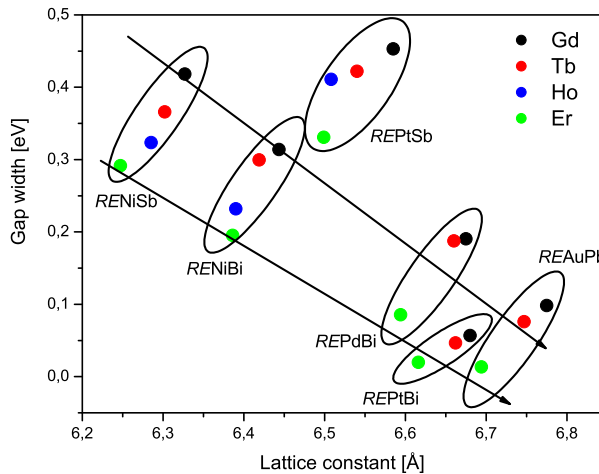


Figure 11.1: Calculated band gaps form some *REME* compounds with MgAgAs structure.

Figure 11.1 shows the calculated band gaps for some *REME* compounds with MgAgAs structure. Two trends can be seen in this picture: First, within a *REME* series with the same *ME* atoms, the band gap is larger for larger lattice parameters or a lighter rare earth atom. Second, within a *REME* series with the same *REM* atoms, the band gap is smaller for larger lattice parameters or a heavier metal atom. The largest band gaps

seem to exist in the *REPtSb* series, the smallest among the *REAuPb* compounds. For *GdAuSn*, the structure was reported to have *CaIn<sub>2</sub>* structure, but X-ray measurements of a single crystal reveals the ordered *LiGaGe* structure. Filling up these compounds with magnetic ions would lead to half-metallic ferromagnets. *REME* compounds with more or less than 18 valence electrons should be metallic, like *GdAuCd*, *GdAuMg* and *GdAuIn* (*ZrNiAl* structure). Also, the effect of Au–X covalency in these compounds was examined. The Au *d* states occupy the same energy range as the In and Mg states, suggesting a significant Au–X covalency. The In *s* lone pair in *GdAuIn* has more localized behavior as compared with Mg *s* in *GdAuMg*.

### Magnetism

The magnetism of some *REME* was examined. As expected from band structure calculations and similar compounds, all order antiferromagnetic at low temperatures. Due to high neutron absorption cross-section of Gd, neutron diffraction is not possible for Gd-containing *REME* compounds. Thus, *GdNiSb* and *GdPdSb* were examined with <sup>155</sup>Gd Mössbauer measurements. With these measurements the magnetic ground states of both structure types of the biphasic compound *GdNiSb* could be obtained. For *GdPdSb*, the magnetic measurements show a second magnetic transition below the antiferromagnetic transition. From the results of Mössbauer measurements, a canted ferromagnetic ordering is likely to exist at low temperature. Indeed, electronic structure calculations show only a marginal energy difference between ferromagnetic and antiferromagnetic ground states. For the ferromagnetic case, band structure calculations predict itinerant states in the minority band and weak localized states in the majority band. According to the classification scheme for half metals as proposed by Coey et al. [62], *GdPdSb* belongs to the class of Type III half metal. This is the first half metallic ferromagnet with a *LiGaGe* structure. The results show that <sup>155</sup>Gd Mössbauer spectroscopy is a powerful tool to examine the magnetic ground state of intermetallic compounds.

### Magneto resistance

Several magnetoresistance effects were found among the *REME* compounds. *RENiBi* and *REAuSn* compounds with *MgAgAs* structure are semiconducting according to band structure calculations although these compounds order antiferromagnetically. Experimentally, a metal – insulator transition was found. For these compounds a **GMR** effect has been observed, which is related to the metal – insulator transition. The magnitude of the GMR scales roughly with square of the *4f* magnetization at low magnetic fields, even below the magnetic ordering temperatures. The highest magnitude of the GMR was found for *DyNiBi*, which also has the biggest spin-orbit coupling. Metallic *REME* compounds show nearly no MR effect. Due to small Bi inhomogeneities in *DyNiBi*, the compound also shows a positive MR at low temperatures and fields whose origin can be explained by the extraordinary magnetoresistance effect (**EMR**). For these cases, the EMR is suppressed in higher fields by the negative MR of the *DyNiBi* phase. The EMR can be tuned by variation of the bismuth content. *LuNiBi* shows a large positive

MR even at room temperature, which makes this compound interesting for applications. Doping with Mn at the Gd position for the GdAuSn compound was not possible but leads to a granular system. This granular GdAuSn/ MnAuSn system shows an amazingly high positive **granular MR** below the antiferromagnetic ordering temperature of GdAuSn.

In summary, this work has four main aspects on the search for new materials for spintronics: First, the half metallic compound GdPdSb, which is the first half-metallic ferromagnet with LiGaGe structure, was found. Second, the presence of a giant magnetoresistance in *REME* compounds with MgAgAs structure. The GMR is related to a metal-insulator transition, and the value of the GMR depends on the value of the spin-orbit coupling. Third, the inhomogeneous DyNiBi compound shows a small positive MR at low temperature that depends on the amount of metallic impurities. And fourth, the LuNiBi compound was found, which shows a positive GMR of 27.5% at room temperature.

## 11.2 Outlook

As shown in this thesis, *REME* compounds with 18 valence electrons show interesting properties concerning spintronic applications. Thus further investigations should be made with these compounds.

### **Tuning the charge carrier concentration of *REME* compounds**

For non-rare earth containing half-Heusler compounds, the charge carrier concentration can easily be obtained via doping. In case of the rare earth compounds, doping seems to either change the structure or leads to granular systems. Only substituting with ions of the same valence electron number should work. Thus investigation should be made on the cubic *REPdBi* and *REPtBi* compounds, and mixtures thereof.

### **Investigation of the influence of metallic impurities on the properties of *REME* compounds**

To understand the relation between magnetoresistance and impurity in inhomogeneous compounds, high resolution microscopy methods (transition microscopy, photoemission electron microscopy) should be used. Also the impurity value has to be varied. With LuNiBi, a compound with a large MR at room temperature was found. As it is still unclear if the positive value in this compound comes only from the impurities or another reason, further investigation is a must. This could lead to new, cheap sensors for spintronic applications.

### **Giant magnetoresistance in *REME* compounds: Influence of the spin-orbit coupling**

Variation of the charge carrier density and the spin orbit coupling by changing the rare earth atom and the preparation conditions has an impact on the value of the GMR effect

in *REME* compounds. In particular, the influence on the metal – insulator transition should be determined to shift it to higher temperatures.

### **Magnetism in *REME* compounds: Mössbauer and neutron diffraction**

As shown in this thesis, the energy difference between antiferromagnetic and ferromagnetic ground state of GdPdSb is marginal. After the antiferromagnetic ordering temperature, the magnetic susceptibility is rising again.  $^{155}\text{Gd}$  Mössbauer measurements indicate a canted ferromagnetism for this compound at low temperature. Such kind of low temperature magnetic behavior is seen for some more *REME* compounds like GdNiBi and TbNiBi.  $^{155}\text{Gd}$  Mössbauer measurements for Gd-containing compounds and neutron diffraction for non-Gd-containing compounds should be made to determine the magnetic ordering at low temperature.

### **Thermoelectric properties of *REME* compounds**

Recently, it was shown that some *REME* compounds are interesting for thermoelectric applications (e.g. [168]). However, until now only a few investigation had been made in this field. Thermoelectrics are compounds that show an electric potential difference when a temperature gradient is applied. This difference can be used to generate electric power. Compounds with small band gaps like *RENiBi* compounds should be more convenient for thermoelectric applications.

### **Ultraviolet and resonant photoemission of *REME* compounds**

Still a challenging task is the theoretical examination of *REME* compounds by band structure calculations. To back up the calculation results, ultraviolet photoemission (UPS) can help to determine the shape of valence band and thus the band gap in these compounds. In this thesis, only one value for  $U_{eff}$  was used in the LDA +  $U$  calculations. With resonant photoemission, the exact energy location of the  $f$  orbitals can be determined and thus the calculations can be more precise.

# List of Figures

1.1	Periodic table of elements, <i>REME</i> elements are marked blue, red and green, respectively . . . . .	5
1.2	Theoretical effective magnetic moments $\mu_{eff}$ of the free $RE^{3+}$ ions . . . . .	9
1.3	Prediction of the de Gennes scaling for the magnetic ordering temperatures $T_N$ (top) and paramagnetic Curie $\theta_P$ (bottom) of <i>REME</i> compounds as a function of the rare earth atom, whereby $T_N$ should be maximum in the Gd – containing compounds . . . . .	10
1.4	Angular dependence (for fields parallel and perpendicular the the sample) of the AMR effect. . . . .	12
1.5	A multilayer system Fe–Cr–Fe with ferromagnetic (left) and with antiferromagnetic (right) exchange coupling between the iron layers. . . . .	13
1.6	A typical tunnel magneto-resistance device (TMR) . . . . .	14
1.7	Granular magnetoresistance . . . . .	15
1.8	Room temperature magneto resistance of a composite van der Pauw disk (top picture) of InSb and Au for a number of values of $\alpha = r_a/r_b$ . The symbols correspond to an $\alpha$ between 0 and $\frac{15}{16}$ , increasing from top to bottom [54]. . . . .	16
1.9	Schematic density of states (DOS) of a half–metallic ferromagnet. . . . .	17
3.1	MgAgAs structure of <i>REME</i> compounds a) and the corresponding simple antiferromagnetic structure b) (Spin of <i>RE1</i> inverse to spin of <i>RE2</i> ) . . . . .	22
3.2	a) LiGaGe structure of <i>REME</i> compound and the corresponding simple antiferromagnetic structures for b) HEX1 c) HEX2, and d) HEX3 (see text for details) . . . . .	23
5.1	Crystal structures of (a) the half-Heusler compound TiNiSn, (b) the filled wurtzite ScCuSn with the LiGaGe structure and (c) LaCuSn, in the ZrBeSi structure type. The structures are depicted in the manner that highlights, respectively, the zinblende NiSn, the wurtzite CuSn and the 'decorated graphite' CuSn networks. The orange spheres are, respectively, Ti, Sc, and La. Light and dark blue spheres represent (Ni/Cu) and Sn. . . . .	29
5.2	Total densities of state obtained from LMTO calculations on the experimental structure of LaCuSn, YCuSn and ScCuSn. The DOS in the main panel are offset on the ordinate for clarity. The inset shows the DOS of the three compounds in a region close to $E_F$ . . . . .	30

5.3	COHPs of the Cu–Sn interaction in the three compounds LaCuSn, YCuSn and ScCuSn. . . . .	31
5.4	Band structures of experimental and hypothetical LaCuSn structures. . .	33
5.5	Electron localization functions (ELFs) of the valence electrons of LaCuSn in (a) the experimental crystal structure and in (b) the hypothetical wurtzite structure. The ELF isosurface is displayed for a value of 0.75. . .	34
5.6	Electron density isosurfaces plotted for values of $0.025e\text{\AA}^{-3}$ for LaCuSn in (a) the experimental crystal structure and in (b) the hypothetical wurtzite structure. The electron density is colored according to the degree of localization. . . . .	34
6.1	Projection of the GdAuMg structure onto the $xy$ plane. All atoms lie on mirror planes at $z = 0$ (thin lines) and $z = 1/2$ (thick lines). Gadolinium, gold, and magnesium atoms are drawn as grey, black, and open circles, respectively. The trigonal prisms around the gold atoms are emphasized. The coordination polyhedra are drawn in the upper part and the site symmetries are indicated. . . . .	38
6.2	LDA + $U$ total DOS and orbital projected Gd $f$ DOS for GdAu $E$ ( $E = \text{Mg, Cd and In}$ ) compounds. In these and in other plots, the top of the valence band is taken as zero on the energy axis. . . . .	41
6.3	LDA orbital-projected density of states for GdAuMg (a) (b), GdAuCd (c) (d) and GdAuIn (e) (f). The orbitals that contribute to the DOS are labelled. . . . .	42
6.4	Crystal Orbital Hamiltonian Populations (COHPs) for the Au– $E$ interactions in GdAu $E$ ( $E = \text{Mg, Cd and In}$ ). Integrated COHP (ICOHPs) are depicted using broken lines. Note: There are two inequivalent Au atoms in the cell. ICOHPs are obtained by integration of the COHPs from over all valence electrons, i.e., up to the top of the valence band. The values of ICOHPs are (a) Au1–Mg 1.118; Au2–Mg 1.229 (b) Au1–Cd 1.2467; Au2–Cd 1.500 (c) Au1–In 1.08; Au2–In 1.3248 in unit eV per interactions. . . . .	44
7.1	Dependence of structure and unit cell volume on the $RE$ - atom for $RENiSb$ compounds. . . . .	47
7.2	Reported structures of GdNiSb: AlB <sub>2</sub> (top left), ZrBeSi (top right) and MgAgAs structure (bottom). . . . .	48
7.3	Density of states (DOS) of both GdNiSb compounds. . . . .	49
7.4	<sup>155</sup> Gd - Mössbauer spectra of biphasic GdNiSb (cubic phase = dotted line, hexagonal phase = dot-dashed line). . . . .	50
7.5	Trend of the magnetic hyperfine field $B_{hf}$ in cubic GdNiSb. . . . .	51
8.1	Dependence of structure and unit cell volume on the $RE$ - atom for $REPdSb$ compounds [37] . . . . .	53
8.2	Powder x-ray diffraction pattern of GdPdSb. The difference plot is shown at the bottom of the figure. $R_{Bragg}$ (GdPdSb) = 5.01 . . . . .	54

8.3	Crystal Structure of GdPdSb (LiGaGe - structure, $P6_3mc$ ) . . . . .	55
8.4	LAPW band structure of antiferromagnetic GdPdSb from the (a) GGA and the (b) LDA + $U$ calculations. For comparison, the DOS calculated using the LDA + $U$ with a photoemission spectrum from GdPdSb excited by Mg $K_\alpha$ radiation is given in (c). . . . .	57
8.5	Projected density of states for ferromagnetic GdPdSb within the GGA a) and the LDA + $U$ b). The insets enlarge the DOS around the Fermi energy. Spin up states are shown in the upper portion and spin down states in the lower portion of each plot. The top of the valence band is taken as zero on the energy axis. . . . .	58
8.6	a) Magnetization curve in high magnetic fields at 4 K; b) inverse magnetic susceptibility of GdPdSb ( $T_N = 13.1$ K); c) susceptibility below 17 K as a function of temperature in an applied field of $80 \times 10^3$ A/m . . . . .	59
8.7	Sections of hysteresis loops of GdPdSb for different temperatures. . . . .	60
8.8	Conductivity measurements of GdPdSb at low temperatures. . . . .	61
8.9	$^{155}\text{Gd}$ Mössbauer spectra of GdPdSb at different temperatures . . . . .	62
8.10	Temperature dependence of the magnetic hyperfinefield (top) and angle between hyperfinefield and field gradient (bottom) . . . . .	63
9.1	Powder x-ray diffraction patterns of GdAuSn (top) and MnAuSn (bottom) together with Rietveld refinement curves (red circles). The difference plot is shown at the bottom of the figures. $R_{Bragg}$ (GdAuSn) = 2.02, $R_{Bragg}$ (MnAuSn) = 4.67. . . . .	66
9.2	Structure of hexagonal GdAuSn and cubic MnAuSn. The layered ABC and ABAB structure is emphasized . . . . .	68
9.3	LDA band structure of MnAuSn; the top of the valence band is taken as zero on the energy axis. . . . .	68
9.4	Density of states (DOS) for GdAuSn (top) and ErAuSn (bottom). . . . .	69
9.5	$\chi_M$ vs. $T$ of GdAuSn ( $T_N = 26$ K), ErAuSn ( $T_N = 4$ K) and TmAuSn. . . . .	70
9.6	Temperature dependence of the magnetisation of MnAuSn in an applied field of 8000 A/m; $T_C = 570\text{K}$ . Insert shows the hysteresis loop at 5K. . . . .	71
9.7	$^{197}\text{Au}$ and $^{155}\text{Gd}$ Mössbauer spectra of GdAuSn at $T = 12$ K . . . . .	72
9.8	$^{119}\text{Sn}$ Mössbauer spectra of GdAuSn across the antiferromagnetic transition. . . . .	74
9.9	Zero magnetic field conductivity measurements of MnAuSn, TmAuSn and GdAuSn. . . . .	75
9.10	Electrical resistance of REAuSn compounds without and with an externally applied field of $1.6 \times 10^6$ A/m . Below each plot the respective magnetoresistance (MR). . . . .	76
9.11	Magnetoresistance of TmAuSn at and below the metal – insulator transition temperature and of ErAuSn. Straight lines are fits using the expression 9.4. . . . .	77
9.12	Photoemission spectra (top, excitation energy = 21.2 eV) and calculated DOS (bottom) for hexagonal and cubic ErAuSn . . . . .	78

9.13	$^{119}\text{Sn}$ Mössbauer spectra of GdAuSn, MnAuSn and their 0.95/0.05 mixture at $T = 80$ K. . . . .	79
9.14	Magnetoresistance of the granular systems $(\text{GdAuSn})_{0.1}(\text{MnAuSn})_{0.9}$ at $T = 3$ K (open circles) and $T = 30$ K (filled circles). . . . .	80
10.1	Structure of $RENiBi$ (Half-heulser structure, $F\bar{4}3m$ ). A filled tetrahedral side is emphasized with lines. . . . .	84
10.2	Temperature dependence of the magnetization of $RENiBi$ compounds in a magnetic field of $4 \times 10^6$ Am $^{-1}$ . . . . .	87
10.3	Magnetic ordering temperatures $T_N$ (top) and paramagnetic Curie $\theta_P$ (bottom) of $RENiBi$ compounds as a function of the rare earth atom: solid curve, prediction of the de Gennes scaling whereby $T_N$ should be maximum of the Gd-containing compounds; $\Delta$ experimental data . . . . .	89
10.4	Normalized Resistance in the temperature range from 3K to 300K of metallic (top) and semiconducting (bottom) $RENiBi$ compounds. . . . .	90
10.5	Density of states (DOS) of some $RENiBi$ and hypothetical $\text{ErNi}_2\text{Bi}$ compounds. . . . .	92
10.6	Electrical resistance of $RENiBi$ compounds without and with an externally applied field of $1.6 \times 10^6$ A/m. Below each plot the respective magnetoresistance (MR). . . . .	93
10.7	Electrical resistance in the presence of externally applied magnetic fields (H) and magnetoresistance (MR) as a function of temperature (T) for DyNiBi. . . . .	94
10.8	Magnetoresistance of $RENiBi$ samples at the respective metal – insulator transition temperatures. Straight lines are fits using Expression 9.4. . . . .	94
10.9	Scanning microscope image of a polished DyNiBi surface. Arrows mark Bi dots in the DyNiBi matrix (A) and on the surface (B) due to soft polishing	95
10.10	Field dependence of the resistance at 10K. Two samples with slightly different bismuth impurities were measured (red dots = higher impurity content). . . . .	95
10.11	Electrical resistance in the presence of an externally applied magnetic field (H) and magnetoresistance (MR) as a function of temperature (T) for LuNiBi. . . . .	96
10.12	Field dependence of the resistance at 300 K. . . . .	97
11.1	Calculated band gaps form some $REME$ compounds with MgAgAs structure. . . . .	99

# List of Tables

1.1	Overview of the <i>REME</i> compounds structure variety according to the number of valence electrons (VE). . . . .	7
1.2	The classification of half-metals proposed by Coey <i>et al.</i> [62] . . . . .	17
3.1	Unit cell parameters for the antiferromagnetic structure of <i>REME</i> compounds with LiGaGe structure. . . . .	23
5.1	Crystal structures of the compounds whose electronic structures are described here. <i>RE</i> (Sc, Y, La) at (0,0,0), Cu at $\frac{2}{3}, \frac{1}{3}, z(Cu)$ and Sn at $\frac{1}{3}, \frac{2}{3}, z(Sn)$ . The first three experimental crystal structures are taken from [106].	29
6.1	Interatomic distances (pm) in the structures of GdAu <i>E</i> ( <i>E</i> = In, Mg and Cd) [118, 119, 120]. All distances within the first coordination sphere are listed . . . . .	39
6.2	Experimental crystal structures of GdAu <i>E</i> ( <i>E</i> = Mg, Cd and In), space group P62m (No. 189); Gd in (x, 0, 0); Au1 in $(\frac{1}{3}, \frac{2}{3}, \frac{1}{2})$ ; Au2 in (0, 0, 0); E in $(x, 0, \frac{1}{2})$ . . . . .	39
6.3	Total energy difference $\Delta E$ (in eV) between the ferromagnetic (FM) and antiferromagnetic (AFM) structures of GdAu <i>E</i> ( <i>E</i> = Mg, Cd and In) and corresponding Neel temperature in Kelvin. . . . .	40
9.1	Lattice parameter of <i>REAuSn</i> and <i>MnAuSn</i> compounds . . . . .	66
9.2	Crystal data and structure refinement for GdAuSn. . . . .	67
9.3	Calculated energy and magnetic parameters for the three simple antiferromagnetic ordering structures of GdAuSn . . . . .	69
9.4	The set of hyperfine parameters and effective moments obtained from band structure calculations of MnAuSn. . . . .	71
10.1	Calculated ( $I_C$ ) and observed ( $I_0$ ) x – ray diffraction intensities of ErNiBi with MgAgAs (Half-Heusler-) structure and hypothetical ErNi <sub>2</sub> Bi with MnCu <sub>2</sub> Al- (full-Heusler-) structure. The pattern was recorded with CuK $\alpha$ radiation. . . . .	85
10.2	Lattice parameter, cell volume and <i>RE</i> - <i>RE</i> distance of <i>RENiBi</i> with cubic MgAgAs-Type structure . . . . .	85
10.3	Magnetic properties of <i>RENiBi</i> ( <i>RE</i> = Pr, Sm, Gd-Tm, Lu) compounds. The theoretic moments are obtained from $\mu_{eff}(theo) = g_j[J(J + 1)]^{1/2}$ . . . . .	88

10.4 Electrical behavior of $RENiBi$ ( $RE = Pr, Sm, Gd, Dy, Er, Tm, Lu$ ) compounds. (SC = semi conductor; SC-metal = semi conductor to metal transition). . . . .	90
---	----

# Bibliography

- [1] P. Villars and L. D. Calvert. *Pearsons's Handbook of Crystallographic Data for Intermetallic Compounds*. American Society of Metals: Materials Park, OH 44073; desk edition, 1997.
- [2] R. D. Hoffmann and R. Pöttgen. *Z. Kristallogr.*, 216:127, 2001.
- [3] R. Pöttgen and D. Johrendt. *Chem. Mater.*, 12:875, 2000.
- [4] S. K. Dhar, N. Nambudripad, and R. Vijayaraghavan. *J. Phys. F:Met Phys*, 18:L41, 1988.
- [5] I. Karla, J. Pierre, and B. Ouladdiaf. *Physica B*, 253:215, 1998.
- [6] H. Fujii, Y. Uwatoko, M. Akayama, K. Satoh, Y. Maeno, T. Fujita, J. Sakurai, H. Kanimura, and T. Okamoto. *Jpn. J. Appl. Phys.(Suppl.)*, 26:549, 1987.
- [7] A. Slebarski, W. Glogowski, A. Jezierski, A. Czopnik, and A. Zygmunt. *Phys. Rev. B*, 70:184429, 2004.
- [8] C. Felser, S. Cramm, D. Johrendt, J. Mewis, O. Jepsen, G. Hohlneicher, W. Eberhardt, and O. K. Andersen. *Europhys. Lett.*, 40:85, 1997.
- [9] V. Ksenofontov, H. C. Kandpal, J. Ensling, M. Waldeck, D. Johrendt, A. Mewis, P. Gtlich, and C. Felser. *Europhys. Lett.*, 74:672, 2006.
- [10] D. T. Adroja, S. K. Malik, S. N. Padalia, R. Walia, and R. Vijayaraghavan. *Phys. Rev. B*, 42:2700, 1997.
- [11] T. Takabatake, Y. Nakazawa, and M. Ishikawa. *Jpn. J. APpl. Phys. (Suppl.)*, 26:547, 1987.
- [12] C. L. Chien. *J. Appl. Phys.*, 69:5267, 1991.
- [13] F. Canepa and S. Cirafici. *J. Alloys Compds.*, 232:71, 1996.
- [14] J. Pierre, I. Karla, and K. Kaczmariska. *Physica B*, 259-261:845, 1999.
- [15] S. K. Malik, H. Takeya, and K. A. Gschneider Jr. *Phys. Rev. B*, 48:9858, 1993.
- [16] C. Felser, G. H. Fecher, and B. Balke. *Angew. Chem. Int. Ed.*, 46:668, 2007.

- 
- [17] M. D. Bojin and R. Hoffmann. *Helvetica Chimica Acta*, 86:1653, 2003.
- [18] M. D. Bojin and R. Hoffmann. *Helvetica Chimica Acta*, 86:1683, 2003.
- [19] D. Jung, H.-J. Koo, and M.-H. Whangbo. *J. Mol. Struct. Theochem.*, 527:113, 2000.
- [20] H. C. Kandpal, R. Seshadri, and C. Felser. *J. Phys. D: Appl. Phys.*, 39:776, 2006.
- [21] R. A. de Groot, F. M. Mueller, P. G. van Engen, and K. H. J. Buschow. *Phys. Rev. Lett.*, 50:2024, 1983.
- [22] J.-S. Kang, J. H. Hong, S. W. Jung, Y. P. Lee, J.-G. Park, S.-J. Olson, C. G. and Youn, and B. I. Min. *Solid State Commun.*, 88:653, 1993.
- [23] F. Casper, V. Ksenofontov, H. C. Kandpal, S. Reiman, T. Shishido, M. Takahashi, M. Takeda, and C. Felser. *Z. Anorg. Allg. Chem.*, 632:71, 2006.
- [24] S. Baran, J. Leciejewicz, N. Stüsser, A. Szytula, A. Zygmunt, and V. Ivanov. *J. Phys. Condens. Matter*, 8:8397, 1996.
- [25] S. Baran, J. Leciejewicz, N. Stüsser, A. Szytula, and Z. Tomkowicz. *Solid State Commun.*, 101:631, 1997.
- [26] S. Baran, J. Leciejewicz, M. Slaski, P. Hofmann, and A. Szytula. *J. Alloys Compds.*, 275-277:541, 1998.
- [27] R. Hatzl, M. Reissner, M. Forsthuber, E. Gratz, W. Steiner, G. Wiesinger, and K. Yvon. in "Conf. Proc. 50 ICAME-95", page 347. SIF, Bologna, 1996.
- [28] A. Szytula. *Handbook of magnetic materials 6*, page 85. K. H. J. Buschow (Eds), Amsterdam: North Holland, 1991.
- [29] H. Lueken. *Magnetochemie*. (Stuttgart, Leipzig: B. G. Teubner), 1999.
- [30] F. Casper, H. C. Kandpal, G. H. Fecher, and C. Felser. *J. Phys. D: Appl. Phys.*, 40:3024, 2007.
- [31] M. A. Rudermann and C. Kittel. *Phys. Rev.*, 96:99, 1954.
- [32] T. Kasuya. *Prog. Theor. Phys.*, 16:45, 1956.
- [33] K. Yoshida. *Phys. Rev.*, 106:106, 1957.
- [34] P. W. Anderson. in "Magnetism", Volume 1, page 25. JG. T. Rado and H. Suhl., Eds., Academic Press, New York, London, 1963.
- [35] G. J. van den Berg and J. de Nobel. *J. Phys. Radium*, 23:665, 1962.
- [36] J. Kondo. *Prog. Theor. Phys.*, 32:37, 1964.

- 
- [37] S. K. Malik and D. T. Adroja. *Phys. Rev. B*, 43:6295, 1991.
- [38] W. Thomson. *Prog. R. Soc. London*, A8:546, 1857.
- [39] G. Binasch, P. Grünberg, F. Saurenbach, and W. Zinn. *Phys. Rev. B*, 39:4828, 1989.
- [40] M. N. Baibach, J. M. Broto, A. Fert, F. N. Vandau, F. Petroff, P. Etienne, G. Creuzet, A. Friedrich, and J. Chazelas. *Phys. Rev. Lett.*, 61:2472, 1988.
- [41] P. Ball. *Nature*, 404:918, 2000.
- [42] G. H. Jonker and J. H. Van Santen. *Physica*, 16:337, 1950.
- [43] J. H. Van Santen and G. H. Jonker. *Physica*, 16:559, 1950.
- [44] R. v. Helmolt, J. Wecker, B. Holzapfel, L. Schultz, and K. Samwer. *Phys. Rev. Lett.*, 71:2331, 1993.
- [45] S. Jin, T. H. Tiefel, M. McCormack, R. A. Fastnacht, R. Ramesh, and L. H. Chen. *Science*, 264:413, 1994.
- [46] M. R. Oliver, J. O. Dimmock, A. L. McWhorter, and T. B. Reed. *Phys. Rev. B*, 5:1078, 1972.
- [47] C. Felser, K. Ahn, R. K. Kremer, R. Seshadri, and A. Simon. *J. Solid State Chem.*, 147:19, 1999.
- [48] S. v. Molnar, A. Briggs, J. Flouquet, and G. Remenyi. *Phys. Rev. Lett.*, 51:706, 1983.
- [49] M. Julliere. *Phys. Rev. Lett.*, 54A:225, 1975.
- [50] S. S. P. Parkin, C. Kaiser, A. Panchula, P. M. Rice, B. Hughes, M. Samant, and S.-H. Yang. *Nature Materials*, 3:862, 2004.
- [51] S. Yuasa, A. Fukushima, T. Nagahama, K. Ando, and Y. Suzuki. *Jpn. J. Appl. Phys.*, 43:L588, 2004.
- [52] S. Yuasa, T. Nagahama, A. Fukushima, Y. Suzuki, and K. Ando. *Nature Materials*, 3:868, 2004.
- [53] A. E. Berkowitz, J. R. Mitchell, M. J. Carey, A. P. Young, S. Zhang, F. E. Spada, F. T. Parker, A. Hutten, and G. Thomas. *Phys. Rev. Letters*, 68:3745, 1992.
- [54] S. A. Solin, T. Thio, D. R. Hines, and J. J. Heremans. *Science*, 289:1530, 2000.
- [55] S. A. Solin, D. R. Hines, A. C. H. Rowe, J. S. Tsai, Yu. A. Pashkin, S. J. Chung, N. Goel, and M. B. Santos. *Appl. Phys. Lett.*, 80:4012, 2002.
- [56] M. Weiss, H. and Wilhelm. *Z. f. Phys.*, 176:399, 1963.

- [57] S. A. Wolf, D. D. Awschalom, R. A. Buhrman, J. M. Daughton, M. L. von Molnar, A. Y. Chtchelkanova, and D. M. Treger. *Science*, 294:1488, 2001.
- [58] I. Zutic, J. Fabian, and S. Das Sarma. *Rev. Mod. Phys.*, 76:323, 2004.
- [59] W. S. Pickett and J. S. Moodera. *Phys. Today*, 54:34, 2001.
- [60] P. Grünberg. *Phys. Today*, 54:31, 2001.
- [61] J. Kübler, A. R. Williams, and C. B. Sommers. *Phys. Rev. B*, 28:1745, 1983.
- [62] J. M. D. Coey, M. Venkatesan, and M. A. Bari. *Lecture Notes in Physics*, volume 595. Heidelberg: Springer, 2002.
- [63] B. Nadgorny, I. I. Mazin, M. Osofsky, R. J. Soulen Jr., P. Broussard, R. M. Stroud, D. J. Singh, V. G. Harris, A. Arsenov, and Y. Mukovskii. *Phys. Rev. B*, 63:184433, 2001.
- [64] P. Blaha, K. Schwarz, G. K. H. Madsen, D. Kvasnicka, and J. Luitz. *WIEN2K, An augmented plane wave + local orbitals program of calculating crystal properties*. Karlheinz Schwarz, Techn. Universität Wien, Austria, 2001.
- [65] J. P. Perdew, K. Burke, and M. Enzerhof. *Phys. Rev. Lett.*, 77:3865, 1996.
- [66] V. I. Anisimov, F. Aryasetiawan, and A. I. Lichtenstein. *J. Phys. Condens. Matter*, 9:767, 1997.
- [67] O. Jepsen and O. K. Andersen. *TB-LMTO-ASA-47*. MPI für Festkörperforschung, Stuttgart, Germany, 2000.
- [68] O. Jepsen and O. K. Anderson. *Z. Phys. B*, 97:35, 1995.
- [69] R. Dronskowski and P. E. Bloechl. *J. Phys. Chem.*, 97:8617, 1993.
- [70] A. D. Becke and K. E. Edgecombe. *J. Chem. Phys.*, 92:5397, 1990.
- [71] B. Silvi and A. Savin. *Nature*, 371:683, 1994.
- [72] S. Baran, M. Hofmann, N. Stüsser, A. Szytula, P. Smeibidl, and S. Kausche. *J. Magn. Magn. Mat.*, 231:94, 2000.
- [73] D. Bialic, R. Kruk, R. Kmiec, and K. Tomala. *J. Alloys Compds.*, 257:49, 1997.
- [74] J. Rodríguez-Carval. *Physica B*, 192:55, 1993.
- [75] W. Haberditzl. *Magnetochemie*. (Berlin:Akademie), 1968.
- [76] CP-NIM. [http://www.bessy.de/upload/bitpdfs/d\\_16\\_1b.pdf](http://www.bessy.de/upload/bitpdfs/d_16_1b.pdf), 2004.
- [77] K. Lagerec and D. G. Rancourt. *Phys. Rev. B*, 129:266, 1997.

- [78] Z. Klencsar. *Nucl. Instrum. Methods B*, 129:527, 1997.
- [79] I. I. Mazin. *Appl. Phys. Lett.*, 77:3000, 2000.
- [80] K. Ramesha, R. Seshadri, C. Ederer, T. He, and M. A. Subramanian. *Phys. Rev. B*, 70:214409, 2004.
- [81] J. E. Pask, L. H. Yang, C. Y. Fong, W. E. Pickett, and S. Dag. *Phys. Rev. B*, 67:224420, 2003.
- [82] J. I. Horikawa, T. Hamajima, F. Ogata, T. Kambara, and K. I. Gondaira. *J. Phys. C: Solid State Phys.*, 15:2613, 1982.
- [83] M. S. Park, S. K. Kwon, S. J. Youn, and B.I. Min. *Phys. Rev. B*, 59:10018, 1999.
- [84] I. Galanakis, P. H. Dederichs, and Papanikolaou. *Phys. Rev. B*, 66:134428, 2002.
- [85] J. Köhler, S. Deng, C. Lee, and M. H. Whangbo. *Inorg. Chem.*, 46:1957, 2007.
- [86] C. Palmstrom. *MRS Bull.*, 28:725, 2003.
- [87] T. Block, C. Felser, G. Jakob, J. Ensling, B. Müling, P. Gütlich, and R. J. Cava. *J. Solid State Chem.*, 176:646, 2003.
- [88] P. I. Sorantin and K. Schwarz. *Inorg. Chem.*, 31:567, 1992.
- [89] I. I. Mazin, D. J. Singh, and C. Ambrosch-Draxl. *Phys. Rev. B*, 59:411, 1999.
- [90] W. S. Pickett and D. J. Singh. *Phys. Rev. B*, 53:1146, 1996.
- [91] H. S. Jarrett, W. H. Cloud, R. J. Bouchard, S. R. Butler, C. G. Frederick, and J. L. Gillson. *Phys. Rev. Lett.*, 21:617, 1968.
- [92] I. Galanakis and P. Mavropoulos. *Phys. Rev. B*, 67:104417, 2003.
- [93] R. A. de Groot. *Physica B*, 172:45, 1991.
- [94] N. Lossau, H. Kierspel, J. Langen, W. Schlabitz, D. Wohlleben, A. Mewis, and C. Sauer. *Z. Phys. B*, 74:227, 1989.
- [95] R. Pöttgen, D. Johrendt, and D. Kussmann. *Handbook of the Physics and Chemistry of Rare Earths vol 32*, page 453. Amsterdam: North-Holland, 2001.
- [96] R. Pöttgen, H. Borrmann, and R. K. Kremer. *J. Magn. Magn. Mater.*, 152:192, 1996.
- [97] J. F. Riecken, G. Heymann, T. Soltner, R. D. Hoffmann, H. Huppertz, D. Johrendt, and R. Pöttgen. *Z. Naturf. B*, 60:825, 2005.
- [98] W. H. Lee and R. N. Shelton. *Phys. Rev. B*, 35:5369, 1989.

- [99] K. Umeo, K. Masumori, T. Sasakawa, F. Iga, T. Takabate, Y. Ohishi, and T. Adachi. *Phys. Rev. B*, 71:064110, 2005.
- [100] S. K. Malik and D. T. Adroja. *J. Magn. Magn. Mater.*, 102:42, 1991.
- [101] J. Pierre and I. Karla. *J. Magn. Magn. Mater.*, 217:74, 2000.
- [102] R. Pöttgen, H. Borrmann, C. Felser, O. Jepsen, R. Henn, R. Kremer, and A. Simon. *J. Alloys Compounds*, 23:170, 1996.
- [103] G. Nuspl, K. Polborn, J. Evers, G. A. Landrum, and R. Hoffmann. *Inorg. Chem.*, 35:6922, 1996.
- [104] G. A. Landrum, R. Hoffmann, J. Evers, and H. Boysen. *Inorg. Chem.*, 37:5754, 1998.
- [105] E. Gaudin, B. Chevalier, U. Heying, C. Rodewald, and R. Pöttgen. *Chem. Mater.*, 17:2693, 2005.
- [106] C. P. Sebastian, C. Fehse, H. Eckert, R. D. Hoffmann, and R. Pöttgen. *Solid State Sci.*, 8:1386, 2006.
- [107] C. P. Sebastian, S. Rayaprol, R. D. Hoffmann, U. C. Rodewald, T. Pape, and R. Pöttgen. *Z.f.Naturf. b*, 62:647, 2007.
- [108] A. Slebarski. *J. Alloys Compounds*, 423:15, 2006.
- [109] V. K. Pecharsky and K.A. Gschneider Jr. *Appl. Phys. Lett.*, 70:3299, 1997.
- [110] V. K. Pecharsky and K.A. Gschneider Jr. *Adv. Cryog. Eng.*, 43:1729, 1998.
- [111] K. A. Gschneider Jr. and V. K. Pecharsky. *Annu. Rev. Mater. Sci.*, 30:387, 2000.
- [112] K. A. Gschneider Jr., V. K. Pecharsky, and A. O. Tsokol. *Rep. Prog. Phys.*, 68:1479, 2005.
- [113] V. K. Pecharsky and K.A. Gschneider Jr. *Phys. Rev. Lett.*, 78:4494, 1997.
- [114] E. Brück, O. Tegus, L. Zhang, X. W. Li, F. R. de Boer, and K. H. J. Buschow. *J. Alloys Compds.*, 383:32, 2004.
- [115] C. P. Sebastian and R. Pöttgen. *Z.f.Naturf. B: Chemical Sciences*, 61:1045, 2006.
- [116] S. Baran, M. Hofmann, J. Leciejewicz, M. Slaski, A. Szytula, and A. Zygmunt. *J. Phys. Condens. Mat.*, 9:9053, 1997.
- [117] H. Oesterreicher. *J. Less-Common Met.*, 55:131, 1977.
- [118] K. Latka, R. Kmiec, A. W. Pacyna, Th. Fickenscher, R. D. Hoffmann, and R. Pöttgen. *Solid State Sci.*, 6:301, 2004.

- [119] K. Latka, R. Kmiec, A. W. Pacyna, Th. Fickenscher, R. D. Hoffmann, and R. Pöttgen. *J. Magn. Magn. Mater.*, 280:90, 2004.
- [120] R. Pöttgen, G. Katzyba, K. Görlich, E. A. an Latka, and R. Dronskowski. *J. Solid State Chem.*, 141:352, 1998.
- [121] J. Gegner, T. C. Koethe, H. Wu, H. Hartmann, T. Lorenz, T. Fickenscher, R. Pöttgen, and L. H. Tjeng. *Phys. Rev. B*, 74:073102, 2006.
- [122] H. C. Kandpal, Frederick Casper, G. H. Fecher, C. Felser, J. Kübler, and Rainer Pöttgen. *submitted*, 2008.
- [123] R. Seshadri and N. A. Hill. *Chem. Mater.*, 13:2892, 2001.
- [124] J. M. Raulot, G. Baldinozzi, R. Seshadri, and P. Cortona. *Solid State Sci.*, 4:467, 2002.
- [125] J. Emsley. *The Elements*. Clarendon Press Oxford, 1989.
- [126] A. E. Dwight. in "Proceedings of Rare Earth Research Conference 11th", page 642. J.M. Haschke and H.A. Eick, Eds., NTIS, Springfield, VA, 1974.
- [127] V. K. Pecharskii, Y.V. Pankevich, and O. I. Bodak. *Sov. Phys. Crystallogr.*, 28:97, 1983.
- [128] R. V. Skolozdra, A. Guizik, A. M. Goryn, and J. Pierre. *Acta Phys. Pol. A*, 92:343, 1997.
- [129] H. Hartjes and W. Jeitschko. *J. Alloys Compds.*, 226:81, 1995.
- [130] G. LeBras, P. Bonville, P. Imbert, G. Polatsek, M. J. Besnus, P. Haen, and V. Moshchal'kov. *Physica B*, 199&200:542, 1994.
- [131] R Marazza, D. Rossi, and R. Ferro. *J. Less-Common Met.*, 78:1, 1980.
- [132] A. Zygmunt and Szytula. A. *J. Alloys Compds.*, 219:185, 1995.
- [133] A. Imre and A. Mewis. *Z. Naturforsch.*, 61b:17, 2006.
- [134] S. Baran, J. Ivanov, J. Leciejewicz, N. Stüsser, A. Szytula, A. Zygmunt, and Y. Ding. *J. Alloys Compds.*, 257:5, 1997.
- [135] S. Baran, J. Leciejewicz, N. Stüsser, A. Szytula, A. Zygmunt, and Y. Ding. *J. Mag. Mag. Mater.*, 170:143, 1997.
- [136] C. Felser, R. Seshadri, A. Leist, and W. Tremel. *J. Mater. Chem.*, 8:787, 1998.
- [137] M. S. Augsburger, M. C. Viola, J. C. Pedregosa, A. Muñoz, J. A. Alonso, and J. Carbonio. *J. Mater. Chem.*, 15:993, 2005.
- [138] P. G. de Gennes. *J. Phys. Radium*, 23:510, 1962.

- [139] V. Ksenofontov, K. Kroth, S. Reiman, F. Casper, V. Jung, M. Takahashi, M. Takeda, and C. Felser. *Hyp. Int.*, 168:1201, 2006.
- [140] S. Cirafici, A. Palenzona, and F. Canepa. *J. Less-Common Met.*, 107:179, 1985.
- [141] W. Albers. *Preparative Methods of Solid State Chemistry*. Hagen Müller (eds), Academic Press, New York, 1972.
- [142] A. Neumann, L. Offernes, A. Kjekshus, and B. Klewe. *J. Alloys Compds.*, 274:136, 1998.
- [143] K. Latka, E. A. Görlich, R. Kmiec, R. Kruk, A. W. J. Pacyna, and W. Chajec. *Mol. Phys. Rep.*, 22:87, 1998.
- [144] A. E. Dwight. in *"Proceedings of Rare Earth Research Conference 12th"*, page 480. J.M. Haschke and H.A. Eick, Eds., NTIS, Springfield, VA, 1976.
- [145] G. M. Sheldrick. *SHELXL-97, Program for the crystal structure refinement*. University of Göttingen, Germany, 1997.
- [146] S. Baran, M. Hofmann, N. Stüsser, A. Szytula, P. Smeibidl, and S. Kausche. *J. Magn. Magn. Mat.*, 231:94, 2001.
- [147] K. Latka, J. Gurgul, R. Kmiec, A. W. Pacyna, and W. Chajec. *J. Alloys Compds.*, 400:16, 2005.
- [148] N. N. Greenwood and T. C. Gibb. *Mössbauer spectroscopy*. Chapman and Hall, London, 1971.
- [149] J. G. Stevens and V. E. Stevens. *Mössbauer effect data index*, page 136. Plenum, New York, 1975.
- [150] R. E. Watson and A. J. Freeman. *Phys. Rev.*, 123:2027, 1961.
- [151] J. M. Ziman. *Electrons and Phonons*, page 492. Oxford University Press, London, 1963.
- [152] R. Mallik and E. V. Sampathkumaran. *Phys. Rev. B*, 58:9178, 1998.
- [153] M. K. Gubkin, T. M. Perekalina, A. V. Bykov, and V. A. Chubarenko. *Phys. Solid State*, 35:728, 1993.
- [154] Y Tokura (eds). *Colossal Magnetoresistance Oxides*. Gordon and Breach Science, New York, 2000.
- [155] H. L. Ju, J. Gopalakrishnan, J. L. Peng, Q. Li, G. C. Xiong, T. Venkatesan, and R. L. Green. *Phys. Rev. B*, 51:6143, 1995.
- [156] R. D. Sanchez, J. Rivas, C. Vazquez-Vazquez, A. Lopez-Quintela, M. T. Causa, M. Tovar, and S. Oseroff. *Appl. Phys. Lett.*, 68:134, 1996.

- 
- [157] R. Mahesh, R. Mahendiran, A. K. Raychaudhuri, and C. N. R. Rao. *Appl. Phys. Lett.*, 68:2291, 1996.
- [158] S. Lee, H. Y. Hwang, B. I. Shraiman, W. D. Ratcliff II, and S.-W. Cheong. *Phys. Rev. B*, 82:4508, 1998.
- [159] A. E. Dwight. *J. Less Common Met.*, 34:279, 1974.
- [160] M. G. Haase, T. Schmidt, C. G. Richter, H. Block, and W. Jeitschko. *J. Solid State Chem.*, 168:18, 2002.
- [161] I. Karla, J. Pierre, and R. V. Skolozdra. *J. Alloys Compds.*, 265:42, 1998.
- [162] P. Larson, S. D. Mahanti, S. Sportouch, and M. G. Kanatzidis. *Phys. Rev. B*, 59:15660, 1999.
- [163] V. N. Anatonov, B. N. Harmon, and A. N. Yaresko. *Phys. Rev. B*, 63:205112, 2001.
- [164] Y. Shapira and R.L. Kautz. *Phys. Rev. B*, 10:4781, 1974.
- [165] J. Moussa, L. R. Ram-Mohan, J. Sullivan, T. Zhou, D. R. Hines, and S. A. Solin. *Phys. Rev. B*, 64:184410, 2001.
- [166] I. Eremin, P. Thalmeier, P. Fulde, R. K. Kremer, K. Ahn, and A. Simon. *Phys. Rev. B*, 64:064425, 2001.
- [167] B. Balke, G.H. Fecher, A. Gloskovskii, J. Barth, K. Kroth, C. Felser, R. Robert, and A. Weidenkaff. *submitted*, 2007.
- [168] T. Sekimoto, K. Kurosaki, H. Muta, and S. Yamanaka. *Appl. Phys. Lett.*, 89:092108, 2006.